UH-60 AIRLOADS PROGRAM TUTORIAL

The UH-60A Airloads Program Tutorial was developed by NASA's Subsonic Rotary Wing Project under the Aeronautics Research Mission Directorate.

The purpose of the UH-60A tutorial is to augment helicopter graduate education courses based on the extent and richness of the UH-60A flight test database. Beyond this primary purpose, this tutorial can be used to provide an in-depth introduction to helicopter technology for anyone working in the field.

 For further information, contact Robert Kufeld at Robert.Kufeld@nasa.gov.

January 2009

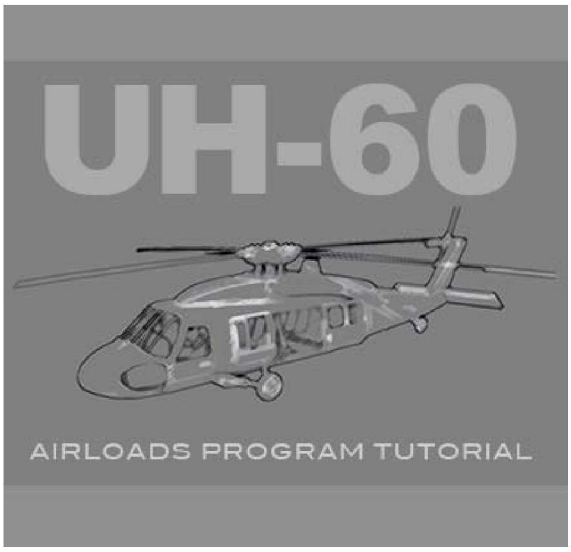

The tutorial is organized in four chapters:

- Chapter 1: Rotor Aeromechanics and Helicopter Design, examines data needs from the designer's perspective.
- Chapter 2: Fundamentals of Rotorcraft Aeromechanics, covers some of the basics of rotorcraft aeromechanics.
- Chapter 3: Airloads Program Experiments, discusses the experiment design.
- Chapter 4: UH-60A Airloads Program Results, is the core of this tutorial.

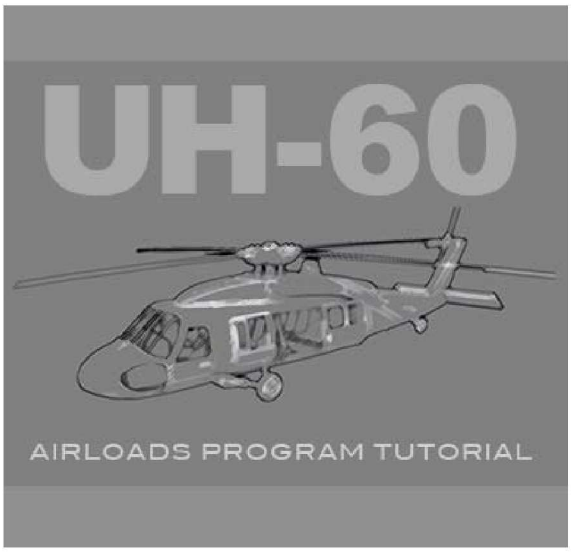

Each chapter begins with an introduction that provides the context for the chapter.The four chapters can be examined in order using the tutorial menu or the buttons on the panels.Or one can skip around as seems useful.

Separate appendices include cited literature, nomenclature, and a site map.These may be accessed directly from buttons on the panels or, in some cases, hyperlinks in the text.

Graphs are used throughout the tutorial and the definition of their variables are in the nomenclature appendix.The nomenclature appendix also includes frequently used terms.

The design of new rotorcraft is based on analysis and guided by experience.But when analytical methods are not trustworthy, the designer must rely on rules of thumb or use data from previous developments.For the scientist or research engineer, the problem is to improve analytical methods so that they are reliable and can be used successfully by the designer, always with the intent of reducing development risk and cost.

The improvement of analytical methods requires advances in many facets of engineering.Above all, these improvements must be tested against experimental measurements.The purpose of the UH-60 Airloads Program was to obtain an extensive set of data on an aircraft in flight with a particular focus on the measurement of blade airloads.The aircraft was tested over a wide range of flight conditions, both in steady flight and in maneuvers.Acoustic measurements were made relative to both ground and airborne microphones.

The UH-60 data have already been used extensively in the development of improved analytical methods.The purpose of this tutorial is to provide an introduction to the breadth of data that are available and at the same time provide a fundamental understanding of rotorcraft aeromechanics.

During the 1980s, NASA and the U.S. Army put together a plan for multiple rotor tests with extensive airloads measurements on the blades.They envisioned three pillars to this program: a model-scale rotor tested in a wind tunnel, a full-scale rotor tested in flight, and that same rotor tested in the 40- by 80-Foot Wind Tunnel.The UH-60A rotor was selected for the first set of tests, since it included technology representative of the period.Compared to prior rotor tests that included airloads measurements, the specification for the UH-60 tests required a ten-fold increase in bandwidth, in part to provide data that could be used with acoustic measurements.

A 0.17-scale model of the UH-60 was tested in the DNW wind tunnel in the Netherlands in 1989 (Yu et al. 1990, Lorber 1991).The UH-60 was tested in flight in 1993-94 (Kufeld et al. 1994).Testing of the UH-60 rotor in the National Full-scale Aerodynamic Complex (NFAC) wind tunnels at Ames Research Center required a new test stand.This test stand, the Large Rotor Test Apparatus (LRTA) was developed and first tested in 2001 (Norman et al. 2002).A test of the pressure-instrumented UH-60 rotor in the 40- by 80-Foot Wind Tunnel is now scheduled for late 2008 or early 2009.

In this chapter, rotorcraft aeromechanics is approached from the designer's viewpoint. The value of the airloads data depends upon whether these data can support a better understanding of how rotorcraft function and whether improved analytical methods can be developed. It is against this objective that the success of the UH-60A Airloads Program is judged.

In the case of the UH-60A, known as the Black Hawk, the Sikorsky Aircraft Project Manager for the program, Ray Leoni, has written a book relating the development of the Black Hawk (Leoni 2007). This book provides a wealth of information on the design of this helicopter, not just in aeromechanics, but across all disciplines. But for this tutorial, we will limit our view to topics in aeromechanics.

Seven general topic areas are discussed in this chapter, each of which are important for design. Many of these topics are related to helicopter performance, but they also include topics such as loads, vibration, and acoustics. The next panel describes the seven topics and the remainder of the chapter discusses the individual topics and shows where Airloads Program data is important for an improved understanding.

The seven aeromechanics design topics discussed in this chapter are:

1. Hover Performance
2. Vertical Rate of Climb (Military)
3. One-Engine-Inoperative OEI Performance
4. Performance, Loads, and Vibration at Maximum Cruise or Level Flight Speed
5. Loads in Critical Maneuvers
6. Vibration at Low Speed (Transition)
7. Noise in low-speed descents

In the aeromechanics discipline, the designer must find solutions for requirements for multiple conditions. Too many design conditions will require too many iterations in the design process, yet if an important condition is overlooked then the design may be inadequate.

Regardless of the tools available, the designer must obtain a solution, whether based on analysis, rules of thumb, or scaled data from previous rotorcraft development programs.

Hover performance must be calculated accurately. The accuracy of the calculation of Figure of Merit shown here (Wachspress et al. 2003) is better than 1%, although such accuracy is rarely achieved.

The UH-60A is a troop carrier and the weight of each troop is 1.5% of the aircraft gross weight. Errors of the order 1-2% may result in an aircraft that cannot carry its full complement of soldiers.

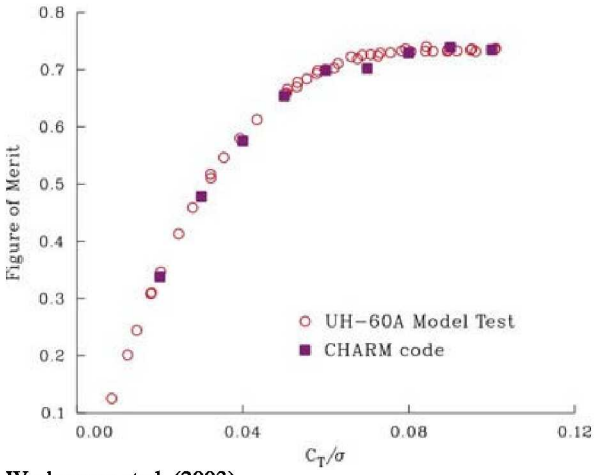

Wachspress et al. (2003)

It is not enough to calculate the main rotor's hover performance accurately. It is also necessary to calculate tail rotor performance (about 10% of main rotor power), download forces (3-5%), gearbox losses (about 1%), and accessory losses (less than 1%).

The tail rotor of the UH-60A is not oriented vertically so that it thrusts only to the side to counteract the main rotor's torque. Rather, it is canted 20 degrees to provide extra lifting force (about 400 lb) and this further complicates the overall calculation.

Vertical Rate of Climb (VROC) is a military requirement for additional power at the hover design point to allow for maneuvering. The required VROC is 500 ft/min for U.S. Army aircraft.

The figure shows that the power for vertical climb is overpredicted with current analyses (Felker et al. 1988). A nondimensional rate-of-climb between 0.2 and 0.3 is equivalent to VROC = 500 ft/min and for this case, the power is overpredicted by about 2.7%. From the designer's perspective the installed power is unnecessarily large and the rotor is not correctly sized.

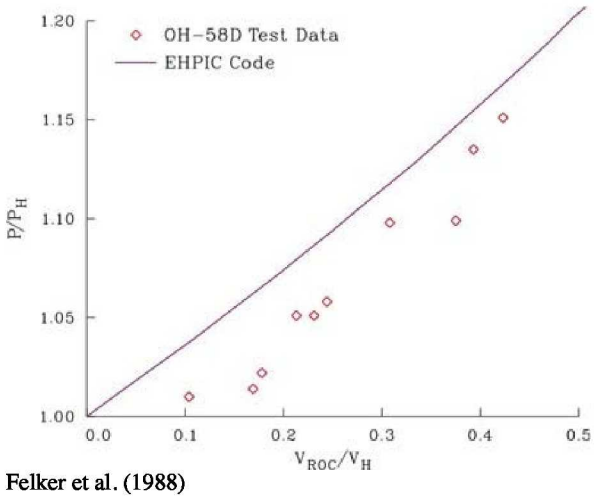

Felker et al. (1988)

For a multi-engine aircraft, whether civilian or military, the One-Engine-Inoperative (OEI) requirements are important for the designer.

First, upon loss of an engine, the aircraft must be able to return to its base, thus, the service ceiling that it can fly at after engine failure must be above any ground obstacles on the return to base. This can be a stringent requirement when operating at high altitudes.

Second, when operating from oil platforms, heliports, or confined areas, the allowable takeoff gross weight will be determined by OEI performance.

Shell Photographic Services

The OEI flight speed is near the minimum power speed of the rotorcraft. The figure here is based on calculations by Yeo et al. (2004) for airspeeds near minimum power for three sets of UH-60 flight test data. The analysis CAMRAD II was used for the predictions. The accuracy of the calculation is assessed by using linear regression to compare the measured and calculated values (Bousman and Norman 2008). The power is overpredicted by 5.4% as shown in the figure. There is considerable scatter in the measurements. It may be that the test measurements are less accurate than the analysis.

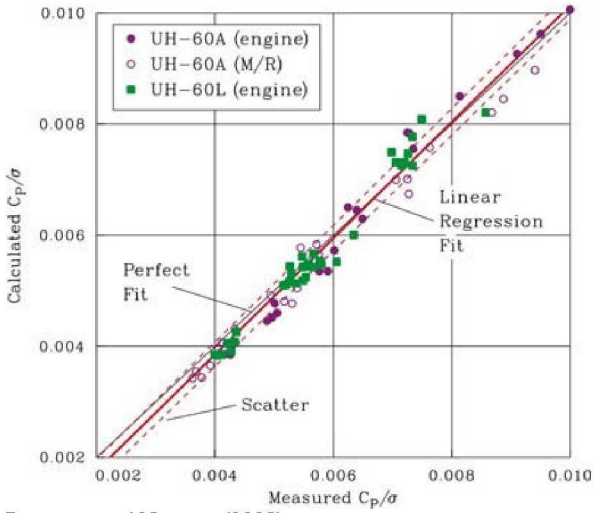

Bousman and Norman (2008)

The figure shows the level flight data obtained during the NASA-U.S. Army UH-60A Airloads Program, where the aircraft weight coefficient, normailzed by solidity, is shown as a function of advance ratio. At lower thrust values, the aircraft is limited in forward speed by transonic drag rise on the rotor blade, and at higher thrust, by dynamic stall. The stall limit is indicated by the stall boundary determined experimentally by McHugh (1978).

For these limit conditions, the designer must determine the performance, the blade loads, and the vibration. Each area has important effects on the aircraft design.

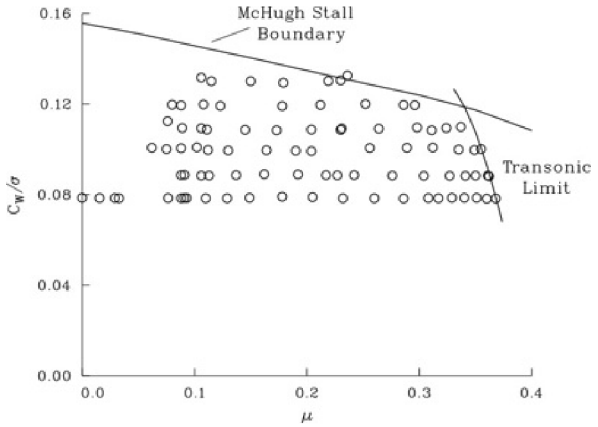

Forward flight performance is characterized by the power required at the maximum level flight speed or the best cruise speed (speed for maximum range). The figure compares the power calculated with CAMRAD II (Yeo et al. 2004) for five weight coefficients. The accuracy of these calculations, based on three different UH-60A flight tests, is an overprediction of about 4%, which is not satisfactory (Bousman and Norman 2008).

The accuracy of the predictions at high speed depends strongly on the parasite power of the helicopter fuselage and the profile power of the rotor blades.

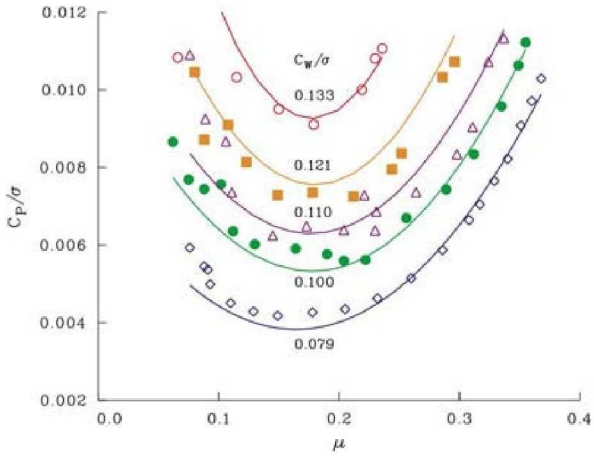

Yeo and Johnson (2005) have evaluated the accuracy of the CAMRAD II code using data from five different rotors. The figure compares the calculated and measured nondimensional flap bending moments. These moments are underpredicted by 27% and there is a large amount of scatter (Bousman and Norman 2008). The accuracy for chord bending and torsion moments is worse. This accuracy is inadequate for design and explains why the designer must rely on scaled test data from previous development programs. If components are underdesigned, such that fatigue damage occurs in level flight, then redesign is required.

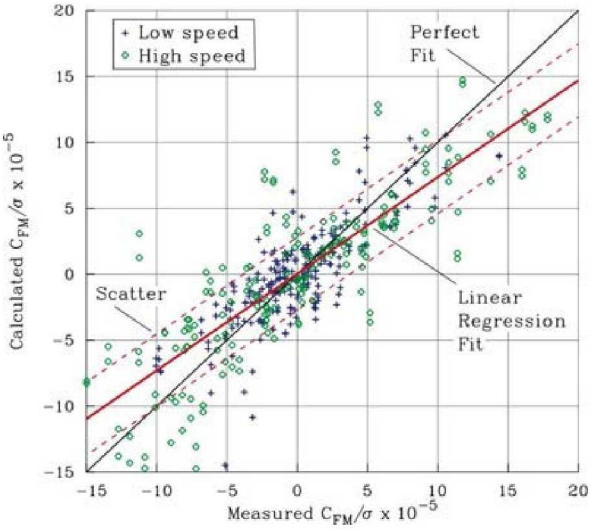

Design for vibration takes into account that rotor blade natural frequencies should be located away from N per rev forcing frequencies. Beyond this, design for reduced vibration is rarely attempted or is successful. Consequently, designers incorporate various fuselage vibration attenuation systems in their designs.

Vibration problems in operations have led the U.S. Army to specify an "Intrusion Index" to define acceptable vibration (Crews 1987). The figure shows that the Airloads Program UH-60A exceeded the Army's ADS-27 limit at nearly all airspeeds. The vibration is particularly excessive at both low and high speeds.

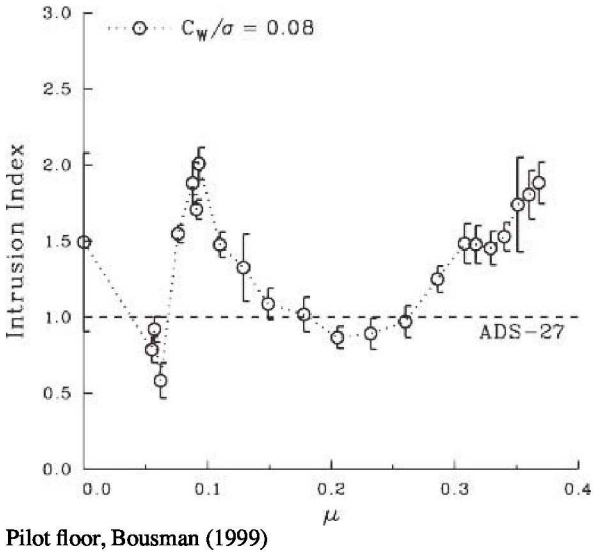

Pilot floor, Bousman (1999)

The figure shows the level flight data as before, but now the weight coefficient is multiplied by the load factor, which allows maneuvers to be included in the figure. Kufeld and Bousman (1998) have examined the maneuvers flown in the Airloads Program and identified the four shown here as the most critical. The designer must include a limited set of critical design maneuvers to insure that rotating- and fixed-system components are sufficiently strong so that they will not fail in flight. Fatigue damage, however, may occur, in which case a replacement "safe life" interval must be specified for the component.

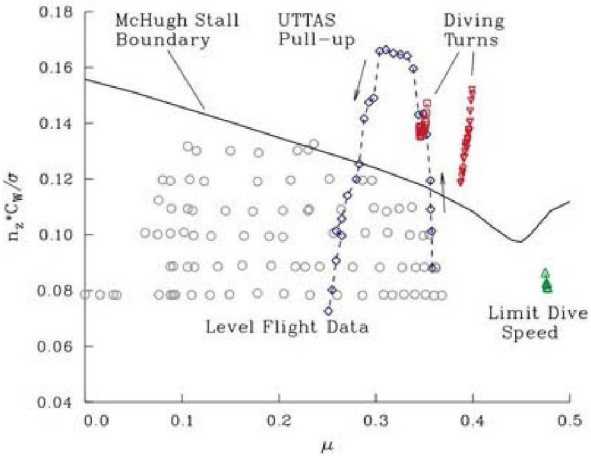

Critical maneuvers identified in the Airloads Program by Kufeld and Bousman (1998) are shown here.

Maximum Load Conditions

Counter 11680, 140 knot, right diving turn (60° bank angle): pitch-link load, torsion moment at 0.30R, and chord bending moment at 0.113R.

Counter 11029, UTTAS maneuver: flap bending moment at 0.113R.

Counter 11682, maximum dive speed (VNE): flap bending moment at 0.60R.

Counter 11659, 120 knot, left diving turn (55° bank angle): chord bending moment at 0.60R.

The UTTAS pull-up maneuver was an Army-specified requirement for the UH-60A. This required that the aircraft pull-up from its maximum level flight speed, achieve a load factor of 1.75g, and hold this load factor for 3.0 seconds without losing more than 30 knots speed.

The figure shows the pitch-link loads during a UTTAS pull-up maneuver flown in the Airloads Program. The maximum loads, ranging from about 2500 to 2860 pounds exceed the loads in level flight by a factor of 2.5 and also exceed the pitch-link endurance limit load.

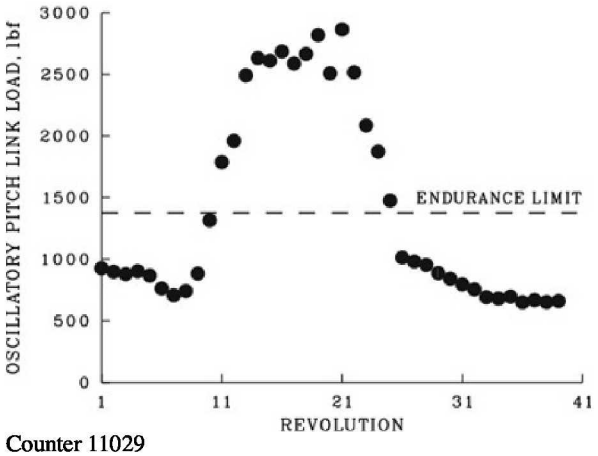

Counter 11029

Peak vibration occurs in transition and at high speed. At high speed the vibration is continuous whereas in transition the vibration tends to be temporary, either as the aircraft approaches a landing site, as shown in the figure, or as it takes off. The harmonic content of vibration differs between transition and high-speed flight, and vibration attenuation or reduction techniques may not be effective in both regimes.

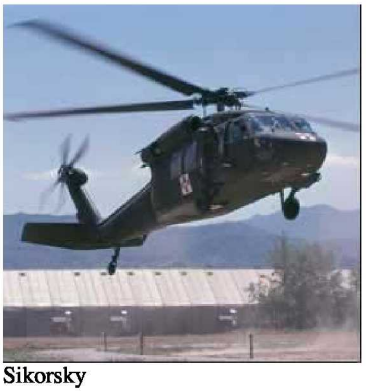

Sikorsky

The FAA requires that civil helicopters meet noise requirements in descending approaches, level flight, and during takeoff. The most difficult requirement is for approach noise, when the blade vortex interactions (BVI) cause severe acoustic radiation. Noise measurements, scaled to a gross weight of 10,000 lbs, are shown in the figure for 38 modern helicopters (Lowson 1993, Cox et al. 1993). Most of these aircraft meet the noise limit, but a few exceed or are close to breaking the limit.

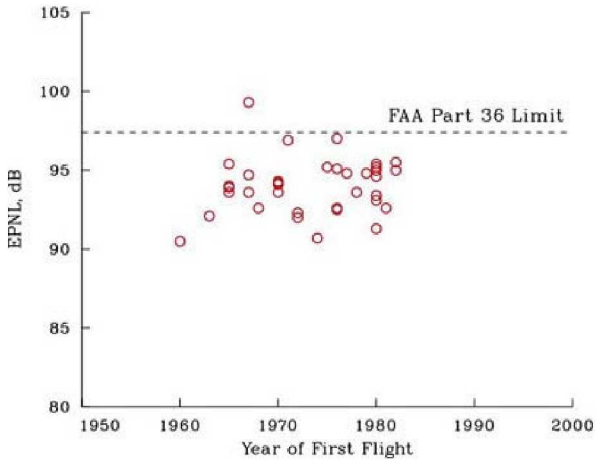

The focus of this chapter is on the aerodynamic forces that make a helicopter work. All of these topics are covered in detail in any basic helicopter text. The purpose of this chapter is to review these topics and provide a basis for the results from the Airloads Program that are covered in Chapter 4.

The chapter begins by looking at the basic aerodynamic characteristics of airfoils that provide the lift a helicopter needs in hover and forward flight. Then, there is a discussion of limits to airfoil performance, both those caused by nonlinearities induced by transonic flow and by dynamic stall.

The rotor wake is discussed next. Particularly at low speed, it is this wake that influences vibration and aircraft noise.

The blade's structural response to aerodynamic loads in examined for flap bending, chord bending, and torsion moments. These loads are important for rotorcraft structural integrity and also for the vibration that is passed through to the fuselage and impairs operation and damages equipment. Finally, brief mention is made of the need for rotor stability in the design of the rotor.

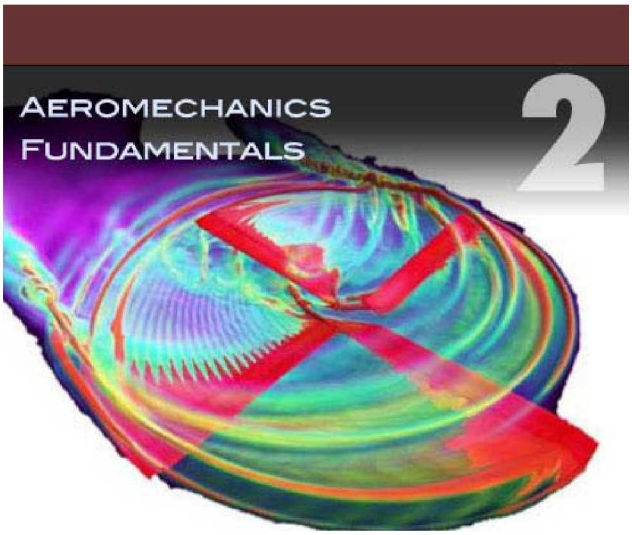

Airfoil lift, drag, and pitching moment depend upon Mach number and angle of attack. At a rotor section

$$V(r,\psi) = \Omega R(\frac{r}{R}) + V_\infty \sin\psi$$

or, in terms of Mach number

$$M(r,\psi) = M_T(\frac{r}{R} + \mu \sin\psi)$$

where M_T is the tip Mach number, which is normally about 0.7. Appropriate Mach numbers for a helicopter airfoil are from near 0 (to account for reverse flow) to about 1 (when $\mu \sim 0.4$).

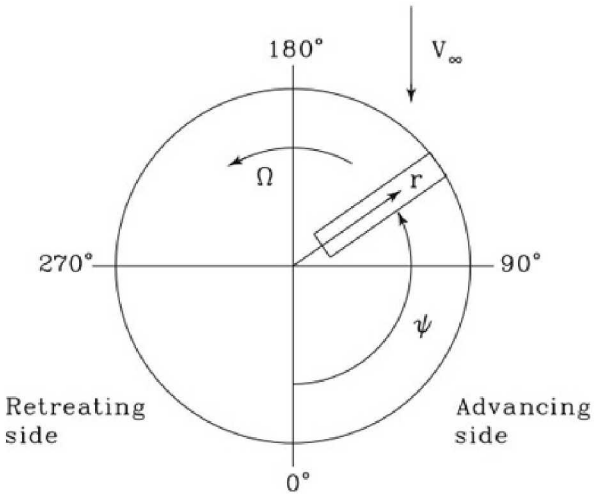

One key attribute of an airfoil section is its lift-to-drag ratio (L/D). Lift is what is desired for a helicopter blade, and drag is the penalty that must be paid. The figure shows the L/D surface of the SC1095 airfoil (one of two) used on the UH-60A blade. The red line shows the maximum L/D, whereas the dashed blue line shows the lift-to-drag ratio at the maximum lift coefficient of the airfoil (where the airfoil stalls). For the greatest efficiency, the rotor blade airfoil sections need to operate as close to the maximum L/D as is possible. Away from the maximum L/D, more drag is required to maintain the lift.

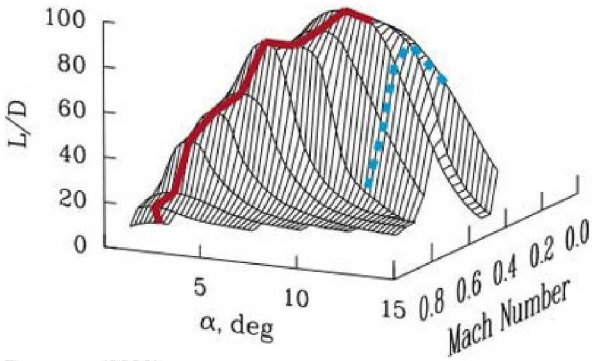

Bousman (2002)

Another way to look at airfoil performance is to examine the airfoil drag, the cost the section must pay for lift. The figure shows the classical "drag bucket" of an airfoil section, in this case, the SC1095. For Mach numbers less than about 0.75, the minimum drag is about the same, regardless of the angle of attack. But within this range, at the lowest Mach numbers, the bucket is quite wide, whereas at higher Mach numbers the bucket narrows. At a Mach number of 0.8, the minimum drag point increases significantly and this is referred to as drag divergence.

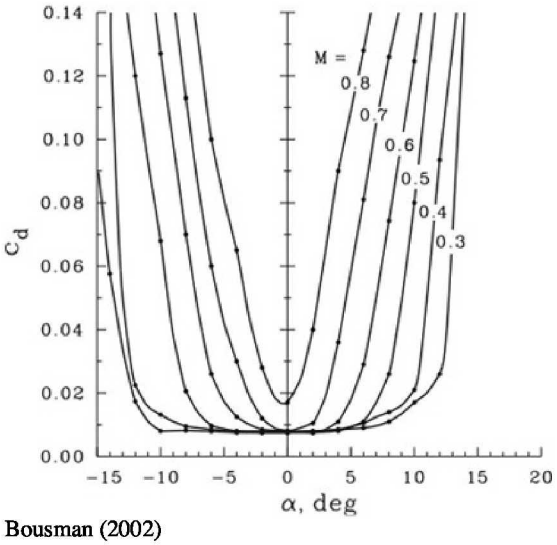

Bousman (2002)

Calculations have been made using the CAMRAD II analysis for the UH-60A for 8 airspeeds. The airfoil section angles of attack and Mach numbers have been computed every 15 deg. of azimuth. These calculated α-M pairs are shown as small crosses in the figure. They follow the maximum L/D curve closely, and all fall within the drag bucket (in this case for the SC1094 R8 section). Both the analysis and the helicopter obtain a solution that minimizes the cost in drag at each airfoil section.

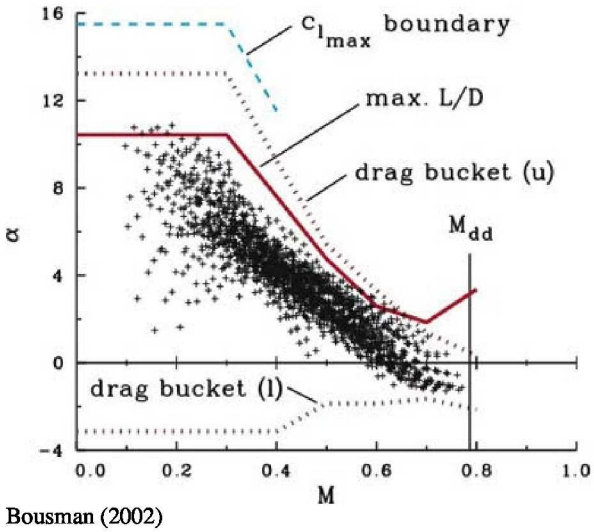

Bousman (2002)

The UH-60A's top speed is limited by power. The drag force on the fuselage and hub, termed the parasite power, increases with the square of velocity. But the drag on the rotor blade, termed the profile power, increases at a greater rate when the blade divergence Mach number is exceeded. Limits based on transonic flow affect the UH-60A primarily below $C_W/\sigma \leq 0.11$ as shown by the red line in the figure. At higher weight coefficients, the airspeed limit is defined by dynamic stall. The airfoil drag beyond the divergence Mach number and dynamic stall both represent nonlinear aerodynamic limits.

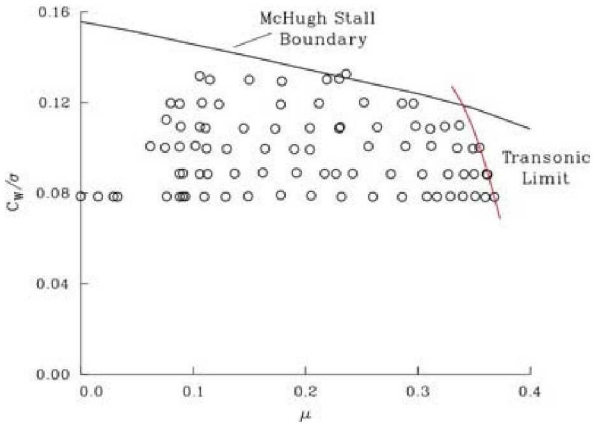

Transonic nonlinearities in airfoil lift, drag, and pitching moment are a result of the development of supersonic flow and strong shock waves on the airfoil. Data are shown for the maximum level flight speed case (Counter 8534, $\mu = 0.37$) and the limit dive speed case (Counter 11682, $\mu = 0.48$). For illustrative purposes the sign of the lower surface data are reversed. At this radial station and azimuth, the section lift on the blade is strongly negative. For the level flight case there is a strong shock on the lower surface, but for the dive case, much stronger shocks are seen on both upper and lower surfaces.

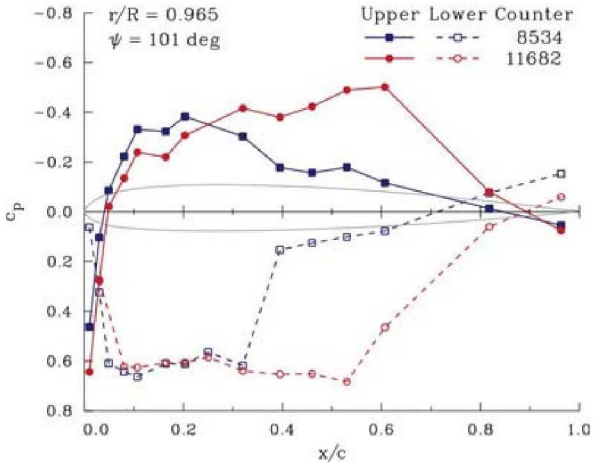

The UH-60A's top speed is limited by transonic flow at lower weight coefficients, but at higher weight coefficients, the speed is limited by dynamic stall. The McHugh boundary shown here was established in a wind tunnel test on a powered rotor model designed to investigate aerodynamic limits. It coincides closely with the limits seen during the UH-60A flight tests.

Dynamic stall is a process where pitching motions allow the airfoil to maintain lift past the static stall limit. But when the airfoil does stall, large excursions in drag and pitching moment result.

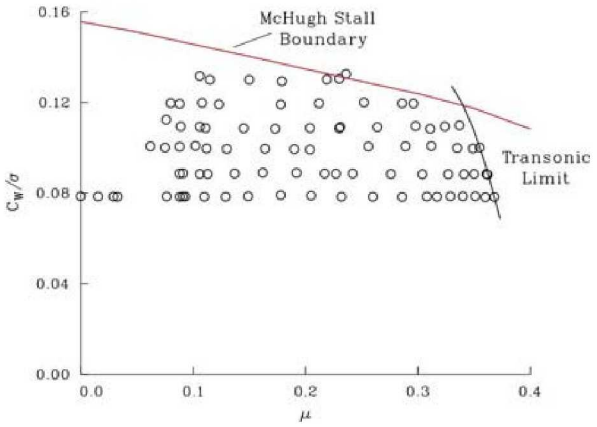

When an airfoil's pitch angle oscillates beyond the static stall boundary, there is an overshoot in lift, which is beneficial for a rotor in maneuver. For the 2D wind tunnel data shown here in Figure 1 for the NACA 0012 (McCroskey et al. 1982), the increase in lift compared to the static value is about 50%. The lift overshoot is caused by a dynamic stall vortex that forms near the forward portion of the airfoil and augments the section lift as it passes along the upper surface. Once the stall vortex leaves the trailing edge, the lift collapses. Although the extra lift is a benefit, the stall vortex also causes excessive drag and pitching moments in dynamic stall, as shown in subsequent figures.

The drag on the section increases rapidly for angles of attack beyond the static stall angle, about 14° for the NACA 0012 section shown in Figure 2. The extremum in drag occurs as the stall vortex leaves the trailing edge and causes massive separated flows. This increase in drag is roughly 20 times the drag that occurs at the static stall angle and greatly increases the power required for the rotor. Whereas the extra lift in dynamic stall is a benefit, the increase in drag is a detriment.

In Figure 3, the moment response to dynamic stall is for the moment to become more negative as the dynamic stall vortex passes along the upper surface of the airfoil. As this vortex leaves the trailing edge, the moment recovers to it normal value near zero. The negative moments in dynamic stall create high loads in the rotating- and fixed-system controls and these high loads in maneuver often size these components. As with drag, the high negative pitching moments associated with dynamic stall are a detriment to the rotor.

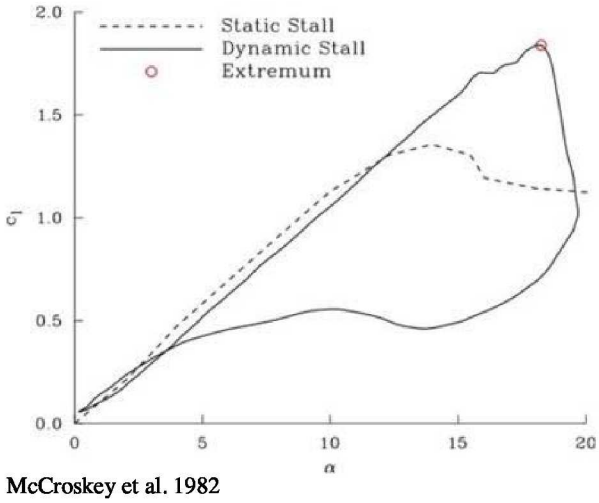

McCroskey et al. 1982

When an airfoil's pitch angle oscillates beyond the static stall boundary, there is an overshoot in lift, which is beneficial for a rotor in maneuver. For the 2D wind tunnel data shown here in Figure 1 for the NACA 0012 (McCroskey et al. 1982), the increase in lift compared to the static value is about 50%. The lift overshoot is caused by a dynamic stall vortex that forms near the forward portion of the airfoil and augments the section lift as it passes along the upper surface. Once the stall vortex leaves the trailing edge, the lift collapses. Although the extra lift is a benefit, the stall vortex also causes excessive drag and pitching moments in dynamic stall, as shown in subsequent figures.

The drag on the section increases rapidly for angles of attack beyond the static stall angle, about 14° for the NACA 0012 section shown in Figure 2. The extremum in drag occurs as the stall vortex leaves the trailing edge and causes massive separated flows. This increase in drag is roughly 20 times the drag that occurs at the static stall angle and greatly increases the power required for the rotor. Whereas the extra lift in dynamic stall is a benefit, the increase in drag is a detriment.

In Figure 3, the moment response to dynamic stall is for the moment to become more negative as the dynamic stall vortex passes along the upper surface of the airfoil. As this vortex leaves the trailing edge, the moment recovers to it normal value near zero. The negative moments in dynamic stall create high loads in the rotating- and fixed-system controls and these high loads in maneuver often size these components. As with drag, the high negative pitching moments associated with dynamic stall are a detriment to the rotor.

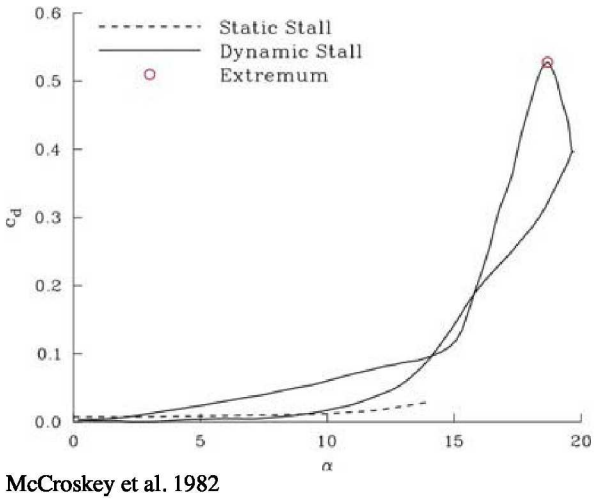

McCroskey et al. 1982

When an airfoil's pitch angle oscillates beyond the static stall boundary, there is an overshoot in lift, which is beneficial for a rotor in maneuver. For the 2D wind tunnel data shown here in Figure 1 for the NACA 0012 (McCroskey et al. 1982), the increase in lift compared to the static value is about 50%. The lift overshoot is caused by a dynamic stall vortex that forms near the forward portion of the airfoil and augments the section lift as it passes along the upper surface. Once the stall vortex leaves the trailing edge, the lift collapses. Although the extra lift is a benefit, the stall vortex also causes excessive drag and pitching moments in dynamic stall, as shown in subsequent figures.

The drag on the section increases rapidly for angles of attack beyond the static stall angle, about 14° for the NACA 0012 section shown in Figure 2. The extremum in drag occurs as the stall vortex leaves the trailing edge and causes massive separated flows. This increase in drag is roughly 20 times the drag that occurs at the static stall angle and greatly increases the power required for the rotor. Whereas the extra lift in dynamic stall is a benefit, the increase in drag is a detriment.

In Figure 3, the moment response to dynamic stall is for the moment to become more negative as the dynamic stall vortex passes along the upper surface of the airfoil. As this vortex leaves the trailing edge, the moment recovers to it normal value near zero. The negative moments in dynamic stall create high loads in the rotating- and fixed-system controls and these high loads in maneuver often size these components. As with drag, the high negative pitching moments associated with dynamic stall are a detriment to the rotor.

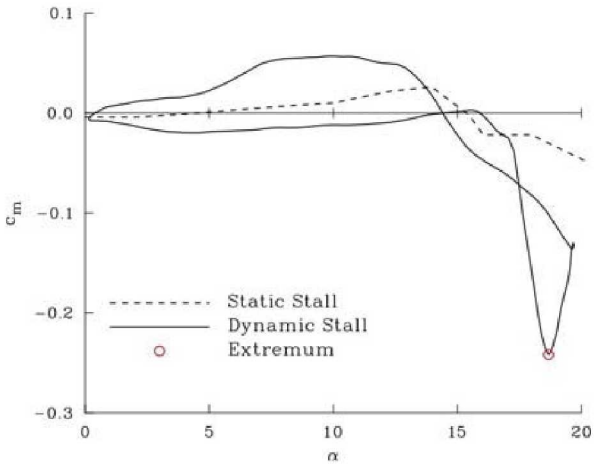

The airfoil dynamic stall overshoot shown in the previous tab, depends upon the range of pitch oscillations and the frequency of the oscillations. The extrema of the lift, drag, and pitching moments for a wide range of conditions are shown here for the SC1095 airfoil (McCroskey et al. 1982). The data show that as lift is increased (which is good), so are drag and pitching moment (which is bad). The static stall characteristics are shown by the solid line. Below the static stall, the lift is linearly proportional to angle of attack, and the drag and pitching moment are constant. But when dynamic stall occurs, there are nonlinear behaviors in all of these aerodynamic parameters.

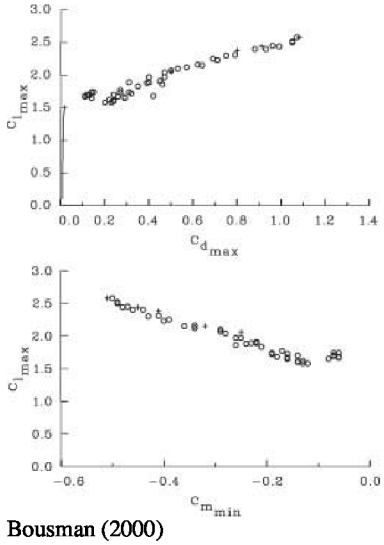

Bousman (2000)

In a 2D wind tunnel test, the angle of attack is known, but this is not the case for flight test. Thus, integration of the blade pressures provides normal force instead of lift, and the viscous drag cannot be determined from the integration. The figure shows the extrema in normal force and pitching moment measured on the UH-60A during the multiple cycles of a maneuver where the aircraft encounters dynamic stall. These flight extrema are compared with a polynomial fit of the 2D wind tunnel data for the same airfoil. In this case, the agreement is remarkably good, indicating that at this radial station, what we have learned from 2D wind tunnel tests can be directly applied to flight.

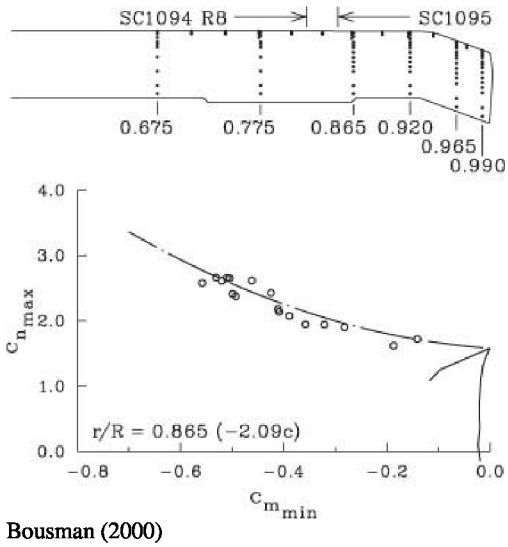

Bousman (2000)

For a helicopter, the angle of attack of the airfoil section, $\alpha(r,\Psi)$, is a combination of the geometric pitch angle, $\Phi(r,\Psi)$, and the induced flow angle, $\Phi(r,\Psi)$. The geometric angle is comprised of the control angles: collective, lateral, and longitudinal pitch, and the elastic twist (which in some flight conditions may be as high as ±3°). The induced flow angle for a section depends upon wake-induced flow from its own blade, as well as from the other rotor blades. This angle also depends on the blade coning and elastic flap and lead-lag motions. The resulting angle may sometimes be half as big as the geometric pitch, quite different from the fixed-wing case.

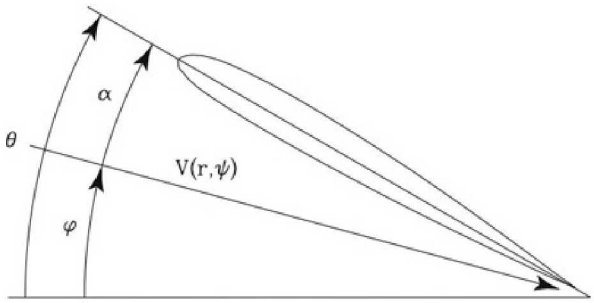

The figure shows a calculation for the UH-60A at $\mu = 0.15$, where the calculated vorticity in the flowfield is used to visualize the individual blade tip vortices. The flow in this figure is approaching from the lower right. The tip vortices from each blade remain distinct over the front and rear of the disk plane. But on the right and left sides, the tip vortices twist around each other and merge into a larger vortex, called the disk vortex. Either individually or in combination, the concentrated tip vortices in the rotor wake strongly influence the induced flow angle that the airfoil section sees and are a source of oscillatory loading on the blades.

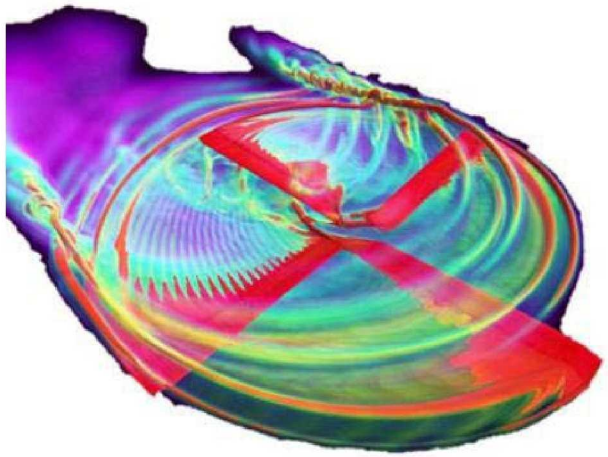

Mark Potsdam

At low speed in level flight (μ = 0.09 for the UH-60A here, 3-120 harmonics plotted), the disk vortices cause a powerful down-up pulse on the advancing side (here near 45°) and an up-down pulse on the retreating side (about 300°) in this offset plot. The azimuthal spacing of the loading suggests that the "core" of the combined tip vortices from previous blades, entwined in one large vortex, is about 10 times the blade chord. The spacing of this loading is such that it excites lower blade frequencies, particularly near 3 to 5/rev, causing the high vibration that is typical at low speeds or in transition flight.

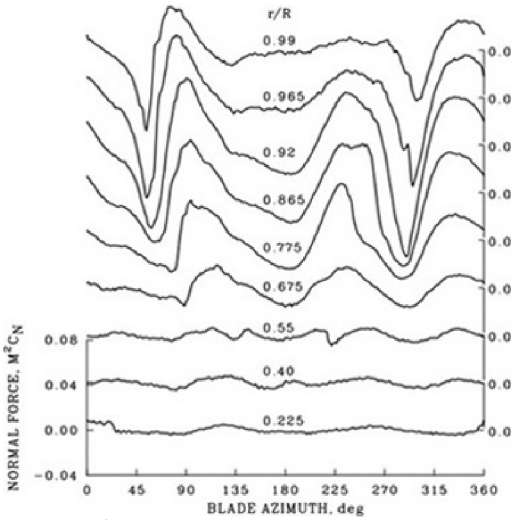

Counter 8517

For descending conditions in low speed flight, as shown in Figure 1 for an increasing tip path plane angle ($\mu = 0.10$), the disk vortices are apparent for all descent cases (3-120 harmonics). The tip path plane angles, α_{TPP}, range from -0.8°, corresponding to level flight up to 13.7°, which is equivalent to a flight path angle of about −15°. The disk vortex is little changed over this range of flight path angles. But the effects of individual blade vortices can be seen, imposed on the disk vortices. These can be examined more closely by plotting only 17-120 harmonics (a high-pass filter), which can be seen by clicking the button at the bottom.

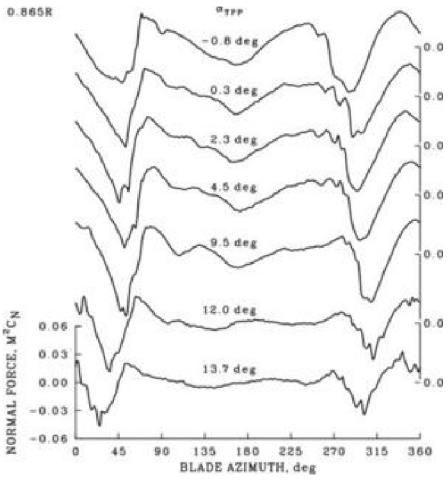

Figure 2. Individual blade vortex interactions (BVI) are seen on both sides of the rotor disk as the vortices wrap around to form the disk vortex (17-120 harmonics). The spacing of the loading suggests that the "core" of each tip vortex is about the same size as the blade chord. The BVI loading is too high in frequency to cause blade vibrations, but instead radiates acoustic energy that causes significant annoyance in neighboring communities as the helicopter approaches its landing site. The BVI loading is particularly noticeable at typical helicopter approach speeds between $\mu = 0.15$ a

For descending conditions in low speed flight, as shown in Figure 1 for an increasing tip path plane angle ($\mu = 0.10$), the disk vortices are apparent for all descent cases (3-120 harmonics). The tip path plane angles, α_{TPP}, range from -0.8°, corresponding to level flight up to 13.7°, which is equivalent to a flight path angle of about −15°. The disk vortex is little changed over this range of flight path angles. But the effects of individual blade vortices can be seen, imposed on the disk vortices. These can be examined more closely by plotting only 17-120 harmonics (a high-pass filter), which can be seen by clicking the button at the bottom.

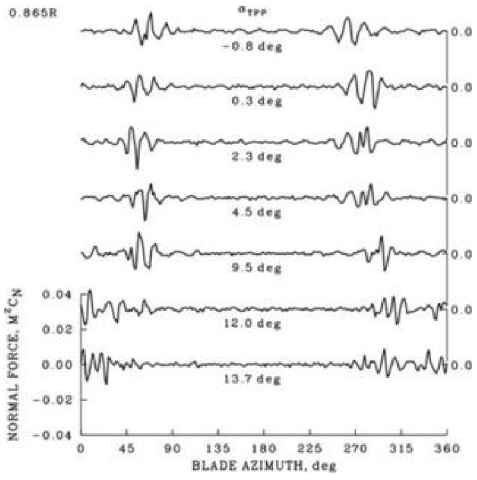

Figure 2. Individual blade vortex interactions (BVI) are seen on both sides of the rotor disk as the vortices wrap around to form the disk vortex (17-120 harmonics). The spacing of the loading suggests that the "core" of each tip vortex is about the same size as the blade chord. The BVI loading is too high in frequency to cause blade vibrations, but instead radiates acoustic energy that causes significant annoyance in neighboring communities as the helicopter approaches its landing site. The BVI loading is particularly noticeable at typical helicopter approach speeds between $\mu = 0.15$ a

In engineering beam theory, rotor blades are modeled as slender elastic beams. Because much of the loading is carried by centrifugal force, the blade sections are much thinner than the wing sections on an airplane that must support cantilever loads. At its simplest, the solution for the blade mass and stiffness is found by the superposition of blade modes, just as sound on the strings of a violin is based on vibratory modes. The approximations of modal theory have been used since the earliest helicopters, but today the approach has been replaced with finite element theory, which offers greater flexibility in modeling.

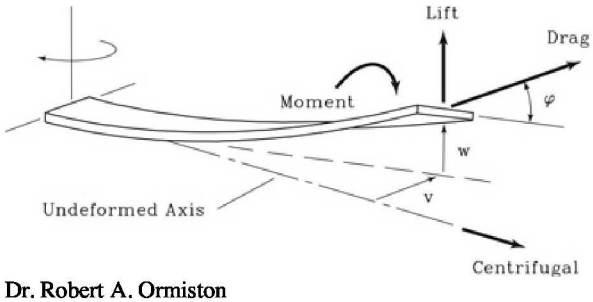

Dr. Robert A. Ormiston

Flap bending moments are comprised of steady moments, caused largely by centrifugal forces, and unsteady moments dependent upon the flight condition. The figure shows the steady flap bending moments along the blade of the UH-60A for the Flight 85 airspeed sweep. The 19 cases range from hover to the maximum level flight speed. The unsteady loads vary greatly over this speed range, but the steady loads show little effect of airspeed. These steady loads are largely caused by centrifugal forces rather than aerodynamic forces.

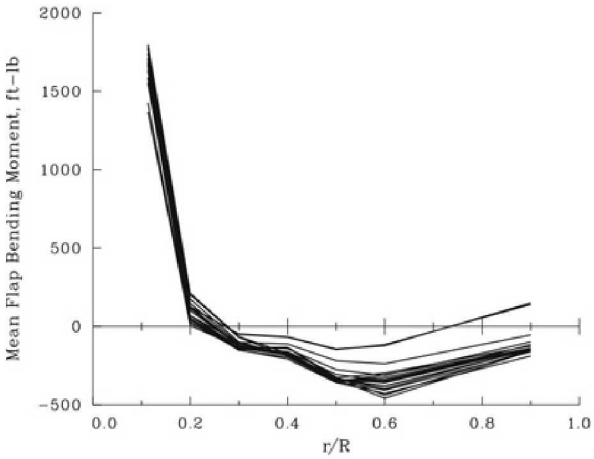

" = 0.08 Airspeed Sweep"

Unsteady flap bending moments are caused by the unsteady airloads on the blades. The figure shows the half peak-to-peak loads along the blade for airspeeds ranging from hover, where the loads are benign, to the maximum level flight speed, where the loads are greatest. Generally, the increase in loads is proportional to airspeed. This is quite different from the steady loads shown on the previous tab. The highest unsteady blade loads on the blade occur either near the blade root, or midspan at about 0.60R.

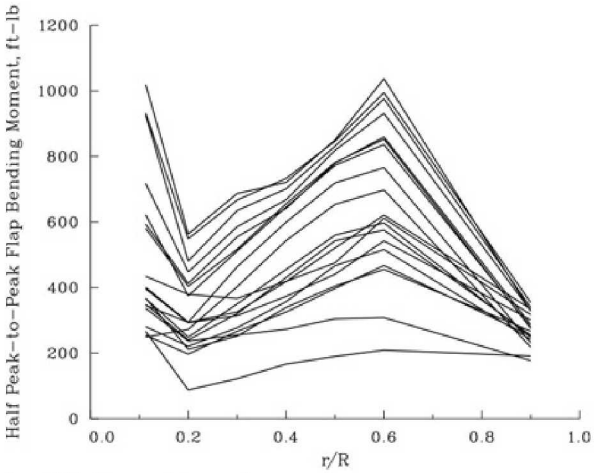

" = 0.08 Airspeed Sweep"

As with the flap bending moments, chord bending moments are comprised of steady moments and unsteady moments. The figure shows the steady chord bending moments along the blade of the UH-60A for the same flight conditions as was shown previously for the flap bending moments. There is some variation in the steady loads with airspeed, but the loading is largely dominated by centrifugal force, not unsteady aerodynamic forces. One of the factors that affects these centrifugal loads is the offset between the section center of gravity and the tensile axis. This offset is difficult to calculate and difficult to measure but has a significant effect on the steady chord bending moments (Sharpe 1986).

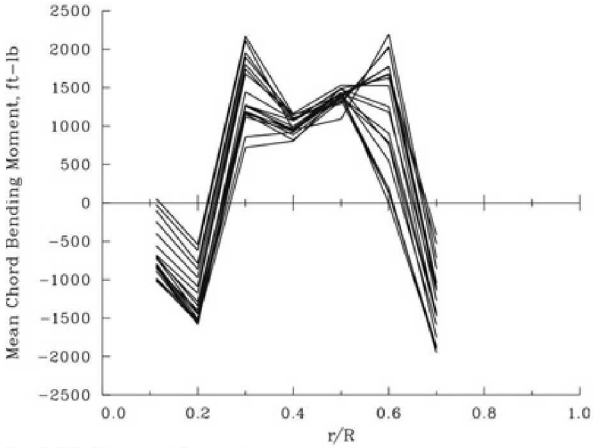

" = 0.08 Airspeed Sweep"

Unsteady chord bending moments are caused by the unsteady airloads on the blades and are also strongly affected by the damper loads, particularly inboard on the blade. The figure shows the half peak-to peak chord bending moments for the $C_W/s = 0.08$ airspeed sweep. The advance ratio varies from hover, where the unsteady moments are least, to the maximum level flight speed, where the loads are the greatest. Generally, the loads are proportional to airspeed and this pattern is quite different from the steady loads observed on the previous tab, which are dominated by centrifugal forces.

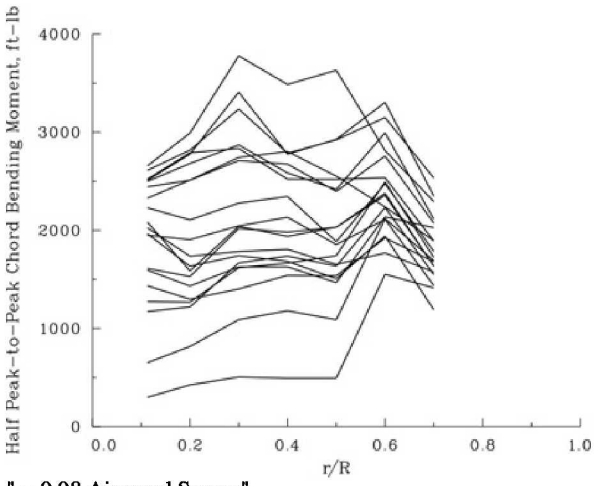

" = 0.08 Airspeed Sweep"

The steady torsion moments are caused largely by steady aerodynamic pitching moments on the cambered airfoils, although there are centrifugal force effects as well. The steady or mean torsion moment here are shown for one airspeed sweep where the speed varies from hover to the maximum flight speed. By comparison with the steady flap and chord bending moments, there appears to be a greater influence of the flight speed on these steady moments. For the data shown here, the inboard torsion moment has been derived from the mean of the four measured pitch-link loads.

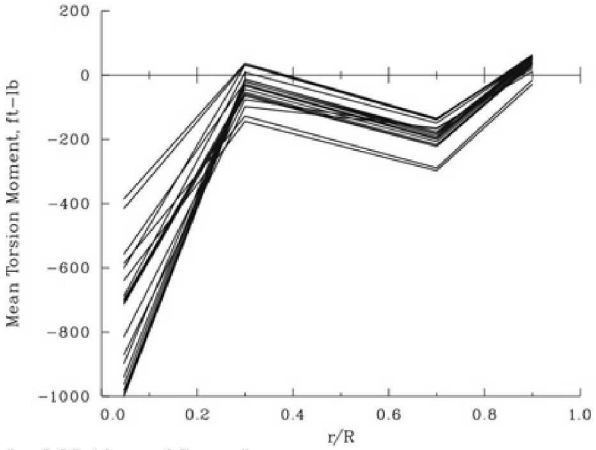

" = 0.08 Airspeed Sweep"

The half peak-to-peak (unsteady) torsion moments are caused by the unsteady pitching moments on the blade and these increase from the blade tip to root. As with the unsteady flap and chord bending moments, the loads increase with flight speed. These loads are minimal in hover, and are greatest at the maximum level flight speed.

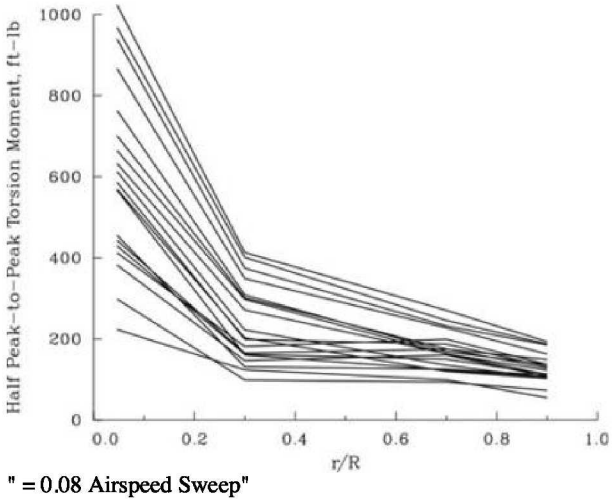

" = 0.08 Airspeed Sweep"

Unsteady flap and chord bending moments are shown here at 0.50R as harmonics. Typically, these moments decrease ("roll-off") with increasing harmonic number, but near blade mode natural frequencies there may be some increase; for instance, near 3/rev for flap bending and 4/rev for chord bending. The blade bending moments combine at the rotor hub as hub moments and shears. But some cancel whereas others are transmitted. For a four-bladed rotor, such as the UH-60A, flap bending moments at 4/rev and 8/rev are transmitted (blue stars) and for the chord bending moments, they are transmitted at 3/rev, 5/rev, 7/rev, and 9/rev (red stars). The other loads

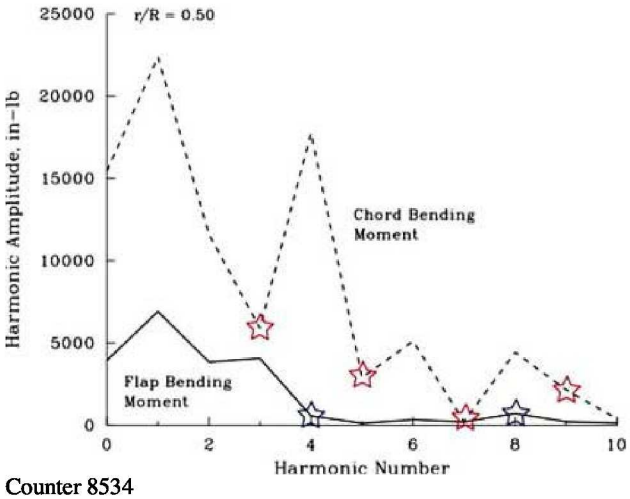

Counter 8534

The cancellation of rotating system loads occurs in theory, but not always in practice. The Army's "Intrusion Index" addresses this reality by calculating the index based on the four largest components of acceleration, regardless of whether they occur at the expected per rev frequency or not. For the peak transition vibration on the UH-60A, at about $\mu = 0.1$, most of the vibration is at the expected per rev frequency (90% of the total). But in high speed flight the normal 4/rev vibration is only 67% and the rest is made up of unexpected frequencies, such as 2/rev and 3/rev.

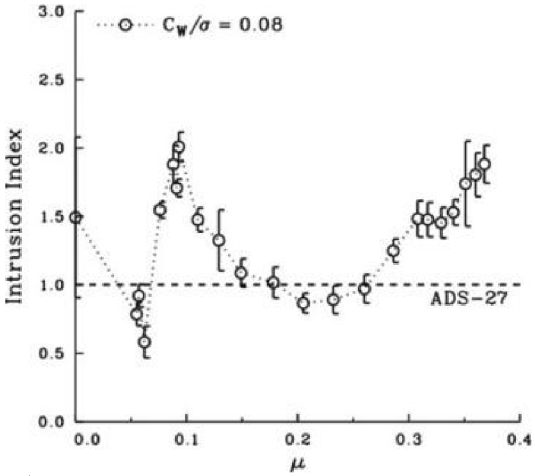

Pilot floor, Bousman (1999)

The helicopter rotor must be stable in all flight conditions. The AH-56A Cheyenne encountered numerous unpredicted rotor stability problems during its development in the 1960s, including one instability that caused a fatal crash off Oxnard, California and another that destroyed an aircraft being tested in the NASA Ames 40- by 80-Foot Wind Tunnel. Some of the development problems were related to the helicopter's stiff inplane rotor and gyro rotor control. Subsequently, newer designs have focused on soft inplane rotors that require appropriate dampers to control air and ground resonance instabilities. But damper design for these configurations remains a formidable problem.

A time history of the measured normal force on a UH-60A blade section, as shown here, can also be represented by a Fourier series (harmonics). Shown in magenta are the first four harmonics of the Fourier series. The time series and harmonic series are equivalent representations and require the same data storage. It is convenient in either the time or frequency domains to show only a range of harmonics. For instance, to understand blade vibratory loads, that is, loads 3/rev and above, it is useful to plot only the 3rd harmonic and above-this is like a high-pass filter. Similarly, to avoid the effects of noise in the data, a plot may show only 0-10 harmonics-this is like a low-pass filter.

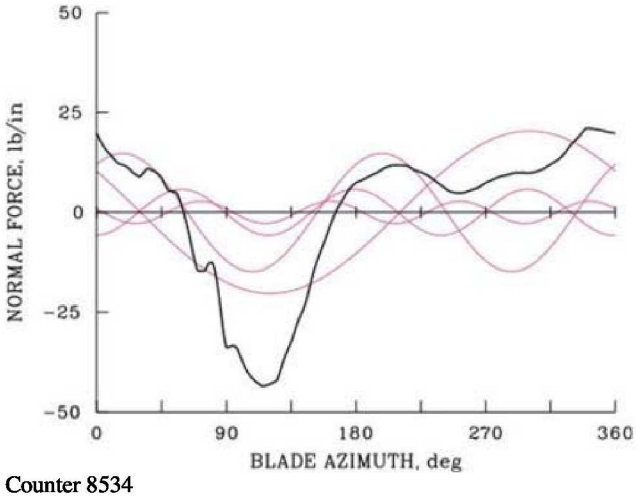

Counter 8534

This chapter starts out by discussing the need for experimentation on the UH-60A, including how the flight program fits into other test programs. Then, a general outline is given of the instrumentation installed on the test aircraft.

A sequence of panels addresses instrumentation calibration. Generally, sensors were linear in their response. The classic approach, where the sensor was calibrated in the laboratory to determine its scale factor and an offset was determined on installation, was used for most sensors. But a few adjustments to this approach are examined. In addition, a limited number of sensors required nonlinear calibration and these are discussed.

The primary focus of the aircraft experiments was the measurement of blade pressures and their integration to obtain forces and moments. A general review of this process and a discussion of typical failure modes is provided.

Finally, there are a number of measurements that can be compared with other measurements and the degree of agreement is a final check on the adequacy of the calibrations and the test approach.

The design of a helicopter, such as the UH-60A, requires balancing many requirements and objectives (Leoni 2007). Achieving that balance, for example, sizing the hub and blade hinges correctly to carry maneuver loads while retaining a minimum size of the hub to reduce drag, requires the designer to use the best analytical tools available and to combine these with previous data, design experience, and sometimes guesses. The purpose of the UH-60A Airloads Program flight experiments was to obtain extensive rotor measurements that would provide the technical community with data to develop improved analyses that can be used by the designer.

Flight International

In the 1980s, NASA and the US Army, following discussions with the helicopter companies, developed a program to obtain detailed blade pressure data on a 0.17-scale model of the UH-60A in the DNW wind tunnel in the Netherlands, on a full-scale UH-60A helicopter in flight at NASA Ames Research Center, and with the same blades tested at full scale in the 40- by 80-Foot Wind Tunnel, also at Ames Research Center. The model-scale tests were completed at the DNW wind tunnel in 1989. The full-scale flight tests, finished in 1993 and 1994, are described in this tutorial. The full-scale wind tunnel tests are now planned for 2009.

The UH-60A Airloads Aircraft was instrumented with about 480 sensors. These sensors (numbers in parentheses) are categorized as:

- blade pressures (242)
- blade temperatures (50)
- blade strain and acceleration (56)
- blade root motion (15)
- fuselage and hub accelerometers (40)
- aircraft state (51)
- health and miscellaneous (26)

Approximately 370 of these sensors were in the rotating system, whereas the remainder were in the fixed system.

The 242 absolute pressure transducers were placed in nine radial arrays on the rotor blade, with slightly fewer transducers on the lower surface than the upper. The radial arrays were concentrated toward the blade tip, where the airloads are greatest. But note that there were also a few transducers located at intermediate radial stations near the leading edge of the blade.

These were installed to better study blade vortex interactions (BVIs). The pressure transducers were not temperature compensated, but the local temperature was measured at 50 locations along the blade. As of yet, no temperature corrections have been applied to the pressure measurements.

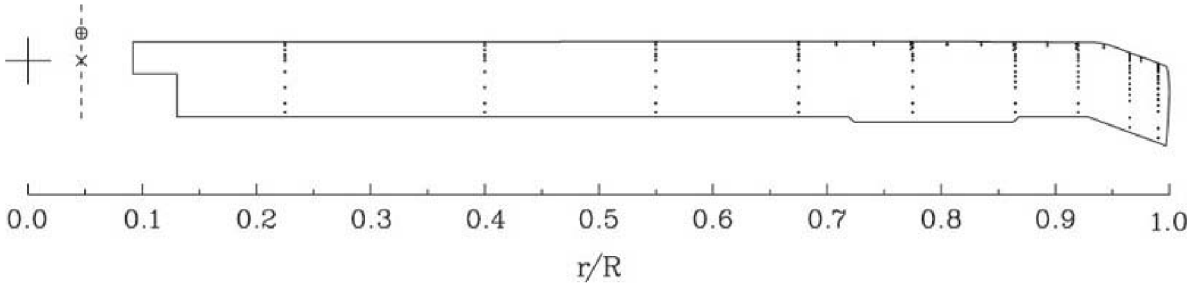

The strain gauge and motion blade had strain measurements at nine radial stations, although not every station had all three measurements.

Accelerometers were built into the blade at four stations. At each station there were two accelerometers in flapping (each offset from the pitch axis for torsion response) and one in chord. Other blades had limited bending measurements.

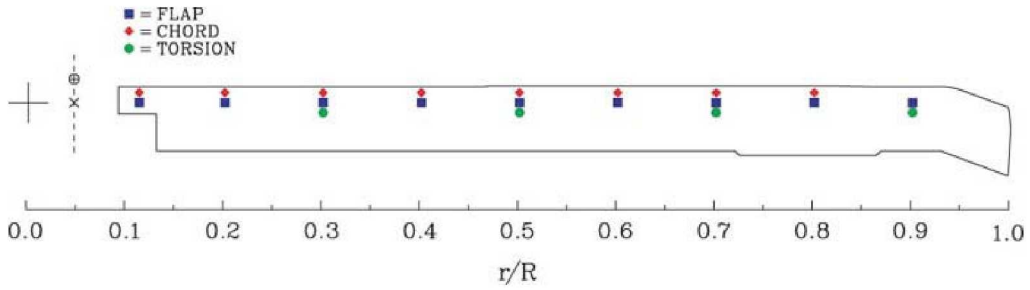

Although the UH-60A is classified as an articulated or hinged helicopter, there are no actual hinges at the blade root that can be used for angular measurements. Rather, the blade motions occur around elastomeric bearings and the "hinges" are the focal points of the bearings. To measure the blade motions about these focal points, a combination of RVDTs and links, referred to as the Blade Motion Hardware (BMH) or "crab arm," connect the blade root to the hub. A crab arm is installed on each blade and, after calibration, provides measurements of the blade flap, lead-lag, and pitch angles.

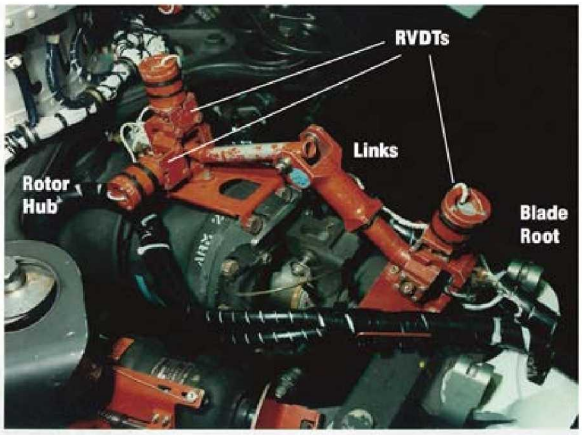

Accelerometers were installed in both the fuselage and on the rotor hub. The fuselage accelerometer locations are shown in the figure as red dots. At most of these locations uni-axial or bi-axial accelerations were measured. Tri-axial measurements in the nonrotating system were only obtained from a location beneath the pilot's seat and a second location at the aircraft center of gravity. In the rotating system, tri-axial measurements were obtained on the rotor hub. In addition, acceleration was measured on each of the hub bifilar vibration absorbers.

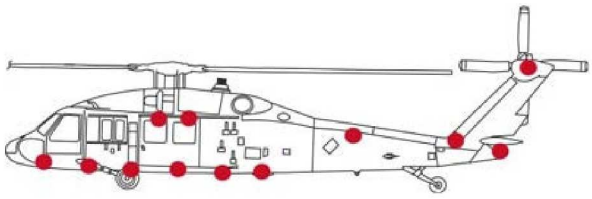

A generation ago, basic aircraft state parameters, such as airspeed, rate of climb, and aircraft attitudes, rates, and accelerations, were recorded from a photo panel, as shown here. Now, all these parameters, are measured and recorded directly onto magnetic tape.

What lingers from the photo panel days is the term "counter," which was used to keep track of each test point as a flight card was flown. On the photo panel, this was a physical counter that synchronized all recorded data. Today, the word "counter" is still used to describe a test point, and that term is used throughout this tutorial.

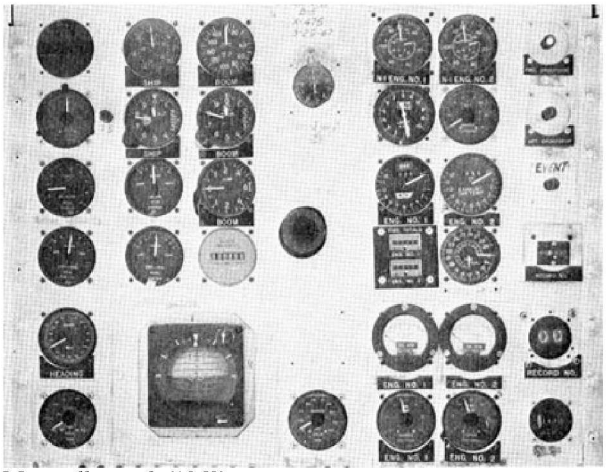

Mattmuller et al. (1969)

The solution to recording so much data from the rotor measurements was to sample the data in the rotating system (A/D) and transmit these data through slip rings to the data recorders in the fuselage as a pulse code modulation (PCM) signal. This was done with the Rotating Data Acquisition System (RDAS). The design of this system was considered to be state of the art in the late 1980s (Kufeld and Loschke 1991). The RDAS shown here was the third design attempted, indicating the great difficulty of achieving high data rates. As the RDAS rates were limited, there was a trade-off between word size and sample rate, and that balance was difficult to achieve.

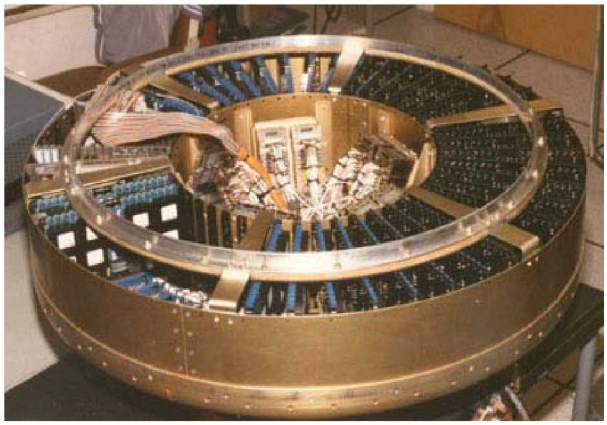

Linear calibrations take the form:

P=mx+b

where P is the output (engineering units), m is the scale factor, b is the offset, and x is the variable being measured. The figure shows the laboratory calibration of the pressure transducer that was installed near the leading edge of the blade at $0.92R$. The scale factor in this case is linear and the offset is near zero. The final value of m depends not just on the slope from the calibration shown here, but in every step of the electronics that takes place from transducer to final data.

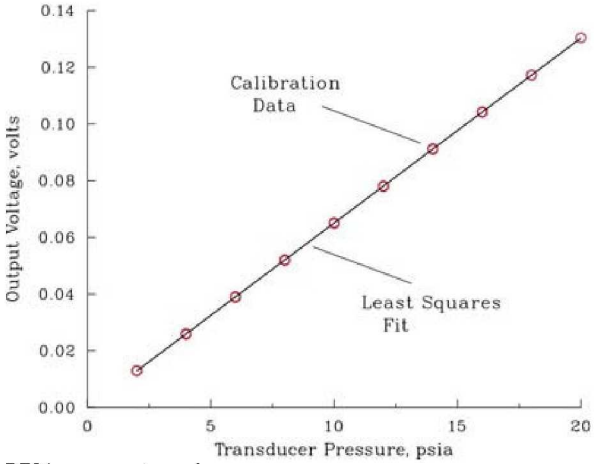

P701 pressure transducer

The offset is defined:

b=P(0)-mx

Prior to and after flight, with the aircraft shut down, measurements were recorded for all parameters ("static cals"). For many parameters the $P(0)$ value was set as zero, but others took on an external measurement or a pre-specified value. For example, the figure shows the outside air temperature static cals that were used to set $P(0)$. Similarly, for blade pressure transducers, the static pressure measurement at the aircraft was used. For the blade strain gauges, calculated offsets were employed.

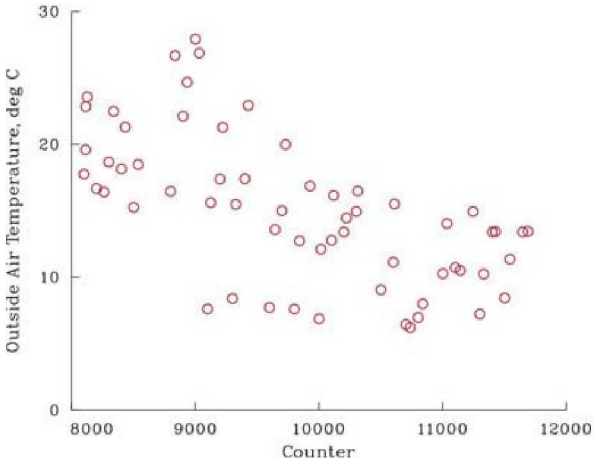

Scale factors were based on laboratory calibrations for most parameters. But in the case of the pressure transducers, intermittent calibrations were made during the flight test program. The calibration was done with the blade mounted on the aircraft or sometimes, as shown here, with the blade off the aircraft. A bag surrounded the entire blade and was sealed. A pump was used to reduce the pressure within the bag to provide for the calibration. The scale factors were computed and moved to the ground station for use during data reduction on subsequent flights.

The flap and chord bending gauges on the blade were calibrated in the laboratory with the blade mounted rigidly at the root. The blade root was positioned at 0 and 180 deg. for the positive and negative flap bending calibration (negative flap bending calibration shown here). For the chord bending calibration, the blade root was positioned at 90 and 270 deg. Calibration loads were applied near the blade tip. The torsion strain gauges were calibrated with the blade mounted vertically, and pure moments were applied near the tip of the blade.

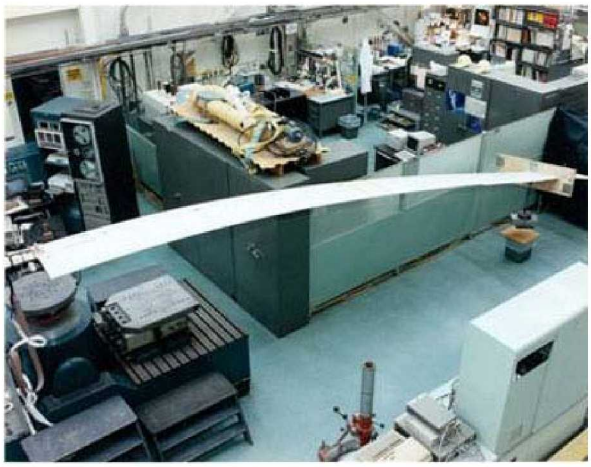

Because of the blade's built-in twist, cross-coupling terms occurred at radial stations outboard of the blade root during the laboratory calibration. The flight data were reduced using only the diagonal terms from the calibration and the off-coupling terms were neglected. It is possible, however, to reprocess the data to examine the effects of the neglected cross-coupling terms. As shown in Figure 1, the flap bending moment is essentially the same whether the cross-coupling terms are included or not.

Figure 2. The chord bending moment is more strongly affected by the off-diagonal terms from the calibration than the flap bending moment. Nonetheless, the differences are slight.

Figure 3. The torsion moment is the most strongly affected blade moment, depending upon whether the diagonal terms of the calibration matrix are used alone or the off-diagonal terms are included. It is expected that the importance of the off-diagonal terms will become greater for radial stations farther from the blade root. But a calibration that uses a 3x3 matrix requires that all measurements at a radial station be satisfactory, and this was not the case for any of the stations outboard of 0.30R.

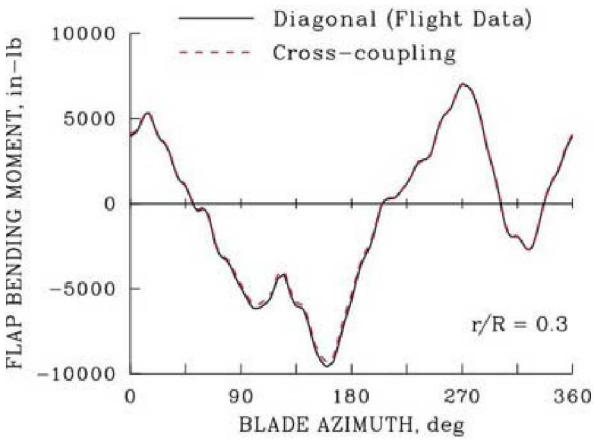

Counter 8534, courtesy of Dr. Hyeonsoo Yeo

Because of the blade's built-in twist, cross-coupling terms occurred at radial stations outboard of the blade root during the laboratory calibration. The flight data were reduced using only the diagonal terms from the calibration and the off-coupling terms were neglected. It is possible, however, to reprocess the data to examine the effects of the neglected cross-coupling terms. As shown in Figure 1, the flap bending moment is essentially the same whether the cross-coupling terms are included or not.

Figure 2. The chord bending moment is more strongly affected by the off-diagonal terms from the calibration than the flap bending moment. Nonetheless, the differences are slight.

Figure 3. The torsion moment is the most strongly affected blade moment, depending upon whether the diagonal terms of the calibration matrix are used alone or the off-diagonal terms are included. It is expected that the importance of the off-diagonal terms will become greater for radial stations farther from the blade root. But a calibration that uses a 3x3 matrix requires that all measurements at a radial station be satisfactory, and this was not the case for any of the stations outboard of 0.30R.

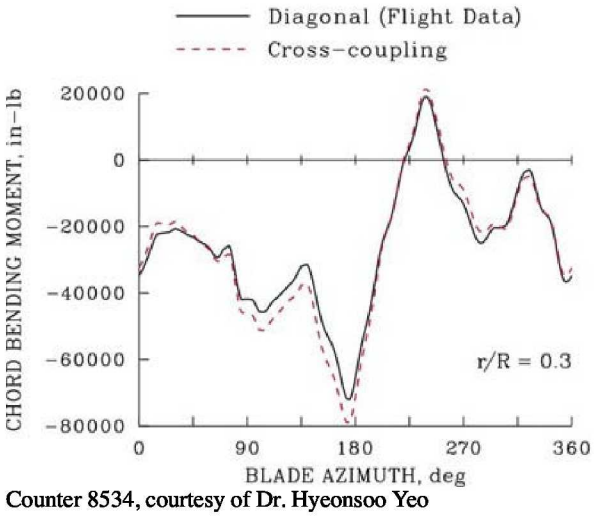

Counter 8534, courtesy of Dr. Hyeonsoo Yeo

Because of the blade's built-in twist, cross-coupling terms occurred at radial stations outboard of the blade root during the laboratory calibration. The flight data were reduced using only the diagonal terms from the calibration and the off-coupling terms were neglected. It is possible, however, to reprocess the data to examine the effects of the neglected cross-coupling terms. As shown in Figure 1, the flap bending moment is essentially the same whether the cross-coupling terms are included or not.

Figure 2. The chord bending moment is more strongly affected by the off-diagonal terms from the calibration than the flap bending moment. Nonetheless, the differences are slight.

Figure 3. The torsion moment is the most strongly affected blade moment, depending upon whether the diagonal terms of the calibration matrix are used alone or the off-diagonal terms are included. It is expected that the importance of the off-diagonal terms will become greater for radial stations farther from the blade root. But a calibration that uses a 3x3 matrix requires that all measurements at a radial station be satisfactory, and this was not the case for any of the stations outboard of 0.30R.

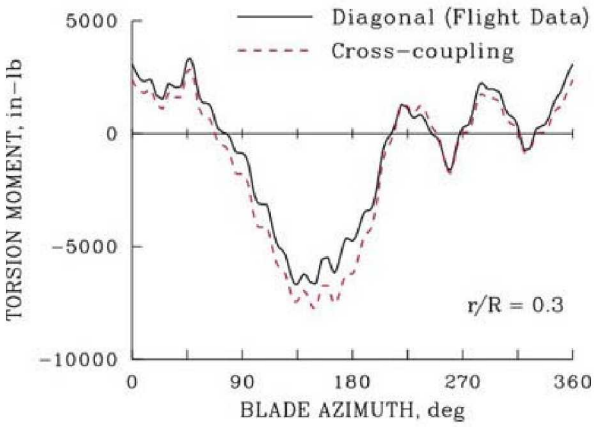

The Blade Motion Hardware (BMH) or "crab arm" is made up of 3 RVDTs connected by linkages. The RVDTs are linear sensors that record angular deflections, but the relationship between the RVDTs and blade root angles is nonlinear. The various constants in the nonlinear equations were identified through calibration. The calibration data for each blade was obtained by positioning the blade at different flap, lead-lag, and pitch angles as shown in the photo. The process was time consuming and required somewhat more than a day's time for each blade. It was done once for the flight test program.

The UH-60A used two airspeed systems. For airspeeds below 20 knots, a Helicopter Airspeed Data Sensor (HADS) was used, while at higher speeds, the airspeed was measured with a pitot-static system on the test boom. The low-speed system was calibrated using a laser tracking system (and wind corrections were measured with balloon-borne anemometry). The high-speed system was calibrated, as shown here, from 80 to 160 knots using a T-34 aircraft with two independent calibrated airspeed systems. From about 20 to 70 knots, the high-speed system was calibrated using a pace car on the airfield runway.

The flight controls, including the pilot's collective, cyclic stick, and pedals showed slightly nonlinear behavior when the sensor output is compared to position measurements. To accommodate the slight nonlinearity, the calibration curve was fit with a 2nd-order polynomial. Shown in the figure is a calibration of the pilot's lateral cyclic stick. These nonlinear calibrations were also used for other sensors, including measurements of other links in the flight control system, the swashplate servo positions, and fuel rates.

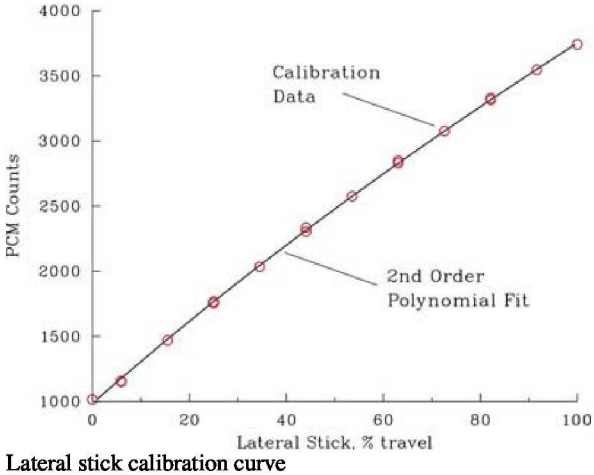

Lateral stick calibration curve

Not all failure modes for pressure transducers are known, but most fall into a few categories. Bag calibrations were repeated throughout the flight test program and detected major calibration errors and dead transducers. Noise on various transducers was not common. When it did occur, it tended to be intermittent. Frequency response was sometimes adequate for structural measurements, but not acoustic measurements. A few transducers showed unusual behaviors, not always repeatable and difficult of categorization. It is possible that there were unknown failures that have not yet been detected.

FAILURE MODES

Calibration scale or bias errors

Dead (continuous or intermittent)

Noisy (continuous or intermittent)

Inadequate frequency response

Uncategorized

Unknown

The pressure transducers were calibrated with the pressure blade hooked up to the aircraft ("bag cals") on a regular basis during the test program. The figure shows the resulting calibration slope for the first 90 of the 242 transducers. Most have a slope slightly below 0.02 volts/psia. But some transducers show an excessive positive or negative value (which is cut off on the plot), or a zero slope. The excessive values are sometimes related to bias problems rather than malfunctions, whereas the zero values generally indicated a failed transducer.

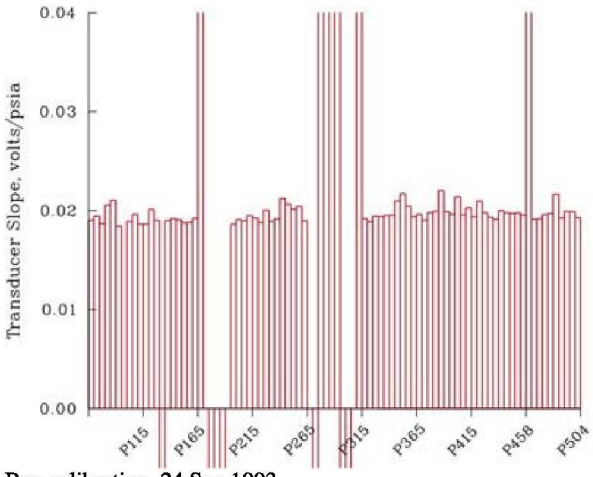

Bag calibration, 24 Sep 1993

The figure shows an offset plot of a fairly severe BVI event. Pressures are shown near the leading edge at 0.01c for the nine radial stations and for the special BVI transducers. As with the dynamic stall case, these data are a check on the location of the transducers and their frequency response. What is notable in this case are the two noise spikes at 0.775R. Although these kinds of spikes were frequent in previous tests where the unamplified analog signals were contaminated during slip ring transmission, they were infrequent in the UH-60A flight test. Small intermittent noise events, as shown here, can sometimes be corrected or just left alone. But in other situations the transducer signal is not used.

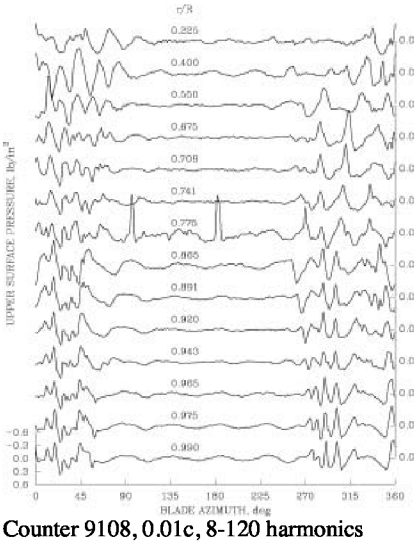

Counter 9108, 0.01c, 8-120 harmonics

Housekeeping points were flown at the start of each test flight and, if enough recording tape was left, at the end. These points were flown at an altitude of about a thousand feet and an airspeed of 80 kts, both inbound and outbound. Variation in atmospheric conditions and aircraft weight means that these were not exact repeat points, but they were good for identifying and tracking instrumentation problems. The figures show the measured pressures for all housekeeping points for two transducers at 0.965R as a cycle plot. The upper surface transducer (P801) as seen in Figure 1, is repeatable and worked for the entire test program.

The lower surface one (P851) as seen in Figure 2, worked through Flight 90 (Cycle 10) and then failed.

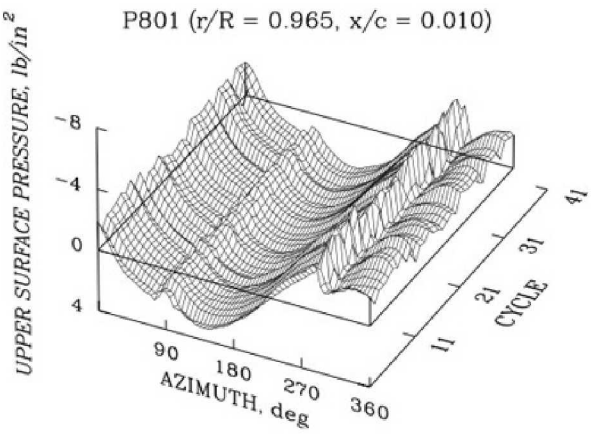

Housekeeping points were flown at the start of each test flight and, if enough recording tape was left, at the end. These points were flown at an altitude of about a thousand feet and an airspeed of 80 kts, both inbound and outbound. Variation in atmospheric conditions and aircraft weight means that these were not exact repeat points, but they were good for identifying and tracking instrumentation problems. The figures show the measured pressures for all housekeeping points for two transducers at 0.965R as a cycle plot. The upper surface transducer (P801) as seen in Figure 1, is repeatable and worked for the entire test program.

The lower surface one (P851) as seen in Figure 2, worked through Flight 90 (Cycle 10) and then failed.

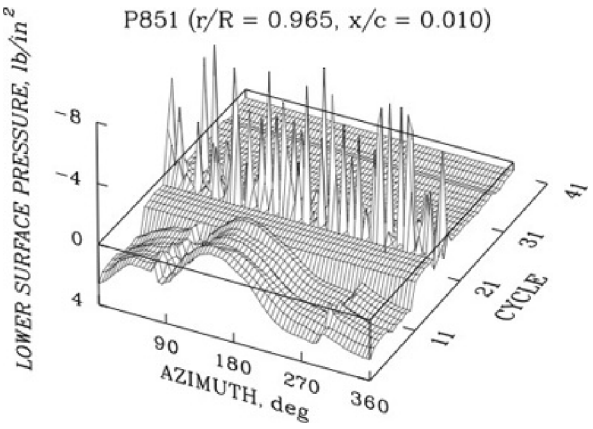

The pressure transducers were designed to have a frequency response well beyond the range of the instrumentation filters so that high frequency pressure measurements could be compared with external acoustic measurements. Once installed in the blade, the frequency response of each transducer was measured in the lab, and then checked again once the blade was on the aircraft. At the end of the program, explosive blanks ("yachting cannon") were fired near the blade and the overpressure ratios identify those transducers with poor frequency response. In the figure, these transducers are circled and they were excluded from the pressure integration. The gaps here indicate failed transducers.

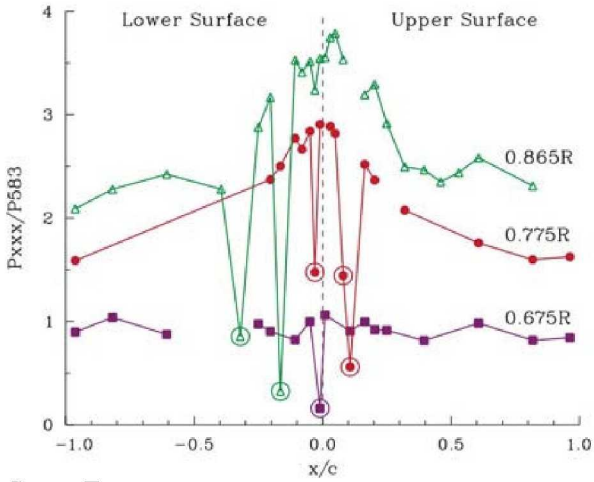

Cannon Test

Based on calibrations and various checks, each pressure transducer was considered either satisfactory or not satisfactory. A status or weighting matrix was established for each flight (and sometimes for individual counters). The figure here shows the status matrix for the upper surface pressure transducers. The lower surface portion of the matrix appears much the same. This matrix was used to document the adequacy of the pressure transducers, and was also used in the integration of the blade pressures for the section normal and chord forces and the pitching moments. All blade pressure measurements have been retained and can be re-integrated using a new status matrix, if needed.

Pressure Transducer Status
Flight 85
4/1/96
-1 = not installed
1 = satisfactory
0 = not satisfactory

x=	1	2	3	4	5	6	7	8	9	
	.225	.400	.550	.675	.775	.865	.920	.965	.990	
Px01	1	1	1	1	1	1	1	1	1	0.010
Px02	-1	-1	-1	-1	1	1	1	1	1	0.030
Px03	1	1	1	1	1	1	1	1	1	0.049
Px04	-1	-1	-1	-1	1	1	1	1	0	0.080
Px05	1	1	1	1	0	0	1	1	1	0.107
Px06	1	1	1	0	1	1	1	1	1	0.164
Px07	1	1	1	1	1	1	1	1	0	0.203
Px08	1	1	1	1	1	1	1	0	1	0.250
Px09	-1	-1	-1	-1	-1	1	1	1	1	0.320
Px10	0	1	1	1	1	1	1	1	1	0.395
Px11	-1	-1	-1	-1	-1	1	1	1	1	0.460
Px12	-1	-1	-1	-1	-1	1	0	1	0	0.530
Px13	1	1	0	1	1	1	0	1	1	0.607
Px14	1	1	1	1	1	1	1	1	1	0.818
Px15	1	1	0	1	1	1	1	1	1	0.963

The accurate integration of the blade pressures requires that the physical location of the transducers be known. Checks were continuous from manufacture through software development to transducer pressure checks. The final end-to-end check was to examine the measured pressures in the presence of a known physical phenomenon. The evolution of dynamic stall vortices was used for these final checks. The red lines shown here trace the passage along the blade chord of two separate dynamic stall vortices, proving that the transducers were correctly identified. (Note also the inadequate frequency response at 0.164c and 0.203c.)

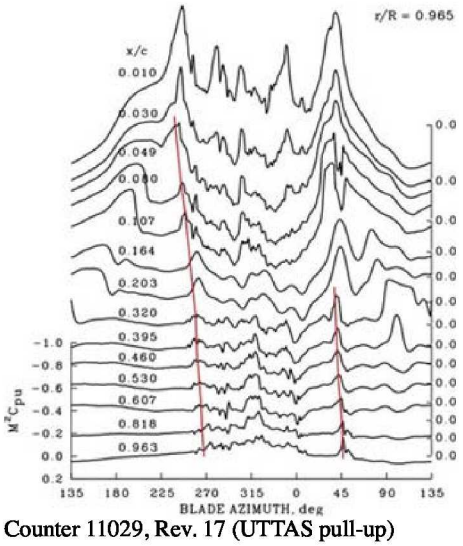

Counter 11029, Rev. 17 (UTTAS pull-up)

The pressure transducers were more closely distributed near the airfoil leading edge where the greatest pressure variation normally occurs in flight. The experimental objective was to obtain an accurate estimate of the normal force, the pitching moment about the quarter chord (0.25c), and the chord force (excluding viscous drag); all were obtained by integrating the measured pressures along the chord. If the transducers are spaced too far apart, then that will cause errors in the estimates. Or, if transducers fail during the flight program, then the accuracy is degraded. If too many transducers are lost, then the integration cannot be performed.

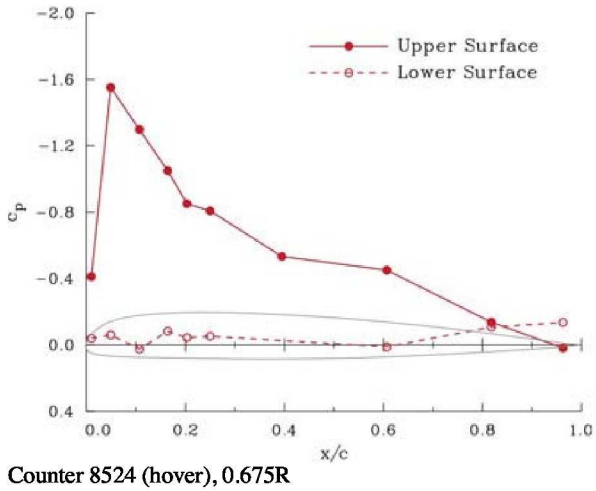

Counter 8524 (hover), 0.675R

The figure shows a calculation using the CFD code FLO-6 at M = 0.38 and α= 8° for the SC1094 R8 airfoil. The locations of the pressure transducers at the 0.675R radius overlie the calculation. At this radial station, the number of leading edge transducers are fewer than at more outboard stations, and it is apparent that the accuracy of the estimated forces and moments will be less. The FLO-6 calculation was used as a means of evaluating the accuracy of alternative integration approaches and to assess errors caused by failed transducers. Generally, accuracy of the algorithms used for forces were within 1–2% and for pitching moment within 2–3%.

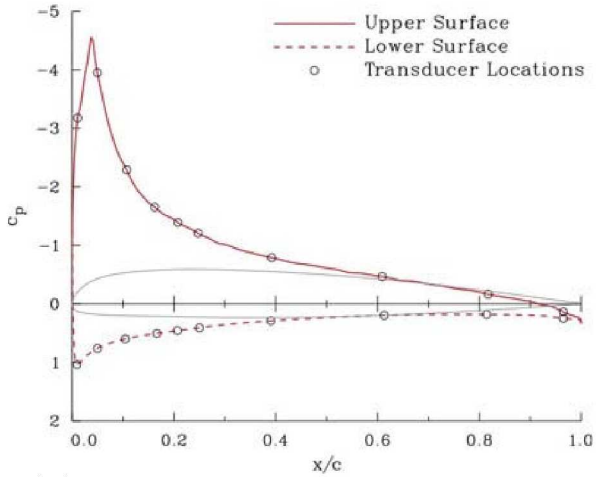

Calculation courtesy of Dr. W. J. McCroskey

Once the individual pressures are integrated at each of the nine radial stations, the section normal force is integrated along the blade to provide the blade thrust. This value should be close to the test aircraft weight, but it is not. The figure shows that the integrated section lift, which is referred to as "uncorrected" rotor thrust, ranges from 10 to 20% above the aircraft weight. Even after corrections for tail rotor, fuselage, and stabilator lift, the thrust is 16% too high. Near hover, part of this discrepancy is probably caused by download on the fuselage. But the remaining sources of errors are unknown, indicating that steady values of lift are biased.

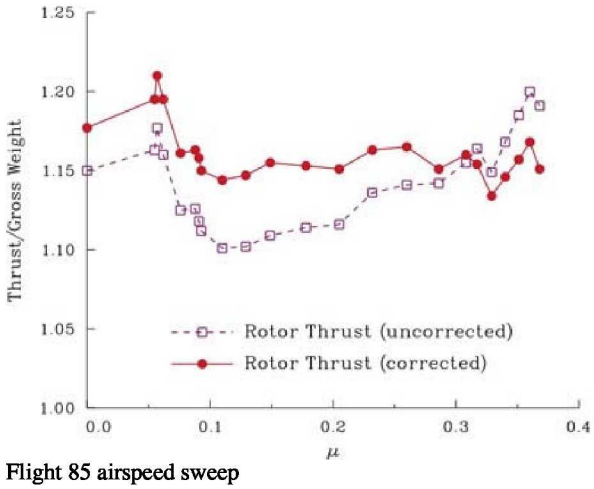

Flight 85 airspeed sweep

The measured flap bending moments at high speed on the blade are shown as a 3D Cartesian surface plot. Over the midspan portion of the blade, the moments are composed mostly of the 1st and 3rd harmonics. But at the root, many more higher harmonics are present. The moments shown in Figure 1 can also be calculated using the measured airloads, in this case using the RCAS analysis (Ho et al. 2007). Click on the arrow to see Figure 2 and the calculated loads will replace this text. Qualitatively, the agreement is quite good.

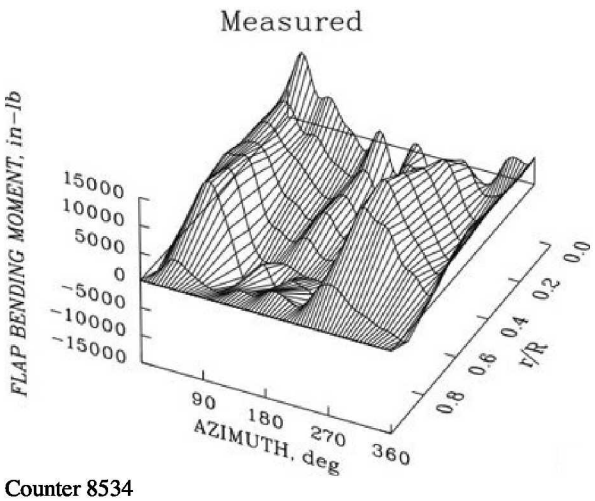

Counter 8534

The measured flap bending moments at high speed on the blade are shown as a 3D Cartesian surface plot. Over the midspan portion of the blade, the moments are composed mostly of the 1st and 3rd harmonics. But at the root, many more higher harmonics are present. The moments shown in Figure 1 can also be calculated using the measured airloads, in this case using the RCAS analysis (Ho et al. 2007). Click on the arrow to see Figure 2 and the calculated loads will replace this text. Qualitatively, the agreement is quite good.

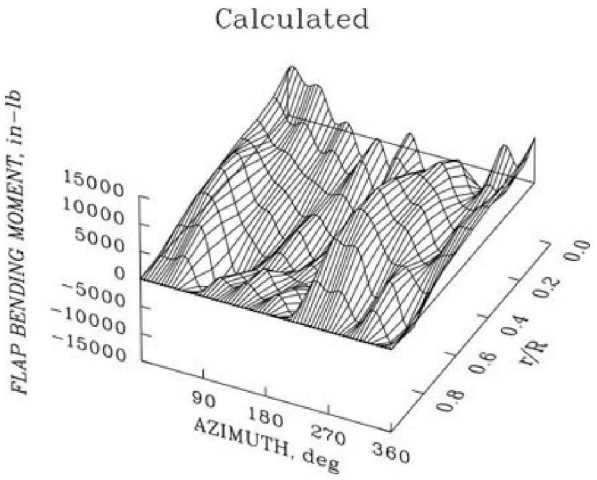

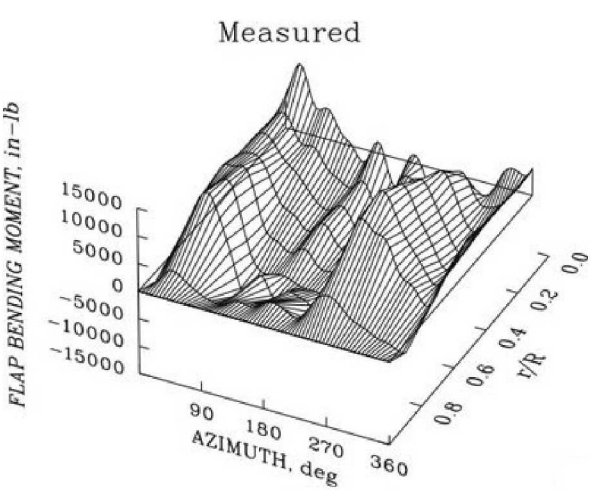

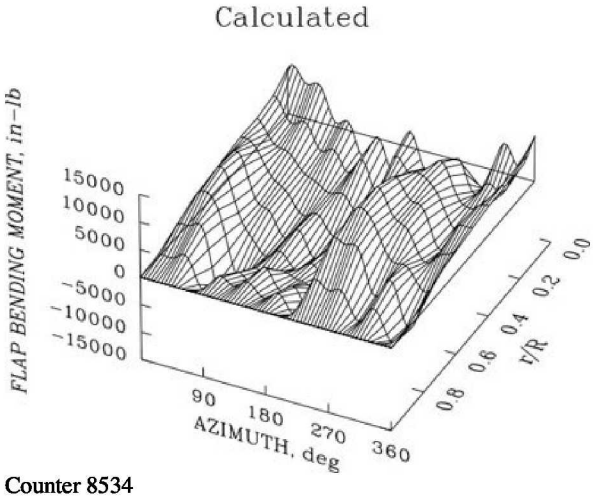

Counter 8534

The measured chord bending moments at high speed on the blade are shown in Figure 1 as a 3D Cartesian surface plot. These moments show higher harmonic loading than was seen for the flap bending. The loads at the root are strongly affected by nonlinear lag damper forces. The moments shown here can also be calculated using the measured airloads and damper forces using the RCAS analysis (Ho et al. 2007). Click on the arrow for Figure 2 and the calculated loads will replace this text. In this comparison, there is good agreement on the retreating side of the rotor, but less agreement on the advancing side.

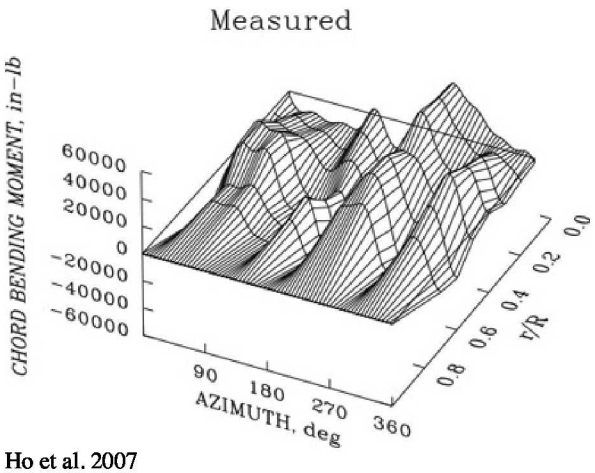

Ho et al. 2007

The measured chord bending moments at high speed on the blade are shown in Figure 1 as a 3D Cartesian surface plot. These moments show higher harmonic loading than was seen for the flap bending. The loads at the root are strongly affected by nonlinear lag damper forces. The moments shown here can also be calculated using the measured airloads and damper forces using the RCAS analysis (Ho et al. 2007). Click on the arrow for Figure 2 and the calculated loads will replace this text. In this comparison, there is good agreement on the retreating side of the rotor, but less agreement on the advancing side.

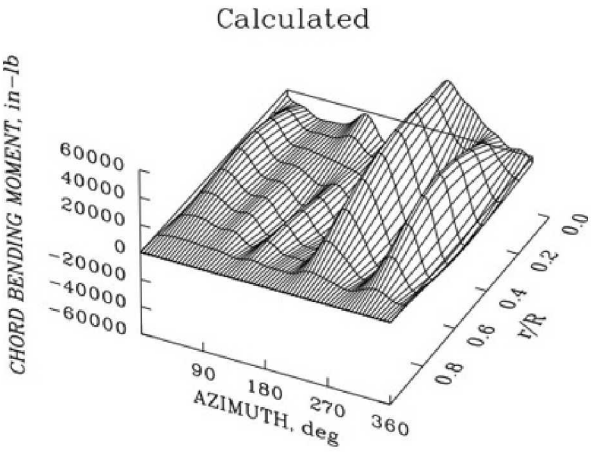

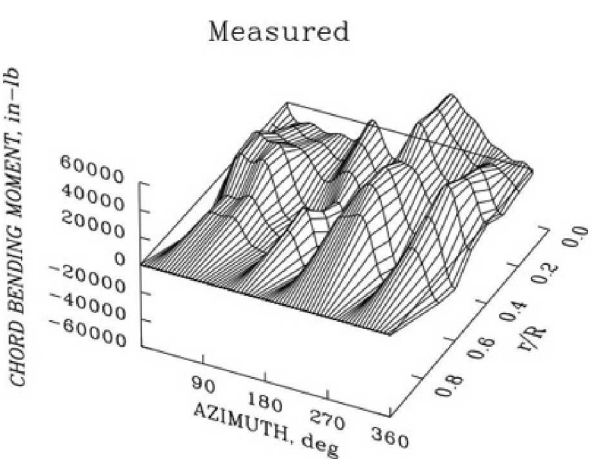
Measured
CHORD BENDING MOMENT, in-lb
60000
40000
20000
0
-20000
-40000
-60000
90
180
270
360
AZIMUTH, deg
0.8
0.6
0.4
0.2
0.0
r/R

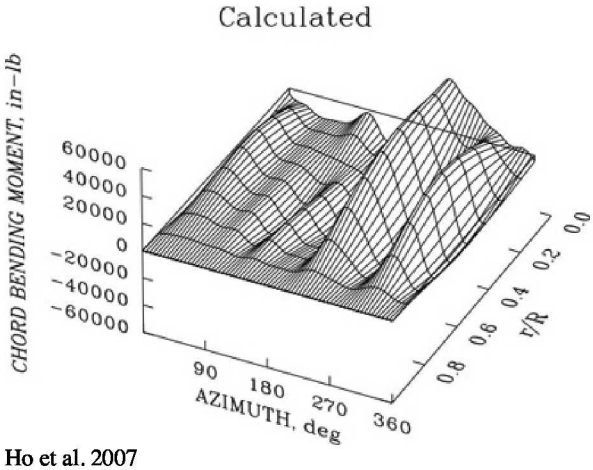
Calculated
CHORD BENDING MOMENT, in-lb
60000
40000
20000
0
-20000
-40000
-60000
90
180
270
360
AZIMUTH, deg
0.8
0.6
0.4
0.2
0.0
r/R

Ho et al. 2007

The measured torsion moments at high speed on the blade are shown on a 3D Cartesian surface plot in Figure 1. These moments increase monotonically from the tip of the blade to the root. The moments shown here can also be calculated using the measured airloads using the RCAS analysis (Ho et al. 2007). Click on the arrow for Figure 2 and the calculated loads will replace this text. There is generally good agreement in the loading on the advancing side of the rotor, but on the retreating side the calculation using measured airloads does not show the higher frequency loading.

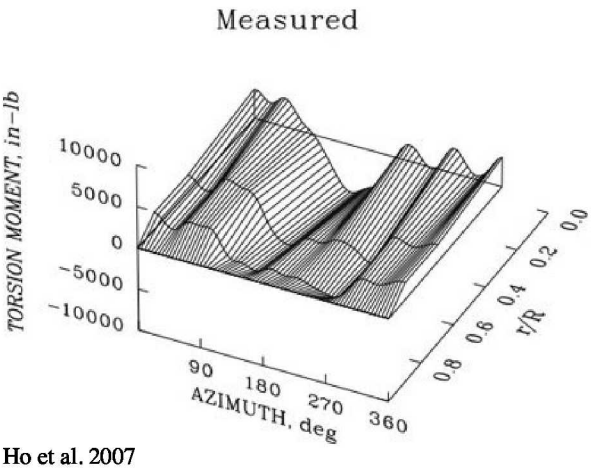

Ho et al. 2007

The measured torsion moments at high speed on the blade are shown on a 3D Cartesian surface plot in Figure 1. These moments increase monotonically from the tip of the blade to the root. The moments shown here can also be calculated using the measured airloads using the RCAS analysis (Ho et al. 2007). Click on the arrow for Figure 2 and the calculated loads will replace this text. There is generally good agreement in the loading on the advancing side of the rotor, but on the retreating side the calculation using measured airloads does not show the higher frequency loading.

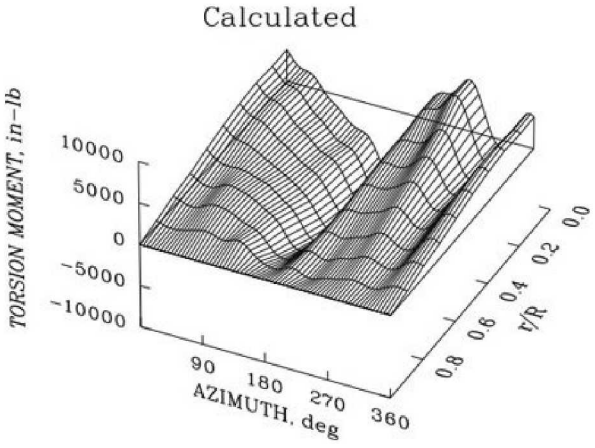

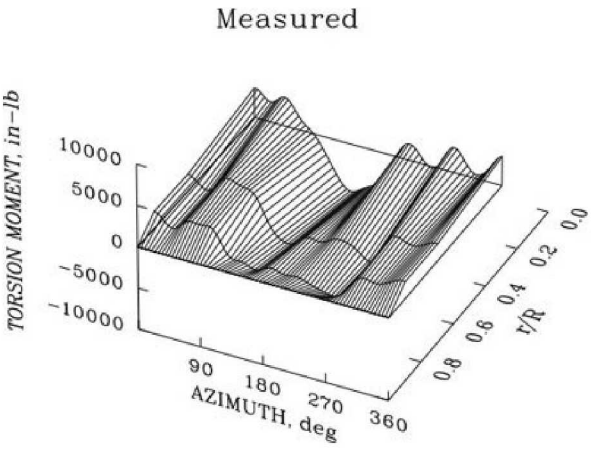
Measured
TORSION MOMENT, in-lb
10000
5000
0
-5000
-10000
90
180
270
360
AZIMUTH, deg
0.8
0.6
0.4
0.2
0.0
r/R

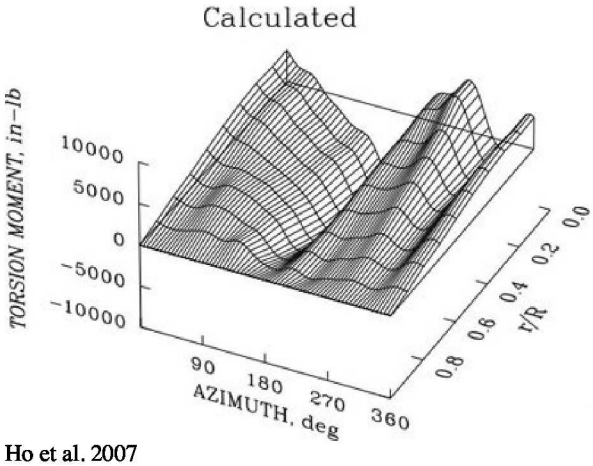
Calculated
TORSION MOMENT, in-lb
10000
5000
0
-5000
-10000
90
180
270
360
AZIMUTH, deg
0.8
0.6
0.4
0.2
0.0
r/R

Ho et al. 2007

With the aircraft on the ground and the collective at flat pitch, the pilot was asked to make one-inch stick inputs, first in longitudinal stick and then in lateral stick. These inputs tilt the rotor disk (through blade flapping) and this also causes shaft bending moments. Figure 1 compares moments calculated from blade flapping with those measured on the shaft-these independent measurements agree. Click on the arrow for Figure 2 and stick motions will replace the shaft moment. Note that the static disk response, as indicated by the shaft bending moments, is similar to the phase of the control inputs.

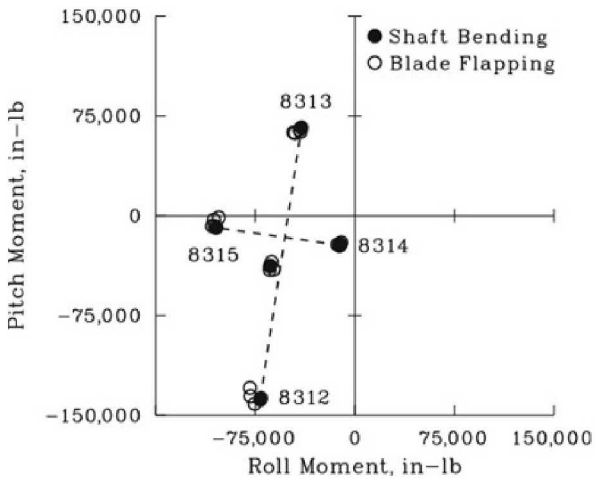

With the aircraft on the ground and the collective at flat pitch, the pilot was asked to make one-inch stick inputs, first in longitudinal stick and then in lateral stick. These inputs tilt the rotor disk (through blade flapping) and this also causes shaft bending moments. Figure 1 compares moments calculated from blade flapping with those measured on the shaft-these independent measurements agree. Click on the arrow for Figure 2 and stick motions will replace the shaft moment. Note that the static disk response, as indicated by the shaft bending moments, is similar to the phase of the control inputs.

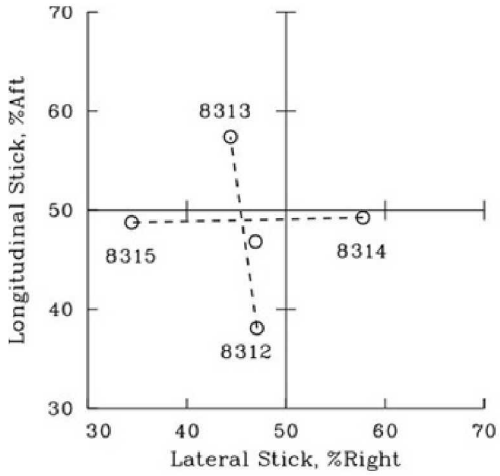

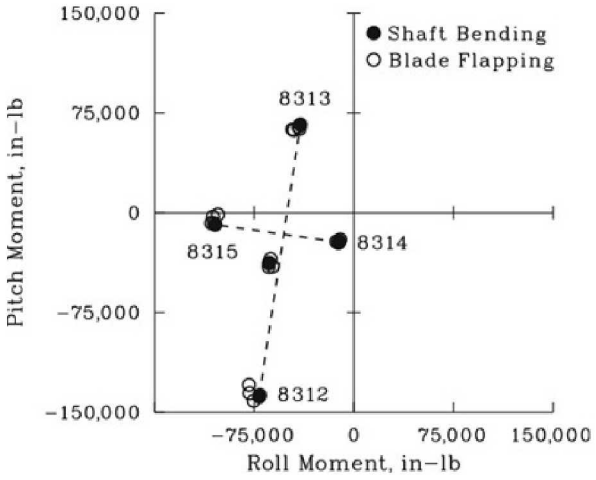
150,000
75,000
0
−75,000
−150,000
Pitch Moment, in−lb
−75,000
0
75,000
150,000
Roll Moment, in−lb
Shaft Bending
Blade Flapping
8313
8314
8315
8312

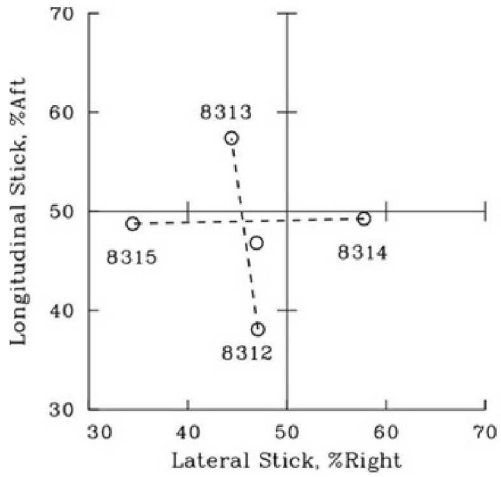
70
60
50
40
30
Longitudinal Stick, %Aft
30
40
50
60
70
Lateral Stick, %Right
8313
8315
8314
8312

This chapter starts out with an overview of the aircraft instrumentation. It then summarizes test results in the areas of hover and forward flight performance, airloads and structural loads, low-speed vortex loading and vibration, high-speed transonic loading and power limits, maneuver loads including dynamic stall, and concludes with acoustic test flights.

An examination of hover performance illustrates the difficulties of obtaining performance data in unsteady conditions.

Forward flight performance provides an overview of testing at multiple weight conditions and looks at power, airloads, and structural loads. Greater detail of the blade airloads in forward flight are provided for low-speed and high-speed cases.

Maneuver loading examines severe flight conditions, where dynamic stall causes excessive control system loading. The behavior of this dynamic stall vortex loading is examined in detail. High loads in diving flight are also shown, where the loading is caused by shocks on the blades.

The chapter finishes with an examination of flight cases important for radiated noise.

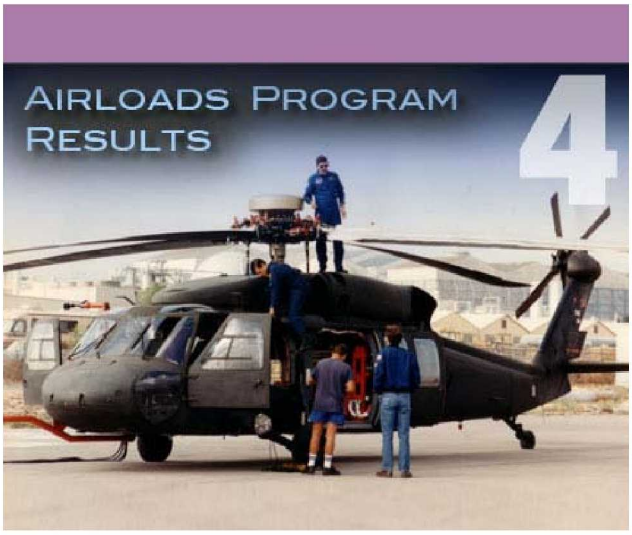

The UH-60A Airloads Aircraft was instrumented with about 480 sensors, most of them in the rotating system. These sensors (the number shown in parentheses) are categorized as:

- blade pressures (242)
- blade temperatures (50)
- blade strain and acceleration (56)
- blade root motion (15)
- fuselage and hub accelerometers (40)
- aircraft state (51)
- health and miscellaneous (26)

The pressure blade (#1) had all pressure and temperature sensors, plus 5 measurements of strain. The strain and motion blade (#3) had 21 strain gauges and 12 accelerometers.

Most of the 242 absolute pressure transducers were chordwise arrays at nine radial stations. Slightly fewer transducers were on the lower surface. These chordwise arrays were concentrated toward the blade tip, where the airloads are greater. But note that there were also a few transducers located at intermediate radial stations near the leading edge of the blade. These were installed to better study blade vortex interactions (BVIs). The pressure transducers were not temperature compensated, but the local temperature was measured at 50 locations along the blade. As of yet, no temperature corrections have been applied to the pressure measurements.

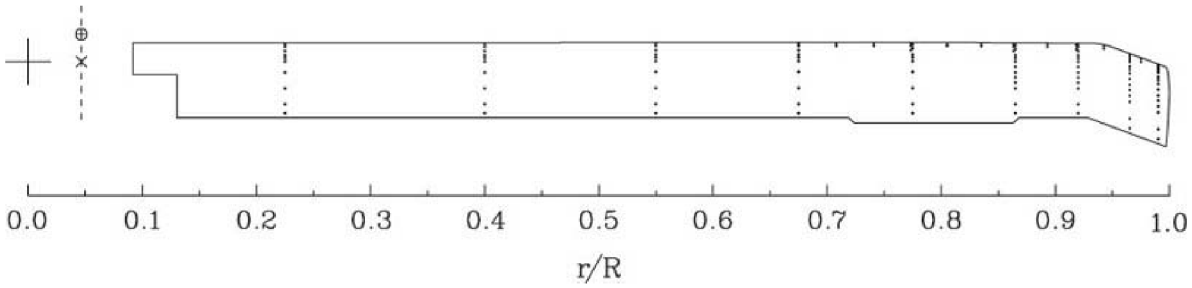

The strain gauge and motion blade had strain measurements at nine radial stations, although not every station had all three measurements. The pressure blade had limited bending measurements as well. Accelerometers were built into the blade at four stations. At each station two accelerometers measured flapping accelerations (each offset from the pitch axis for torsion response) and one measured chord acceleration.

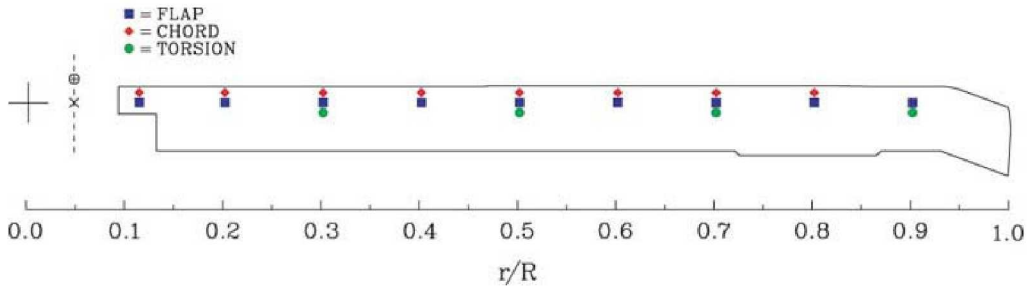

Here, the hover performance measured in the Airloads Program is compared with data obtained by the US Army Edwards Flight Activity (AEFA) (Marshall et al. 1985, Nagata et al. 1989). For the AEFA data, a tether connected the aircraft to the ground and flights were in near-zero winds. Hover points during the Airloads Program were flown in free air regardless of winds, resulting in considerable data scatter. AEFA obtained hover data at three altitudes, providing an extensive range in the C_W/σ, but the Airloads Program data were obtained over a smaller range. Nonetheless, the Airloads Program pressure data provide unique insight into hovering performance.

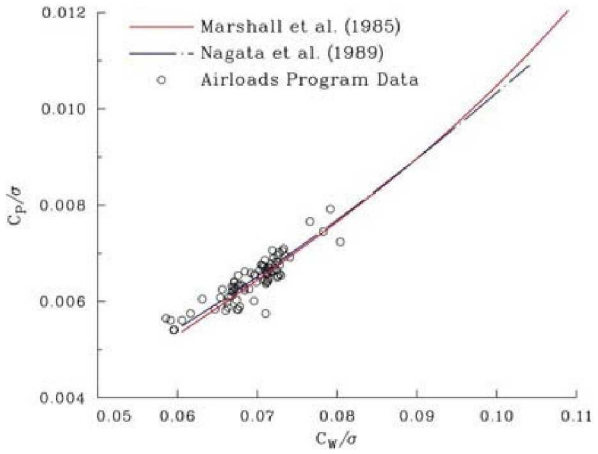

The most accurate hover case was obtained during ground-acoustic testing, performed in cooperation with NASA Langley Research Center. For these tests, aircraft motions were tracked with a laser. Wind speeds were measured on the ground, 30 meters above the ground and at the hover altitude of 250 feet. The data in Figure 1 were taken 5 days apart. For Flight 94, winds were excessive, particularly at the test altitude, whereas for Flight 96, they were less than 3 kts at all altitudes. Click the arrow for Figure 2 to see the computed advance ratios for Flights 96 and 98. (The winds aloft for Flight 98 were about 8 kts.)

For Counter 9605, the x- and y-components of the aircraft velocity with respect to the air mass (μ_x and μ_y) are almost exactly zero.

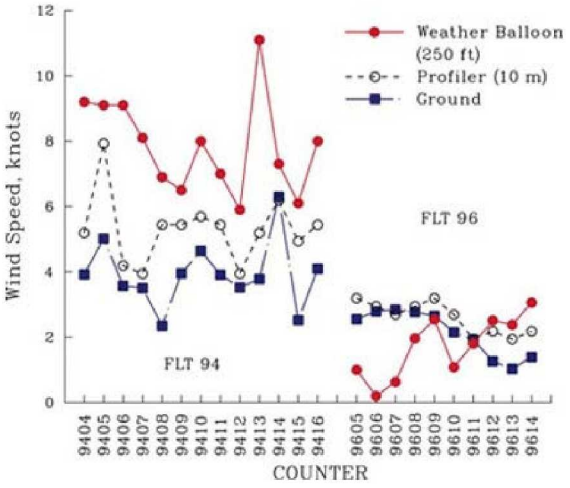

The most accurate hover case was obtained during ground-acoustic testing, performed in cooperation with NASA Langley Research Center. For these tests, aircraft motions were tracked with a laser. Wind speeds were measured on the ground, 30 meters above the ground and at the hover altitude of 250 feet. The data in Figure 1 were taken 5 days apart. For Flight 94, winds were excessive, particularly at the test altitude, whereas for Flight 96, they were less than 3 kts at all altitudes. Click the arrow for Figure 2 to see the computed advance ratios for Flights 96 and 98. (The winds aloft for Flight 98 were about 8 kts.)

For Counter 9605, the x- and y-components of the aircraft velocity with respect to the air mass (μ_x and μ_y) are almost exactly zero.

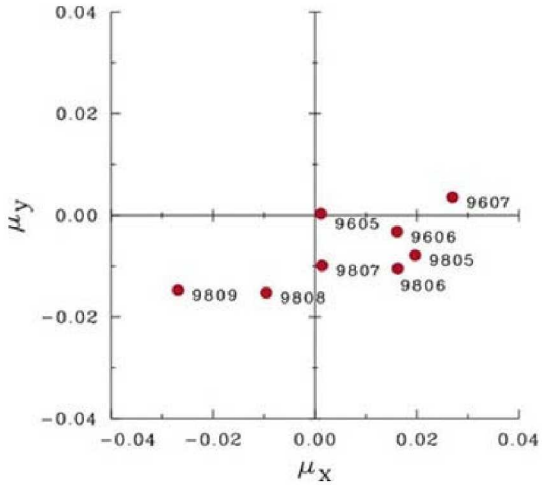

An offset plot of the measured normal force for the hover point, Counter 9605, is shown in the figure. Although this is considered a steady condition, the normal forces outboard of about 0.775R show significant oscillations. These oscillations change from revolution to revolution as can be seen by clicking the button, which provides an animation of 20 revolutions (about 5 sec.). The primary cause of these oscillations is the intersection of the main rotor blade with tail rotor vortices in the fourth quadrant of the rotor disk, as can be seen by referring to a layout of the rotor on the next tab.

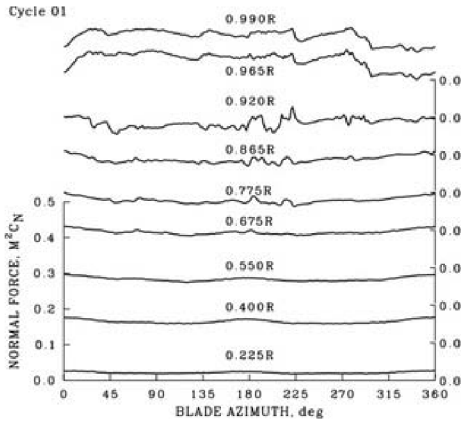

An offset plot of the measured normal force for the hover point, Counter 9605, is shown in the figure. Although this is considered a steady condition, the normal forces outboard of about 0.775R show significant oscillations. These oscillations change from revolution to revolution as can be seen by clicking the button, which provides an animation of 20 revolutions (about 5 sec.). The primary cause of these oscillations is the intersection of the main rotor blade with tail rotor vortices in the fourth quadrant of the rotor disk, as can be seen by referring to a layout of the rotor on the next tab.

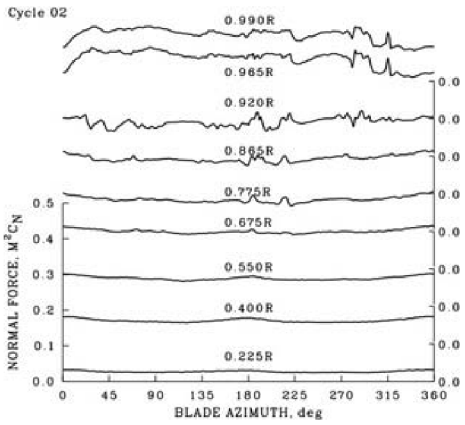

An offset plot of the measured normal force for the hover point, Counter 9605, is shown in the figure. Although this is considered a steady condition, the normal forces outboard of about 0.775R show significant oscillations. These oscillations change from revolution to revolution as can be seen by clicking the button, which provides an animation of 20 revolutions (about 5 sec.). The primary cause of these oscillations is the intersection of the main rotor blade with tail rotor vortices in the fourth quadrant of the rotor disk, as can be seen by referring to a layout of the rotor on the next tab.

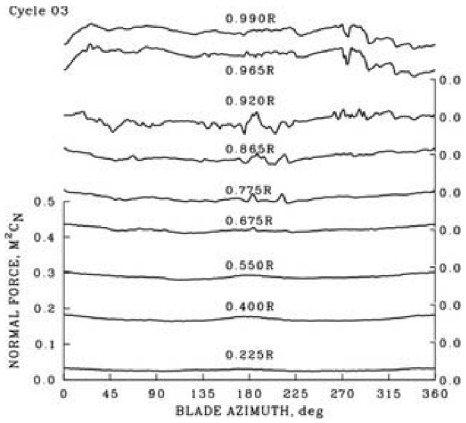

An offset plot of the measured normal force for the hover point, Counter 9605, is shown in the figure. Although this is considered a steady condition, the normal forces outboard of about 0.775R show significant oscillations. These oscillations change from revolution to revolution as can be seen by clicking the button, which provides an animation of 20 revolutions (about 5 sec.). The primary cause of these oscillations is the intersection of the main rotor blade with tail rotor vortices in the fourth quadrant of the rotor disk, as can be seen by referring to a layout of the rotor on the next tab.

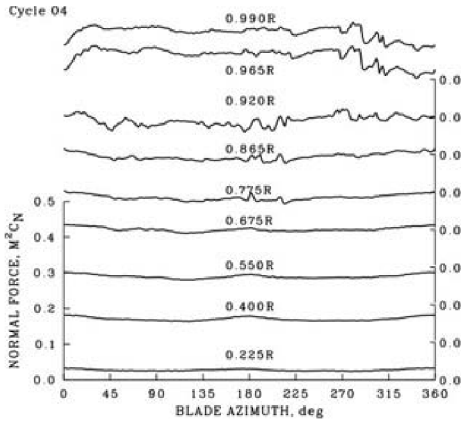

An offset plot of the measured normal force for the hover point, Counter 9605, is shown in the figure. Although this is considered a steady condition, the normal forces outboard of about 0.775R show significant oscillations. These oscillations change from revolution to revolution as can be seen by clicking the button, which provides an animation of 20 revolutions (about 5 sec.). The primary cause of these oscillations is the intersection of the main rotor blade with tail rotor vortices in the fourth quadrant of the rotor disk, as can be seen by referring to a layout of the rotor on the next tab.

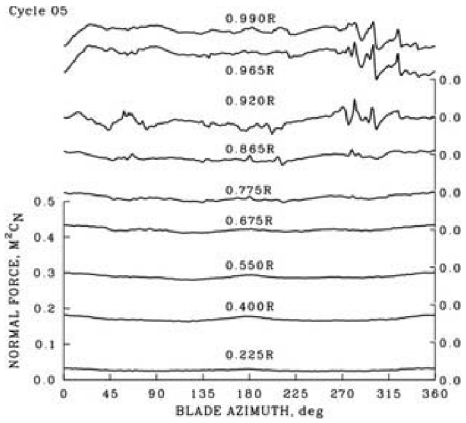

An offset plot of the measured normal force for the hover point, Counter 9605, is shown in the figure. Although this is considered a steady condition, the normal forces outboard of about 0.775R show significant oscillations. These oscillations change from revolution to revolution as can be seen by clicking the button, which provides an animation of 20 revolutions (about 5 sec.). The primary cause of these oscillations is the intersection of the main rotor blade with tail rotor vortices in the fourth quadrant of the rotor disk, as can be seen by referring to a layout of the rotor on the next tab.

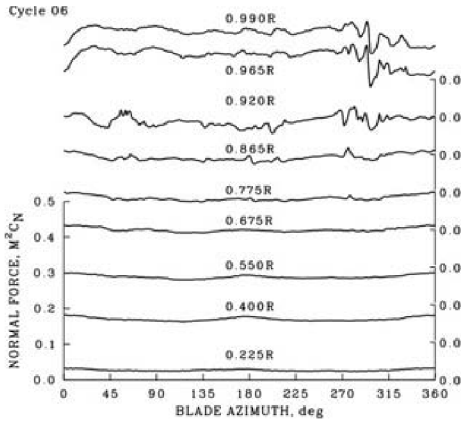

An offset plot of the measured normal force for the hover point, Counter 9605, is shown in the figure. Although this is considered a steady condition, the normal forces outboard of about 0.775R show significant oscillations. These oscillations change from revolution to revolution as can be seen by clicking the button, which provides an animation of 20 revolutions (about 5 sec.). The primary cause of these oscillations is the intersection of the main rotor blade with tail rotor vortices in the fourth quadrant of the rotor disk, as can be seen by referring to a layout of the rotor on the next tab.

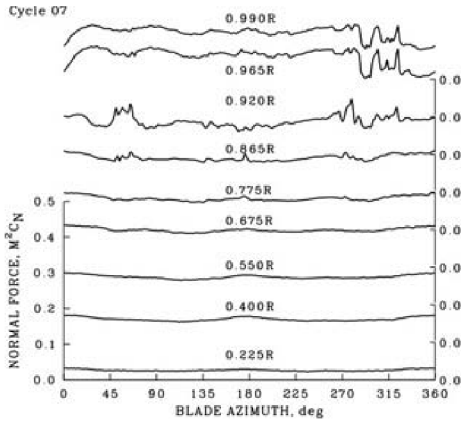

An offset plot of the measured normal force for the hover point, Counter 9605, is shown in the figure. Although this is considered a steady condition, the normal forces outboard of about 0.775R show significant oscillations. These oscillations change from revolution to revolution as can be seen by clicking the button, which provides an animation of 20 revolutions (about 5 sec.). The primary cause of these oscillations is the intersection of the main rotor blade with tail rotor vortices in the fourth quadrant of the rotor disk, as can be seen by referring to a layout of the rotor on the next tab.

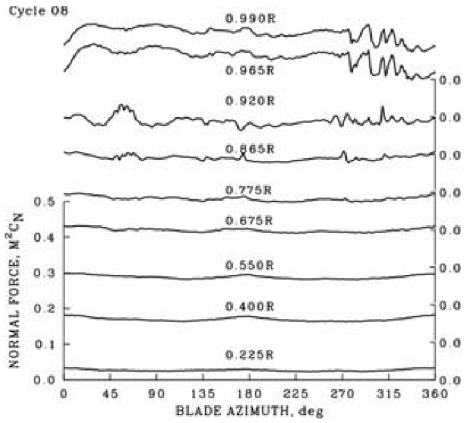

An offset plot of the measured normal force for the hover point, Counter 9605, is shown in the figure. Although this is considered a steady condition, the normal forces outboard of about 0.775R show significant oscillations. These oscillations change from revolution to revolution as can be seen by clicking the button, which provides an animation of 20 revolutions (about 5 sec.). The primary cause of these oscillations is the intersection of the main rotor blade with tail rotor vortices in the fourth quadrant of the rotor disk, as can be seen by referring to a layout of the rotor on the next tab.

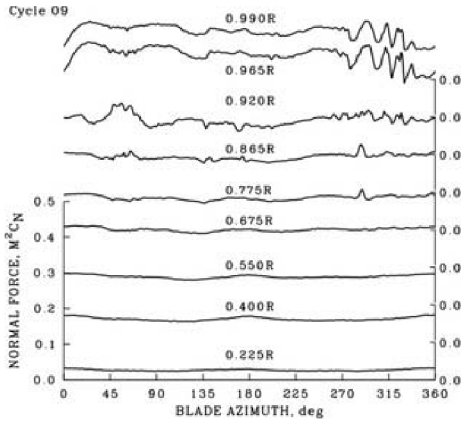

An offset plot of the measured normal force for the hover point, Counter 9605, is shown in the figure. Although this is considered a steady condition, the normal forces outboard of about 0.775R show significant oscillations. These oscillations change from revolution to revolution as can be seen by clicking the button, which provides an animation of 20 revolutions (about 5 sec.). The primary cause of these oscillations is the intersection of the main rotor blade with tail rotor vortices in the fourth quadrant of the rotor disk, as can be seen by referring to a layout of the rotor on the next tab.

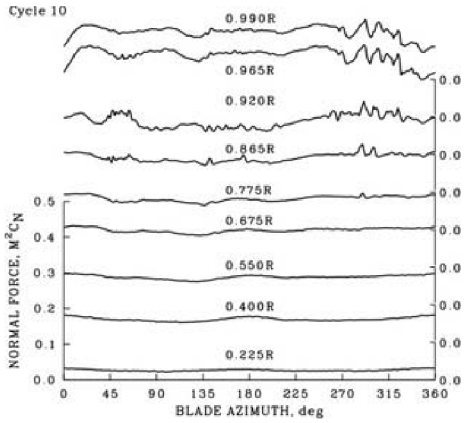

An offset plot of the measured normal force for the hover point, Counter 9605, is shown in the figure. Although this is considered a steady condition, the normal forces outboard of about 0.775R show significant oscillations. These oscillations change from revolution to revolution as can be seen by clicking the button, which provides an animation of 20 revolutions (about 5 sec.). The primary cause of these oscillations is the intersection of the main rotor blade with tail rotor vortices in the fourth quadrant of the rotor disk, as can be seen by referring to a layout of the rotor on the next tab.

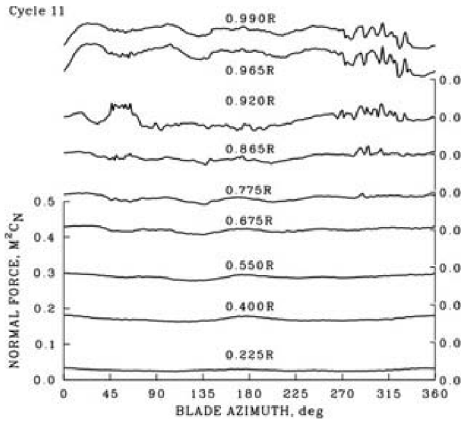

An offset plot of the measured normal force for the hover point, Counter 9605, is shown in the figure. Although this is considered a steady condition, the normal forces outboard of about 0.775R show significant oscillations. These oscillations change from revolution to revolution as can be seen by clicking the button, which provides an animation of 20 revolutions (about 5 sec.). The primary cause of these oscillations is the intersection of the main rotor blade with tail rotor vortices in the fourth quadrant of the rotor disk, as can be seen by referring to a layout of the rotor on the next tab.

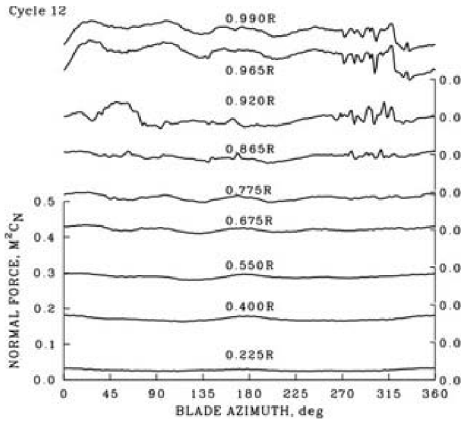

An offset plot of the measured normal force for the hover point, Counter 9605, is shown in the figure. Although this is considered a steady condition, the normal forces outboard of about 0.775R show significant oscillations. These oscillations change from revolution to revolution as can be seen by clicking the button, which provides an animation of 20 revolutions (about 5 sec.). The primary cause of these oscillations is the intersection of the main rotor blade with tail rotor vortices in the fourth quadrant of the rotor disk, as can be seen by referring to a layout of the rotor on the next tab.

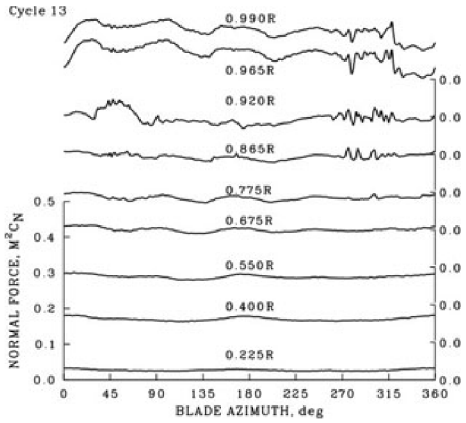

An offset plot of the measured normal force for the hover point, Counter 9605, is shown in the figure. Although this is considered a steady condition, the normal forces outboard of about 0.775R show significant oscillations. These oscillations change from revolution to revolution as can be seen by clicking the button, which provides an animation of 20 revolutions (about 5 sec.). The primary cause of these oscillations is the intersection of the main rotor blade with tail rotor vortices in the fourth quadrant of the rotor disk, as can be seen by referring to a layout of the rotor on the next tab.

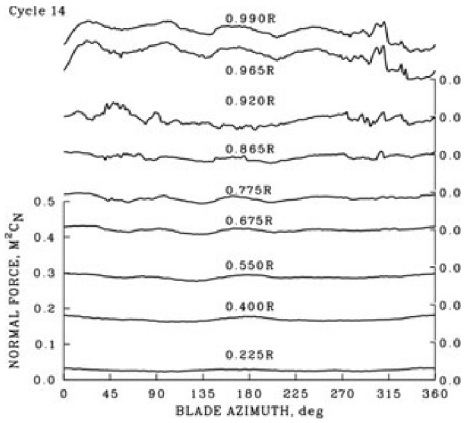

An offset plot of the measured normal force for the hover point, Counter 9605, is shown in the figure. Although this is considered a steady condition, the normal forces outboard of about 0.775R show significant oscillations. These oscillations change from revolution to revolution as can be seen by clicking the button, which provides an animation of 20 revolutions (about 5 sec.). The primary cause of these oscillations is the intersection of the main rotor blade with tail rotor vortices in the fourth quadrant of the rotor disk, as can be seen by referring to a layout of the rotor on the next tab.

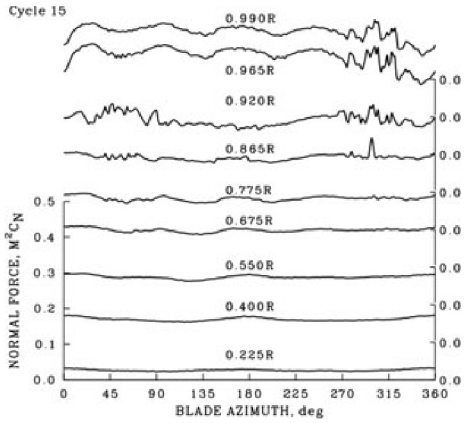

An offset plot of the measured normal force for the hover point, Counter 9605, is shown in the figure. Although this is considered a steady condition, the normal forces outboard of about 0.775R show significant oscillations. These oscillations change from revolution to revolution as can be seen by clicking the button, which provides an animation of 20 revolutions (about 5 sec.). The primary cause of these oscillations is the intersection of the main rotor blade with tail rotor vortices in the fourth quadrant of the rotor disk, as can be seen by referring to a layout of the rotor on the next tab.

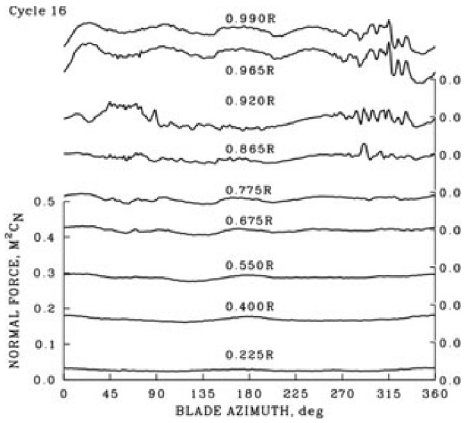

An offset plot of the measured normal force for the hover point, Counter 9605, is shown in the figure. Although this is considered a steady condition, the normal forces outboard of about 0.775R show significant oscillations. These oscillations change from revolution to revolution as can be seen by clicking the button, which provides an animation of 20 revolutions (about 5 sec.). The primary cause of these oscillations is the intersection of the main rotor blade with tail rotor vortices in the fourth quadrant of the rotor disk, as can be seen by referring to a layout of the rotor on the next tab.

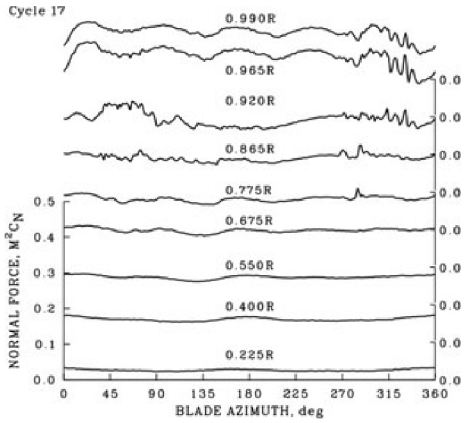

An offset plot of the measured normal force for the hover point, Counter 9605, is shown in the figure. Although this is considered a steady condition, the normal forces outboard of about 0.775R show significant oscillations. These oscillations change from revolution to revolution as can be seen by clicking the button, which provides an animation of 20 revolutions (about 5 sec.). The primary cause of these oscillations is the intersection of the main rotor blade with tail rotor vortices in the fourth quadrant of the rotor disk, as can be seen by referring to a layout of the rotor on the next tab.

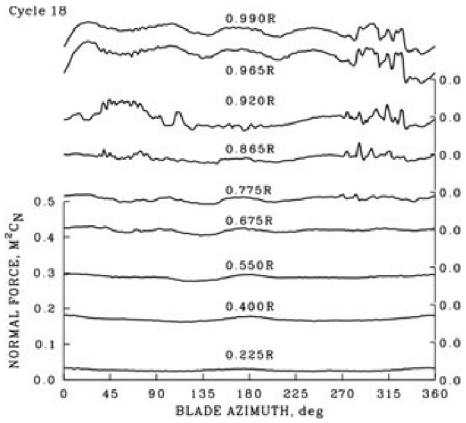

An offset plot of the measured normal force for the hover point, Counter 9605, is shown in the figure. Although this is considered a steady condition, the normal forces outboard of about 0.775R show significant oscillations. These oscillations change from revolution to revolution as can be seen by clicking the button, which provides an animation of 20 revolutions (about 5 sec.). The primary cause of these oscillations is the intersection of the main rotor blade with tail rotor vortices in the fourth quadrant of the rotor disk, as can be seen by referring to a layout of the rotor on the next tab.

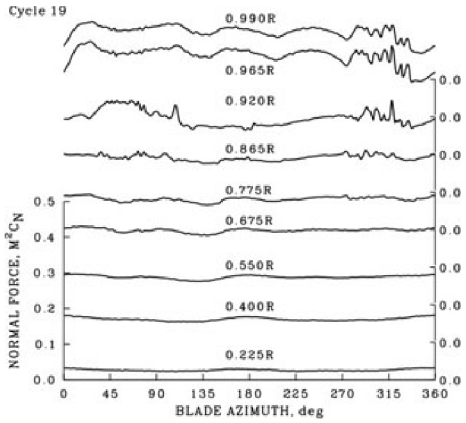

An offset plot of the measured normal force for the hover point, Counter 9605, is shown in the figure. Although this is considered a steady condition, the normal forces outboard of about 0.775R show significant oscillations. These oscillations change from revolution to revolution as can be seen by clicking the button, which provides an animation of 20 revolutions (about 5 sec.). The primary cause of these oscillations is the intersection of the main rotor blade with tail rotor vortices in the fourth quadrant of the rotor disk, as can be seen by referring to a layout of the rotor on the next tab.

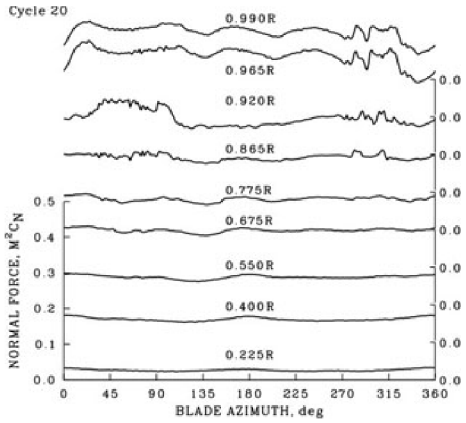

The layout in the figure shows a plan view of the UH-60A. The rotor rotates in a counterclockwise direction and the tail rotor, which counteracts the main rotor torque, must thrust towards the top of the figure, which means the wake moves toward the bottom. Just as the main rotor wake contains concentrated tip vortices, so does the tail rotor wake. Their effect is what is seen in the time histories of the normal force shown in the previous tab.

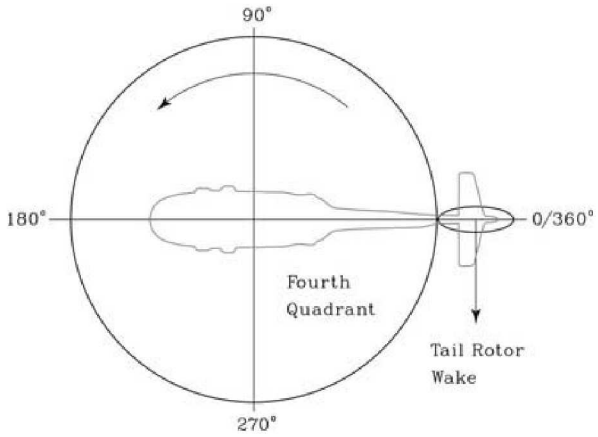

During ground-acoustic testing in hover (in cooperation with NASA Langley Research Center), the winds were higher than desired on Flight 94. The aircraft heading was changed in 15° increments for these tests, and the angle of the relative wind changed by these same increments. These data, then, provide a look at the effects of winds in hover on tail rotor and main rotor interference, which proves the old adage that it is an ill wind that blows no one some good. Two examples are shown in the following tabs. In this figure only 3 of the 15 counters are labeled.

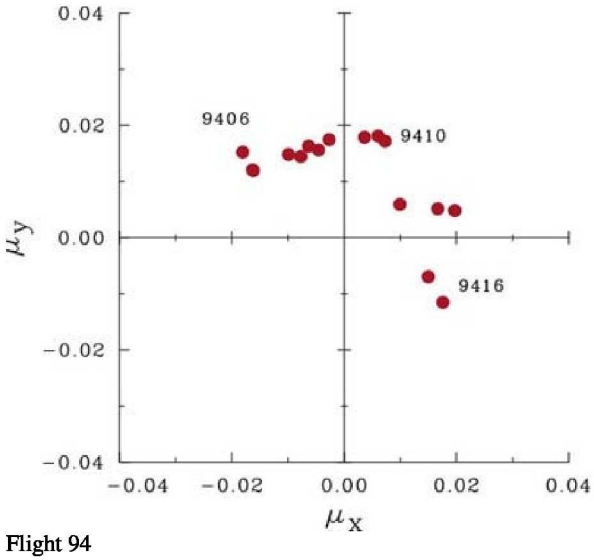

Flight 94

In the figure, an offset plot of the measured normal forces is shown for a case where the relative wind was coming from the right rear quadrant of the aircraft. The expectation was that this wind should blow the tail rotor wake into the main rotor in the fourth quadrant, and that is what is seen in the figure. Multiple intersections of tail rotor vortices are seen on the blade outboard of 0.775R.

The effect of these strong tail rotor vortices is to cause noise in the hover conditions, but they have little effect on the integrated blade loads and are not noticed as an increase in vibration.

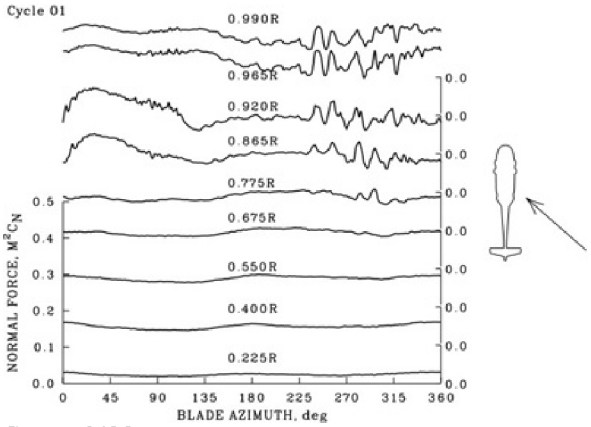

Counter 9406

In the figure, an offset plot of the measured normal forces is shown for a case where the relative wind was coming from the left front quadrant of the aircraft. The expectation is that this wind should blow the tail rotor wake away from the main rotor in the fourth quadrant, and that is what is seen in the figure. Almost no effect of the tail rotor wake is seen on the main rotor loads. The main rotor may have a much greater effect on tail rotor loads and performance. In the 1960s, the rotation direction of some tail rotors caused them to loose lift when immersed in the main rotor wake under adverse wind conditions. This lesson has now been learned.

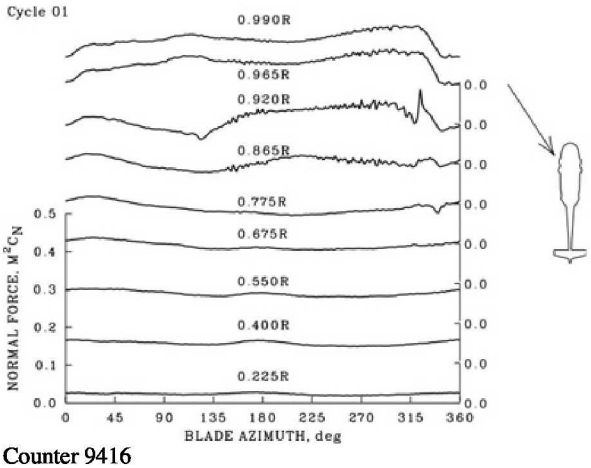

Counter 9416

The US Army requires that new helicopters demonstrate a 500 ft/min vertical rate of climb at the hover design point to provide excess power for maneuver. Both the measurement and calculation of this vertical climb are difficult to obtain accurately (Harris 1986). Three vertical climbs were flown during ground-acoustic testing for different cases of excess power, as shown in Figure 1. The lowest climb rate, Counter 9418, at 600 ft/min, is near the Army requirement.

Figure 2 will show the excess power for these cases. The power ratio for the 600 ft/min case was 1.17, once the power transients settled down.

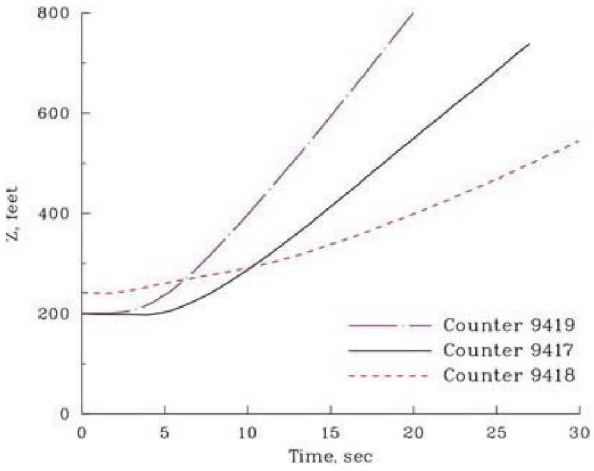

The US Army requires that new helicopters demonstrate a 500 ft/min vertical rate of climb at the hover design point to provide excess power for maneuver. Both the measurement and calculation of this vertical climb are difficult to obtain accurately (Harris 1986). Three vertical climbs were flown during ground-acoustic testing for different cases of excess power, as shown in Figure 1. The lowest climb rate, Counter 9418, at 600 ft/min, is near the Army requirement.

Figure 2 will show the excess power for these cases. The power ratio for the 600 ft/min case was 1.17, once the power transients settled down.

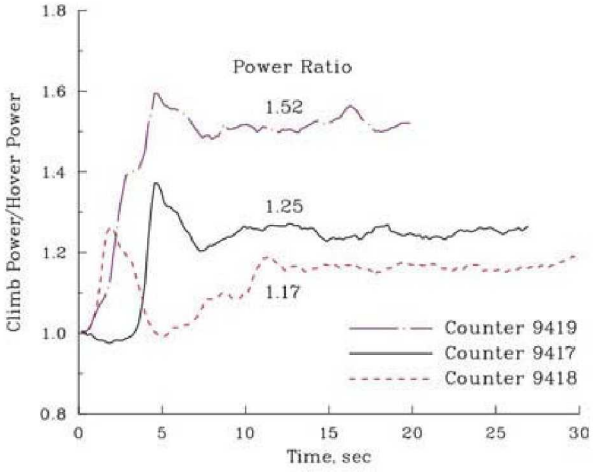

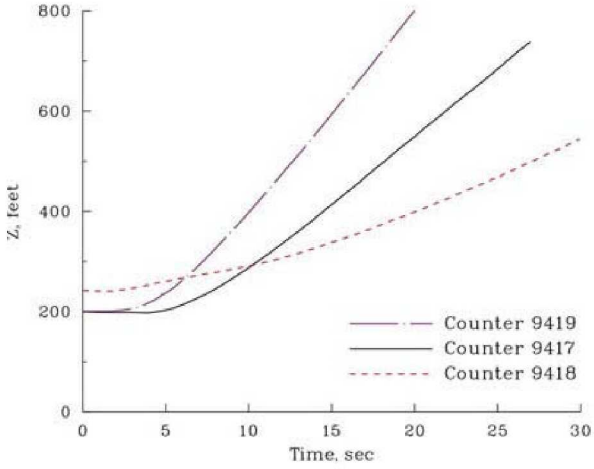
800
600
400
200
0
Z, feet
0
5
10
15
20
25
30
Time, sec
Counter 9419
Counter 9417
Counter 9418

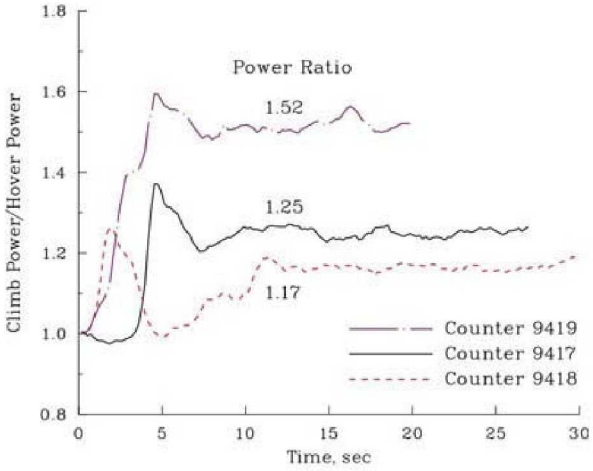
1.8
1.6
1.4
1.2
1.0
0.8
Climb Power/Hover Power
Power Ratio
1.52
1.25
1.17
0
5
10
15
20
25
30
Time, sec
Counter 9419
Counter 9417
Counter 9418

Level flight test data were obtained for six weight coefficients, as shown here. The series of level flight data, called an airspeed sweep, extends from the aircraft's low-speed limit to its high-speed limit. At the lowest weight coefficient, the aircraft's low-speed limit is the hover point, but at higher weight coefficients, the aircraft cannot hover and the low-speed limit is as shown here. The high-speed limit may be caused by the power required to overcome transonic drag or dynamic stall. In some cases, the weight coefficient was varied by adding ballast to the UH-60A, but in most cases it was varied by flying at progressively higher altitudes. The highest airspeed sweep here was obtained at 17,000 feet.

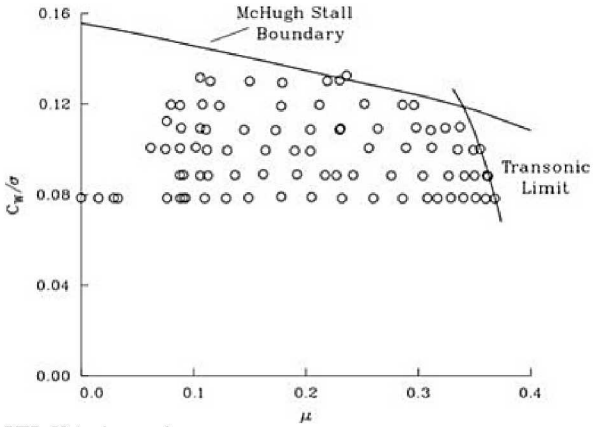

UH-60A airspeed sweeps

The airspeed sweeps at 6 weight coefficients from the Airloads Program are compared with flight data from four previous UH-60A performance tests (Nagata et al. 1981, Marshall et al. 1985, Buckanin et al. 1988, Nagata et al. 1989) in the offset plot. In general, there is good agreement between prior tests and the Airloads Program. It is valuable that there is good repeatability with these tests, but what is most important is that for all the present test points, blade pressure data are available. This means that detailed investigations of blade aerodynamics and structural dynamics may be examined and a better understanding of how they affect performance can be obtained.

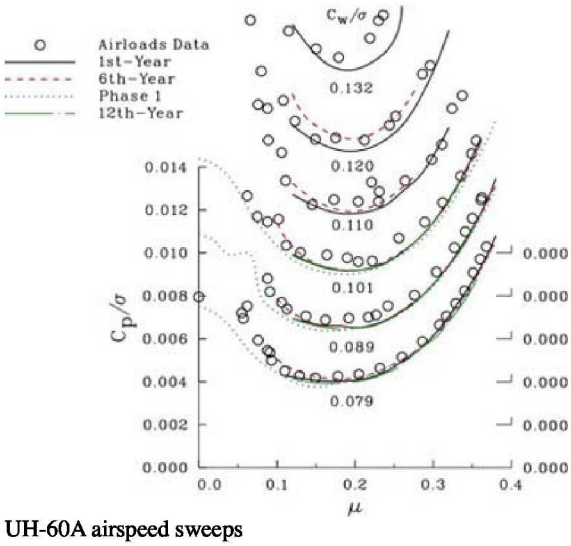

UH-60A airspeed sweeps

As with other checks for experimental consistency in the Airloads Program, it is possible to examine the power balance in the engine drive train (Bousman 2002a). The main rotor and tail rotor powers are measured, as are the powers transmitted by the engine output shafts. Using a measured transmission efficiency, it is possible to calculate a power difference. This difference should be the accessory power needed for hydraulics, electrical equipment, and so on. The accessory power is estimated to be about 60 HP, but for the six airspeed sweeps, much larger differences are shown here, ranging from -40 to 180 HP, suggesting that other factors are involved.

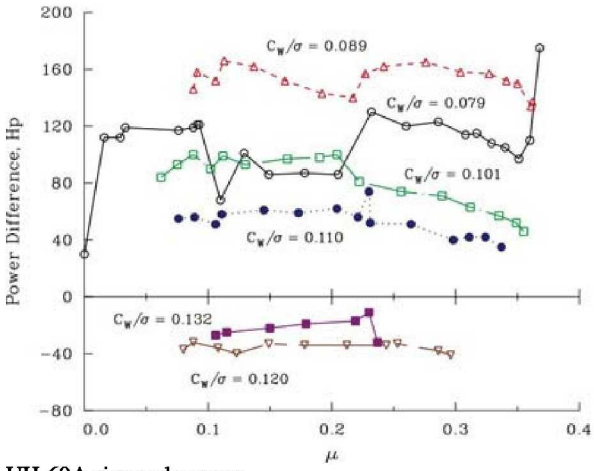

UH-60A airspeed sweeps

The airspeed sweeps were flown from near sea level to 17,000 feet, and the outside air temperatures (OAT) varied from 25 to -5 deg C. The power difference between the engines and rotor is shown here, and it is clear that this difference depends upon the OAT. This temperature effect is not accounted for in the calibrations of any of the drive train components, and the source of the error is unresolved.

Experiments, such as this UH-60A flight test program, will sometimes result in errors that are not understood, as shown here. (See also the problem with the steady thrust integration).

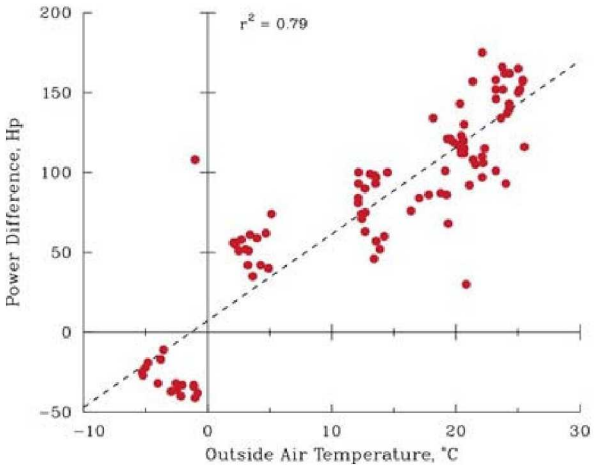

The figure shows a 3D Cartesian surface plot of blade normal force at r/R = 0.865 for advance ratios from 0.015 to 0.368. At low speeds, the normal force is dominated by rotor disk vortices that form at each side of the rotor disk. These disk vortices incorporate the individual tip vortices of each blade. As advance ratio increases, the vortex loading on either side of the rotor declines. At higher advance ratios, the normal force on the advancing side of the rotor disk is reduced, eventually becoming negative. At this point, the loading becomes strongly transonic, and it is necessary that the section airfoils be near zero angle of attack to reduce the effects of transonic drag rise.

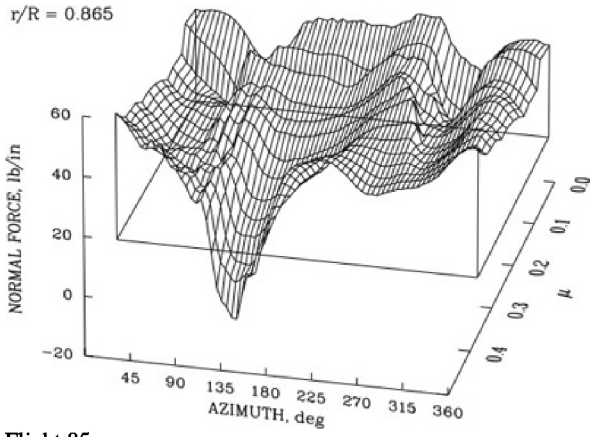

Flight 85

The figure shows a Cartesian surface plot of blade pitching moment at r/R = 0.865 for advance ratios from 0.015 to 0.368. At low speeds the disk vortices that form on each side of the rotor disk cause oscillatory moments, but unlike the case of normal force, these loads are slight. Negative moments on the advancing side become more pronounced at higher advance ratios. The loading becomes strongly transonic and the pitching moments are greatest at these high speeds. These negative moments twist the rotor blade, which in turn changes the blade loading, a classical case of aeroelastic feedback.

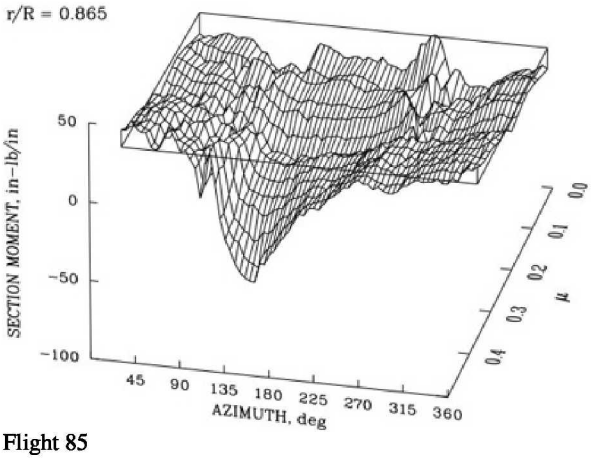

Flight 85

The rotor blade loads are low near hover. As airspeed increases, as shown in Figure 1 for the flap bending moments at the midspan of the blade, the half peak-to-peak loads (1 to 24 harmonics) increase, being greatest at high speed. These are the loads that will cause fatigue damage if they are too large. Thus, the high-speed regime is important for structural design. Vibratory loads that may be transmitted to the fuselage (3 to 24 harmonics) are large at low speed, because of the disk vortices. At high speed, these loads become large because of changes in dynamic pressure and transonic loading around the azimuth. Thus, both forward speed regimes are important for vibration.

The rotor blade chord bending moments, as shown in Figure 2, are low near hover, as was observed for the flap bending moments. As airspeed increases, the half peak-to-peak loads (1 to 24 harmonics) increase, being greatest at high speed. These are the loads that will cause fatigue damage if they are too large. Vibratory loads that may be transmitted to the fuselage (3 to 24 harmonics) are large at low speed, because of the disk vortices. At high speed, the loading becomes large because of changes in dynamic pressure and transonic loading around the azimuth. Thus, as was the case for the flap bending moments, both forward-speed regimes are important for vibration.

The rotor blade torsion moments, shown in Figure 3 at r/R = 0.30 are low near hover. As airspeed increases, the half peak-to-peak loads (1 to 24 harmonics) increase, being greatest at high speed. As was the case with the flap and chord bending moments, knowing the loads at high speed are important for structural design. The vibratory moments, on the other hand are equally severe in both the low-speed and high-speed regimes.

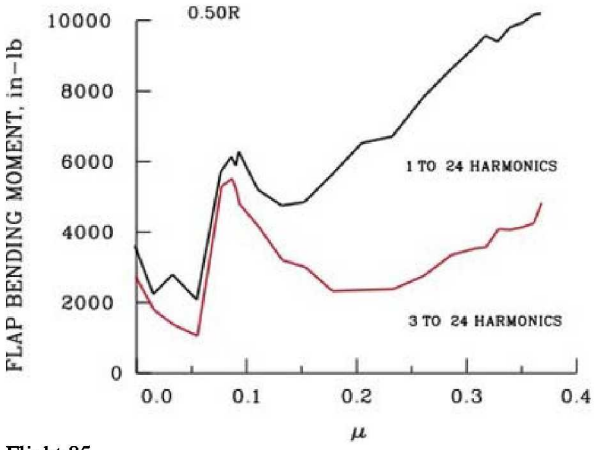

Flight 85

The rotor blade loads are low near hover. As airspeed increases, as shown in Figure 1 for the flap bending moments at the midspan of the blade, the half peak-to-peak loads (1 to 24 harmonics) increase, being greatest at high speed. These are the loads that will cause fatigue damage if they are too large. Thus, the high-speed regime is important for structural design. Vibratory loads that may be transmitted to the fuselage (3 to 24 harmonics) are large at low speed, because of the disk vortices. At high speed, these loads become large because of changes in dynamic pressure and transonic loading around the azimuth. Thus, both forward speed regimes are important for vibration.

The rotor blade chord bending moments, as shown in Figure 2, are low near hover, as was observed for the flap bending moments. As airspeed increases, the half peak-to-peak loads (1 to 24 harmonics) increase, being greatest at high speed. These are the loads that will cause fatigue damage if they are too large. Vibratory loads that may be transmitted to the fuselage (3 to 24 harmonics) are large at low speed, because of the disk vortices. At high speed, the loading becomes large because of changes in dynamic pressure and transonic loading around the azimuth. Thus, as was the case for the flap bending moments, both forward-speed regimes are important for vibration.

The rotor blade torsion moments, shown in Figure 3 at r/R = 0.30 are low near hover. As airspeed increases, the half peak-to-peak loads (1 to 24 harmonics) increase, being greatest at high speed. As was the case with the flap and chord bending moments, knowing the loads at high speed are important for structural design. The vibratory moments, on the other hand are equally severe in both the low-speed and high-speed regimes.

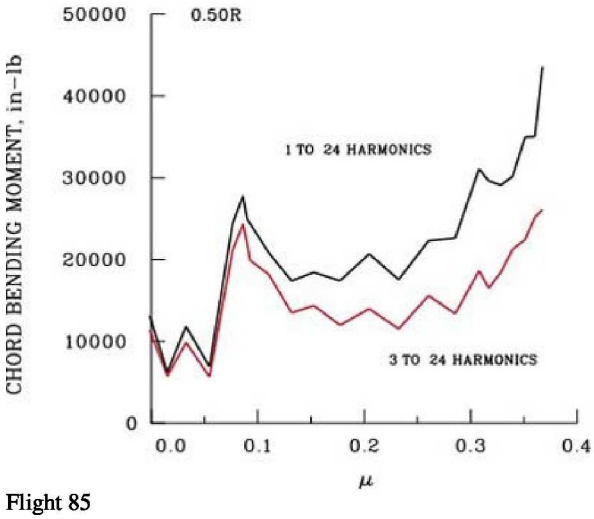

Flight 85

The rotor blade loads are low near hover. As airspeed increases, as shown in Figure 1 for the flap bending moments at the midspan of the blade, the half peak-to-peak loads (1 to 24 harmonics) increase, being greatest at high speed. These are the loads that will cause fatigue damage if they are too large. Thus, the high-speed regime is important for structural design. Vibratory loads that may be transmitted to the fuselage (3 to 24 harmonics) are large at low speed, because of the disk vortices. At high speed, these loads become large because of changes in dynamic pressure and transonic loading around the azimuth. Thus, both forward speed regimes are important for vibration.

The rotor blade chord bending moments, as shown in Figure 2, are low near hover, as was observed for the flap bending moments. As airspeed increases, the half peak-to-peak loads (1 to 24 harmonics) increase, being greatest at high speed. These are the loads that will cause fatigue damage if they are too large. Vibratory loads that may be transmitted to the fuselage (3 to 24 harmonics) are large at low speed, because of the disk vortices. At high speed, the loading becomes large because of changes in dynamic pressure and transonic loading around the azimuth. Thus, as was the case for the flap bending moments, both forward-speed regimes are important for vibration.

The rotor blade torsion moments, shown in Figure 3 at r/R = 0.30 are low near hover. As airspeed increases, the half peak-to-peak loads (1 to 24 harmonics) increase, being greatest at high speed. As was the case with the flap and chord bending moments, knowing the loads at high speed are important for structural design. The vibratory moments, on the other hand are equally severe in both the low-speed and high-speed regimes.

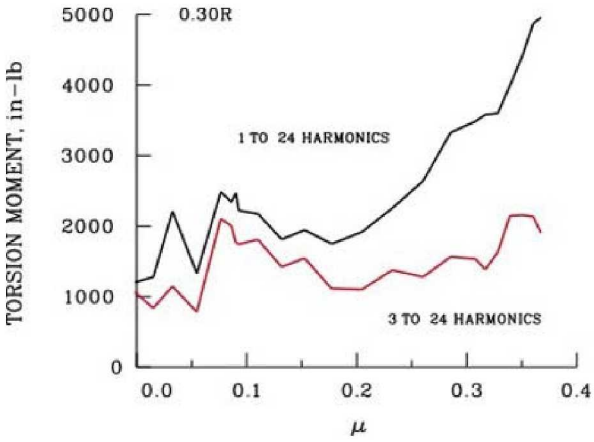

The offset plot here (0-120 harmonics) shows the azimuthal variation of the normal forces at nine radial stations for a low-speed condition, about $\mu = 0.09$. Disk vortices on either side of the rotor are caused by the individual blade tip vortices coalescing or wrapping around each other. The core size of the disk vortex is about 10 times the blade chord, and the effects of the disk vortices can be seen on the outer quarter of the blade. The down-up pulse on the advancing side and the up-down pulse on the retreating side excite the lower frequency blade modes, particularly in the range 3/rev to 5/rev. This disk vortex loading causes the severe vibration that is seen at low speeds in the transition regime.

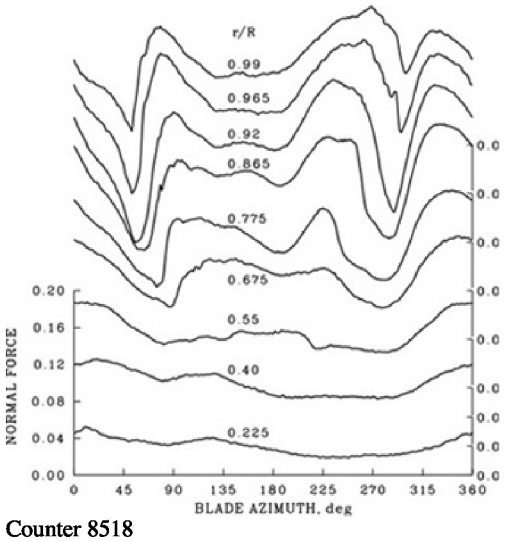

Counter 8518

Acoustic radiation is slight in low-speed, level flight. The offset plot here (17-120 harmonics) shows the azimuthal variation of the normal forces at nine radial stations at about $\mu = 0.09$. By removing the lower frequency harmonics, the contributions of a few tip vortices that have not entirely coalesced within the disk vortices are shown. These individual vortices are fewer and smaller than the vortex chains seen in descending flight. Thus, this low-speed condition, although important for fuselage vibration, does not generate the acoustic energy that is seen in typical approach conditions (descending flight).

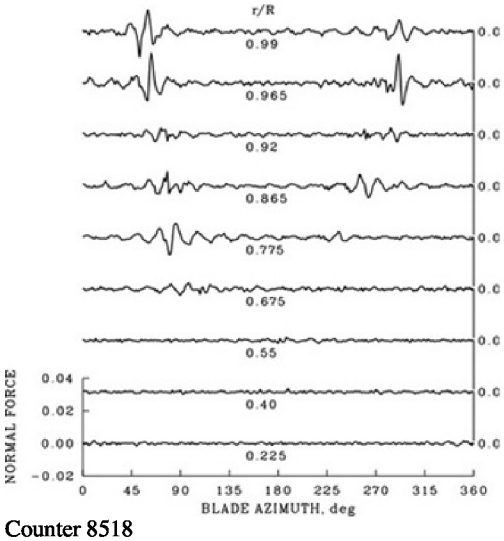

Counter 8518

In this figure, harmonics 3 to 120 of the aerodynamic forces at $r/R = 0.865$ are shown as a cycle plot for the low-speed vibration condition. These aerodynamic vibratory forces, which are the source of the vibration that is felt in the UH-60A cockpit, are seen to be invariant over the five-second duration (20 revolutions or cycles) of this test point.

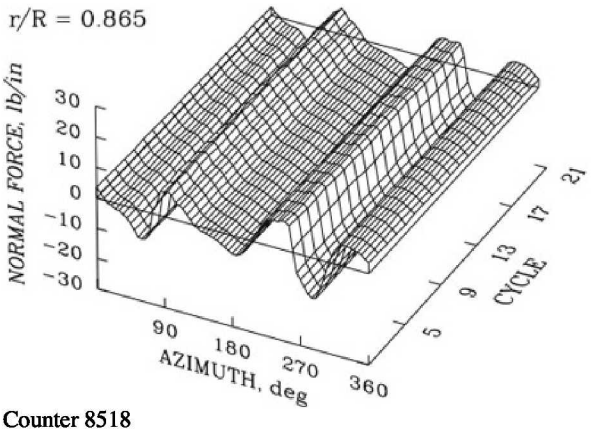

Counter 8518

A cycle plot is shown in Figure 1 for the flap bending response to the airloads for the low-speed vibration case (3–24 harmonics). The loads shown here are fairly invariant, but less so than the airloads on the previous tab. The flap bending moments at the other radial stations are not this steady. In particular, the loads measured at $r/R = 0.113$ show substantially more variation (click on the arrow). Moreover, the dominant 3/rev loads shown here are canceled within the rotating system and only the 4/rev (and 8/rev and so on) will affect the pilot seat vibration.

The cycle plot (Figure 2) of the flap bending vibratory response to the airloads at the blade root (3–24 harmonics) is highly variable, unlike the vibratory loads at the midspan (first figure). For an articulated rotor, the vibratory flap bending moments distributed along the blade combine to form shears at the effective hinge point. It is these shears that combine or cancel, depending upon their frequency, and are transmitted through the rotor hub to the fuselage to cause vibration.

Counter 8518.

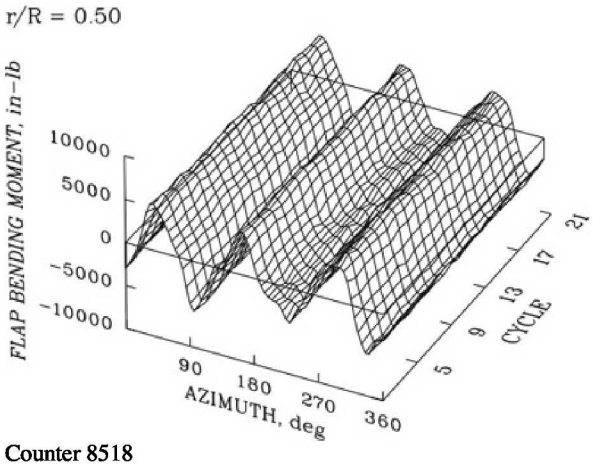

Counter 8518

A cycle plot is shown in Figure 1 for the flap bending response to the airloads for the low-speed vibration case (3–24 harmonics). The loads shown here are fairly invariant, but less so than the airloads on the previous tab. The flap bending moments at the other radial stations are not this steady. In particular, the loads measured at $r/R = 0.113$ show substantially more variation (click on the arrow). Moreover, the dominant 3/rev loads shown here are canceled within the rotating system and only the 4/rev (and 8/rev and so on) will affect the pilot seat vibration.

The cycle plot (Figure 2) of the flap bending vibratory response to the airloads at the blade root (3–24 harmonics) is highly variable, unlike the vibratory loads at the midspan (first figure). For an articulated rotor, the vibratory flap bending moments distributed along the blade combine to form shears at the effective hinge point. It is these shears that combine or cancel, depending upon their frequency, and are transmitted through the rotor hub to the fuselage to cause vibration.

Counter 8518.

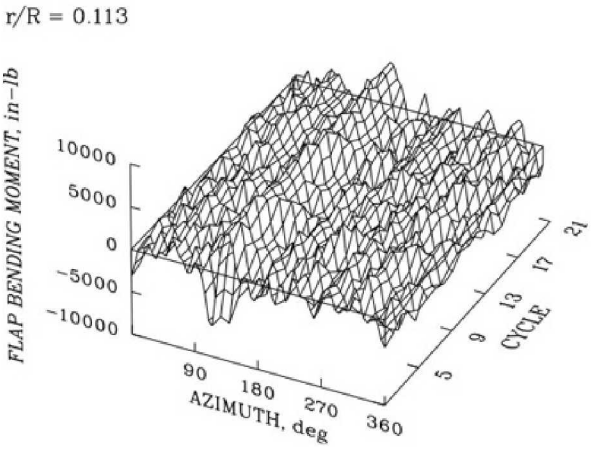

A cycle plot of the chord bending moment at $r/R = 0.50$ is shown in Figure 1 for the low-speed vibration case (3 to 24 harmonics). The chordwise structural response is more variable than was seen for the flap bending moment at the same radius on the previous tab. The variability here is typical of blade midspan locations, but the vibratory chord bending moments are more variable outboard and less variable inboard (click on the arrow). The 4/rev loads shown here will cancel in the rotating system, while 3/rev and 5/rev shears will transfer to the fuselage and cause vibration.

The chordwise structural response at $r/R = 0.113$ is less variable than was seen at the midspan station. It is surprising, perhaps, that the vibratory chord bending moments are invariant at this station whereas the flap bending moments at $r/R = 0.113$ where highly variable. In part this is caused by the lag damper forces which dominate the chord bending moments inboard, whereas the flap bending moments are only slightly affected by the damper forces. A correct calculation of any of these vibratory loads must correctly calculate both the airloads and the structural responses.

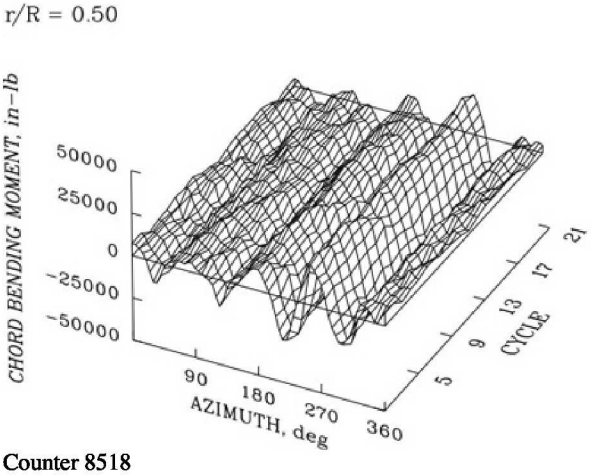

Counter 8518

A cycle plot of the chord bending moment at $r/R = 0.50$ is shown in Figure 1 for the low-speed vibration case (3 to 24 harmonics). The chordwise structural response is more variable than was seen for the flap bending moment at the same radius on the previous tab. The variability here is typical of blade midspan locations, but the vibratory chord bending moments are more variable outboard and less variable inboard (click on the arrow). The 4/rev loads shown here will cancel in the rotating system, while 3/rev and 5/rev shears will transfer to the fuselage and cause vibration.

The chordwise structural response at $r/R = 0.113$ is less variable than was seen at the midspan station. It is surprising, perhaps, that the vibratory chord bending moments are invariant at this station whereas the flap bending moments at $r/R = 0.113$ where highly variable. In part this is caused by the lag damper forces which dominate the chord bending moments inboard, whereas the flap bending moments are only slightly affected by the damper forces. A correct calculation of any of these vibratory loads must correctly calculate both the airloads and the structural responses.

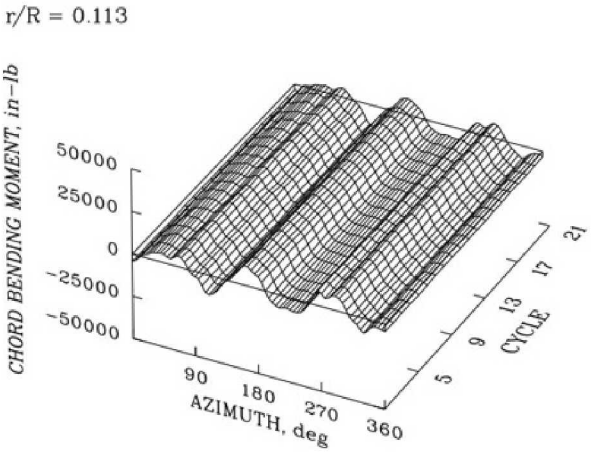

The vertical vibration at the pilot's seat is shown as a cycle plot for the low-speed vibration case (3 to 5 harmonics). Despite the steadiness that was seen in the airloads, the acceleration over the same period is modulated with the acceleration increasing and decreasing every few cycles. The vibration in the fuselage depends upon the additive effects of the airloads, bending moments, and shears on all of the four blades, not just the loads measured on a single blade. To accurately predict fuselage vibration requires not only the accurate calculation of the airloads, but also the effects of dissimilarities between the various blades, whether in the input forces or in the structural response.

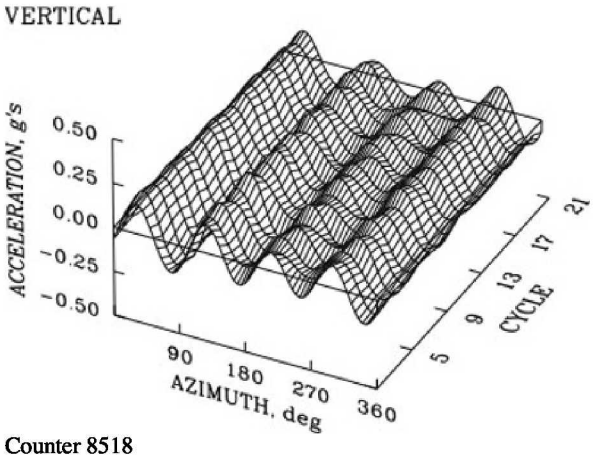

Counter 8518

An offset plot of the blade normal forces (0–120 harmonics) at the maximum flight speed shows that the lift on the blade becomes negative in the second quadrant (negative lift shown in red). In this quadrant, the lift becomes negative outboard of $r/R = 0.775$. The lift reduction is related to high Mach numbers on the airfoil and the need for low angles of attack to minimize airfoil drag and rotor power. The changes in these forces during a single revolution have a significant impact on blade loads. There is also a small area of negative lift on the retreating side, inboard at 0.225R. At this radial station there is an area of reversed flow that extends over about 90 deg.

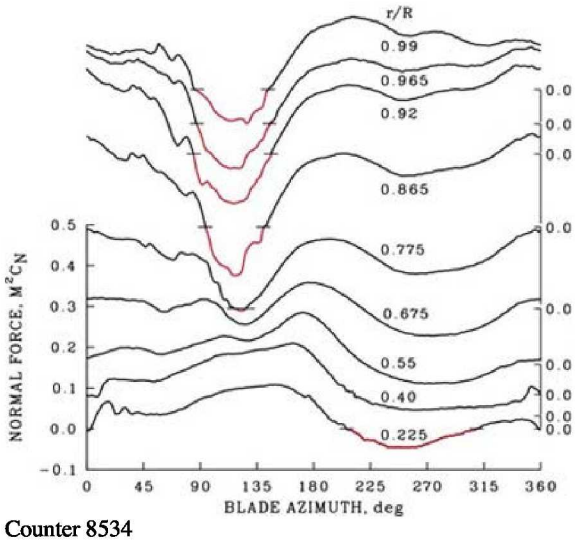

Counter 8534

An offset plot of the blade pitching moments (1–120 harmonics) at the maximum flight speed shows that there are strong negative moments near the blade tip associated with the high Mach numbers and negative lift in the second quadrant. These negative moments cause elastic twisting of the blade, significantly affect the lift distribution, and contribute to high structural loads and vibration. The moment distribution at the tip ($r/R = 0.99$) shows a different pattern because of lift from the tip vortex. There is an area of positive pitching moment on the retreating side, inboard at $r/R = 0.225$, that is caused by the shift in lift in reversed flow.

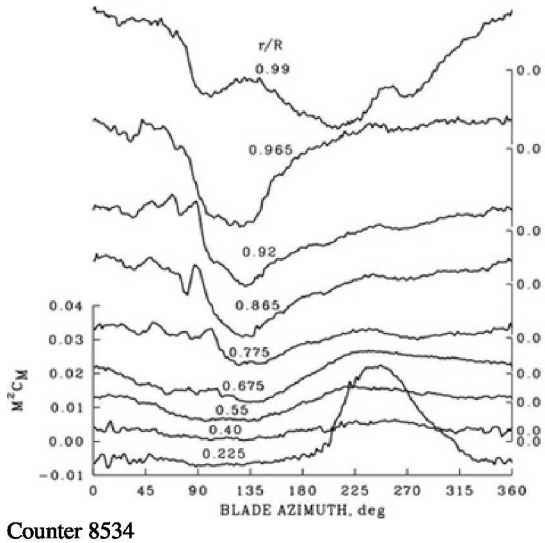

Counter 8534

The 3D Cartesian surface plot of upper surface pressures in high-speed flight shows the importance of transonic flow over the blade sections. The thickened red line shows the loci of the critical pressure coefficient, c_p^*, which is the boundary of supersonic flow and an indicator of the increased nonlinear drag associated with shock formation on the airfoil. In the first quadrant, before the blade lift becomes negative, there is a region of supersonic flow, with the shock extending beyond 0.32c. There is also a small region ofsupersonic flow near the airfoil leading edge in the fourth quadrant. This supersonic flow is caused by the high angle of attack, but there is no stall.

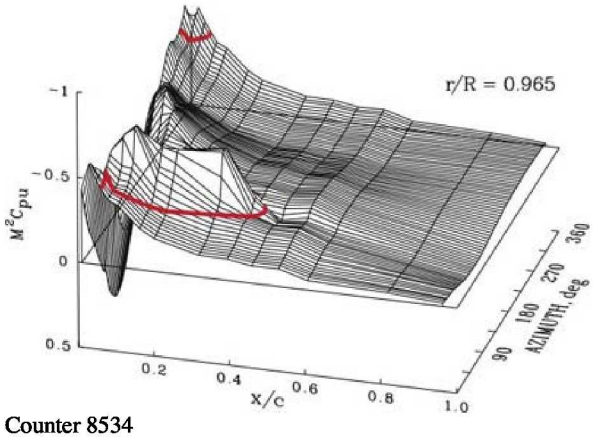

Counter 8534

The 3D Cartesian surface plot of lower surface pressures in high-speed flight shows the development of extensive supersonic flow on the lower surface of the airfoil as negative lift develops in the second quadrant. The thickened red line shows the loci of the critical pressure coefficient, c_p^*, which is the boundary of supersonic flow and an indicator of the increased nonlinear drag associated with shock formation on the airfoil. As is observed on the upper surface pressures in the first quadrant, the shock on the lower surface extends back beyond 0.32c. The nonlinear transonic drag associated with this shock increases the required rotor power and limits the UH-60A's airspeed.

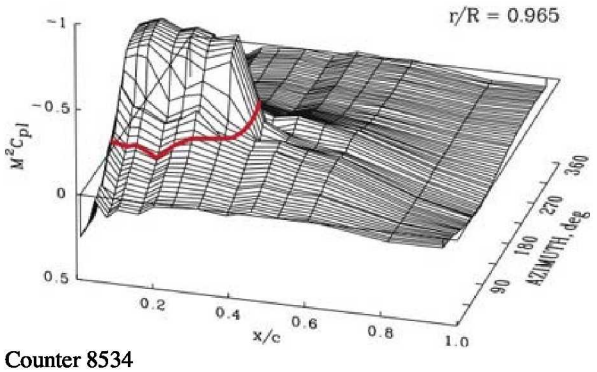

Counter 8534

The UH-60A's high-speed limit conditions were discussed before, but in a relatively simplified manner. This limit, which is an aircraft power limit, is examined in more detail here. The focus is on the six maximum-speed counters (shown as solid red symbols) for the six weight coefficient sweeps in the figure. As already discussed, the speed limit at the lowest weight coefficient is dominated by transonic drag. But as the weight coefficient (rotor thrust) increases, the character of the aerodynamic loading changes. The high angle of attack loading as the blade nears stall becomes more important. At the highest weight coefficients, dynamic stall becomes dominant.

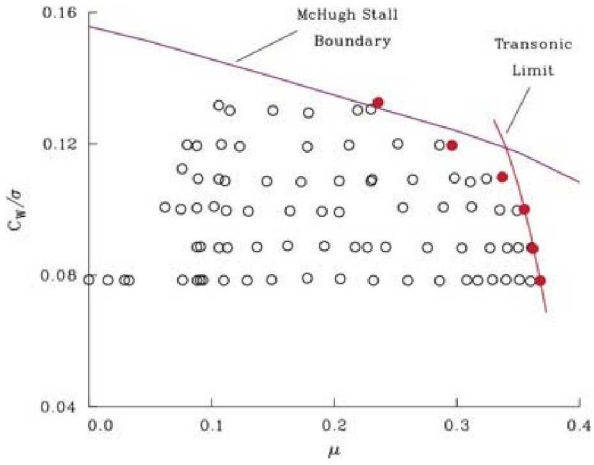

Normal force at 0.865R (0-120 harmonics) is shown in an offset plot. The offsets are the six weight coefficients, the highest weight coefficient at the top. At the lowest weight coefficient, as already discussed, the power limit is caused by transonic drag in the second quadrant. As weight coefficient is increased, the area of negative lift (shown in red) decreases in extent and severity. At $C_W/\sigma = 0.110$, some lift stall is observed in the fourth quadrant (shown by red arrow). At higher weight coefficients, two areas of lift stall are seen and these occur progressively earlier in the third and fourth quadrants. The power limit for this rotorcraft changes over this range from transonic drag to dynamic stall.

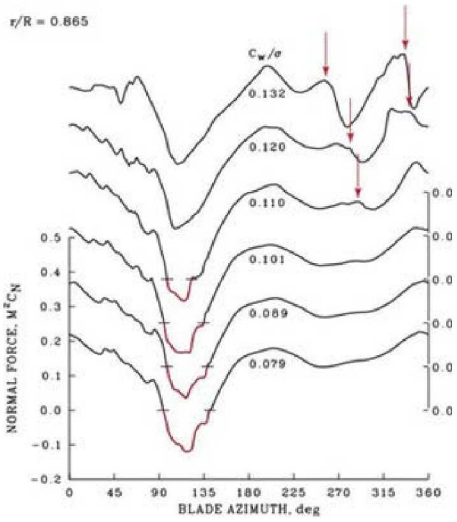

Pitching moments at r/R = 0.865 (1–120 harmonics) are shown in an offset plot. The offsets are the six weight coefficients. As thrust increases, the first indication of dynamic stall is seen at $C_W/\sigma = 0.110$, where moment stall occurs in the fourth quadrant (shown by red arrow). At higher weight coefficients, two areas of moment stall are seen and these occur progressively earlier in the third and fourth quadrants. These dynamic stall events result in rapid increases in airfoil drag that cause the rotor's power limit. At the same time, the large increases in pitching moment cause substantial increases in the rotor torsion moments and control-system loads.

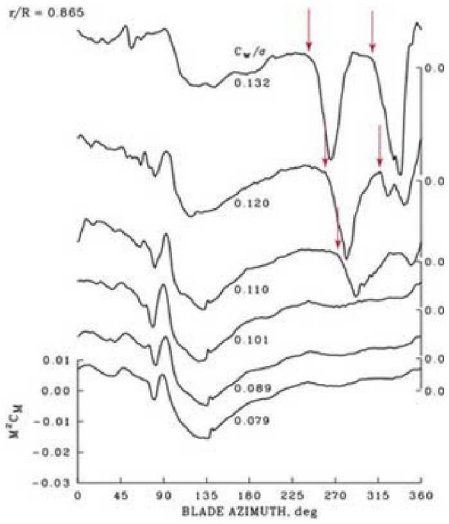

The upper surface blade pressures at $r/R = 0.865$ are shown in an offset plot (Figure 1), where the offset is in the chordwise pressure transducer location, the leading edge at the top. The data here are for $C_W/\sigma = 0.079$, which is the lowest thrust condition, as previously described. The red circles show the critical pressure or sonic line, where the flow locally becomes supersonic on the airfoil. This occurs in the first quadrant, with supersonic flow extending back to 0.395c. The flow becomes subsonic again as the lift becomes negative in the second quadrant. There are also patches of supersonic flow that occur on the retreating side of the blade at high lift, but there is no evidence of stall.

The upper surface blade pressures are again shown in an offset plot (Figure 2), where the offset is in the chordwise pressure transducer location, the leading edge at the top. The data here are for $C_W/\sigma = 0.089$. The red circles again show the critical pressure or sonic line, where the flow locally becomes supersonic on the airfoil. The flow is very similar to the previous case, there is supersonic flow on the airfoil surface in the first quadrant extending back to 0.395c. The shock wave passing over the pressure transducers is apparent as a very steep pressure gradient near the sonic line. Again, there are small patches of supersonic flow on the retreating side of the rotor at high airfoil angles of attack.

The upper surface blade pressures at$C_W/\sigma = 0.101$ are shown in an offset plot (Figure 3). This is the fourth highest rotor thrust case of the six limit-speed cases. Compared to the previous thrust case, the supersonic flow is slightly reduced in extent, occurring only as far back as 0.320c. There is a disturbance in the supersonic flow at high angles of attack in the fourth quadrant, and this may be incipient dynamic stall, with a possible stall vortex shed extending back as far as 0.164c. If so, the overall effect is slight and no change in pitching moment is observed in the pitching moment data (next tab).

The upper surface blade pressures at $C_W/\sigma = 0.110$ are shown in an offset plot (Figure 4). This is the limit-speed case for the third highest thrust condition. As thrust increases, the area of supersonic flow in the first quadrant is reduced, but supersonic flow is still observed as far back as 0.395c. Two pressure disturbances are seen in the fourth quadrant, and these are caused by the shedding of dynamic stall vortices near the airfoil's leading edge. The disturbances are indicated with red lines. The first disturbance extends nearly to the airfoil's trailing edge and causes a significant negative pitching moment. The second and weaker stall vortex is no longer observed past 0.530c.

The upper surface blade pressures at $C_W/\sigma = 0.120$ are shown in an offset plot (Figure 5). This is the limit speed at the second highest thrust condition. There continues to be a large area of transonic flow in the first quadrant, with supersonic flow extending back to 0.395c. Two cycles of dynamic stall are again seen in the fourth quadrant. The first dynamic stall vortex extends to the airfoil's trailing edge, causing the flow to separate, but the second stall vortex is less powerful. The rotor's power is significantly affected by the supersonic flow in the first quadrant and the extra drag from dynamic stall in the fourth quadrant.

The upper surface blade pressures at $C_W/\sigma = 0.132$ are shown in an offset plot (Figure 6). This is the limit speed case for the highest thrust condition. Although the airspeed at this condition is much reduced from the lowest thrust case ($\mu = 0.236$ versus 0.368), there is still extensive supersonic

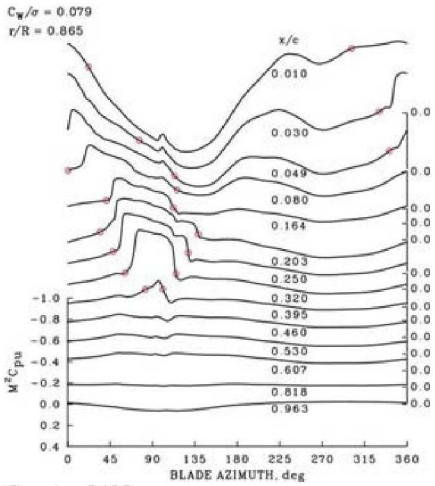

Counter 8428

flow in the first quadrant. The two dynamic stall vortices seen in the previous thrust case are stronger than before, both vortices extending to the trailing edge and causing separation. The vortices now occur earlier, with the first appearing at the end of the third quadrant. The dynamic stall vortices have a significant effect on rotor power and loads.

The upper surface blade pressures at $r/R = 0.865$ are shown in an offset plot (Figure 1), where the offset is in the chordwise pressure transducer location, the leading edge at the top. The data here are for $C_W/\sigma = 0.079$, which is the lowest thrust condition, as previously described. The red circles show the critical pressure or sonic line, where the flow locally becomes supersonic on the airfoil. This occurs in the first quadrant, with supersonic flow extending back to 0.395c. The flow becomes subsonic again as the lift becomes negative in the second quadrant. There are also patches of supersonic flow that occur on the retreating side of the blade at high lift, but there is no evidence of stall.

The upper surface blade pressures are again shown in an offset plot (Figure 2), where the offset is in the chordwise pressure transducer location, the leading edge at the top. The data here are for $C_W/\sigma = 0.089$. The red circles again show the critical pressure or sonic line, where the flow locally becomes supersonic on the airfoil. The flow is very similar to the previous case, there is supersonic flow on the airfoil surface in the first quadrant extending back to 0.395c. The shock wave passing over the pressure transducers is apparent as a very steep pressure gradient near the sonic line. Again, there are small patches of supersonic flow on the retreating side of the rotor at high airfoil angles of attack.

The upper surface blade pressures at$C_W/\sigma = 0.101$ are shown in an offset plot (Figure 3). This is the fourth highest rotor thrust case of the six limit-speed cases. Compared to the previous thrust case, the supersonic flow is slightly reduced in extent, occurring only as far back as 0.320c. There is a disturbance in the supersonic flow at high angles of attack in the fourth quadrant, and this may be incipient dynamic stall, with a possible stall vortex shed extending back as far as 0.164c. If so, the overall effect is slight and no change in pitching moment is observed in the pitching moment data (next tab).

The upper surface blade pressures at $C_W/\sigma = 0.110$ are shown in an offset plot (Figure 4). This is the limit-speed case for the third highest thrust condition. As thrust increases, the area of supersonic flow in the first quadrant is reduced, but supersonic flow is still observed as far back as 0.395c. Two pressure disturbances are seen in the fourth quadrant, and these are caused by the shedding of dynamic stall vortices near the airfoil's leading edge. The disturbances are indicated with red lines. The first disturbance extends nearly to the airfoil's trailing edge and causes a significant negative pitching moment. The second and weaker stall vortex is no longer observed past 0.530c.

The upper surface blade pressures at $C_W/\sigma = 0.120$ are shown in an offset plot (Figure 5). This is the limit speed at the second highest thrust condition. There continues to be a large area of transonic flow in the first quadrant, with supersonic flow extending back to 0.395c. Two cycles of dynamic stall are again seen in the fourth quadrant. The first dynamic stall vortex extends to the airfoil's trailing edge, causing the flow to separate, but the second stall vortex is less powerful. The rotor's power is significantly affected by the supersonic flow in the first quadrant and the extra drag from dynamic stall in the fourth quadrant.

The upper surface blade pressures at $C_W/\sigma = 0.132$ are shown in an offset plot (Figure 6). This is the limit speed case for the highest thrust condition. Although the airspeed at this condition is much reduced from the lowest thrust case ($\mu = 0.236$ versus 0.368), there is still extensive supersonic flow in the first quadrant. The two dynamic stall vortices seen in the

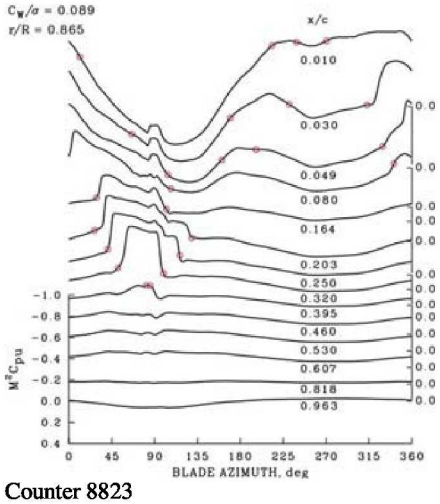

Counter 8823

previous thrust case are stronger than before, both vortices extending to the trailing edge and causing separation. The vortices now occur earlier, with the first appearing at the end of the third quadrant. The dynamic stall vortices have a significant effect on rotor power and loads.

The upper surface blade pressures at $r/R = 0.865$ are shown in an offset plot (Figure 1), where the offset is in the chordwise pressure transducer location, the leading edge at the top. The data here are for $C_W/\sigma = 0.079$, which is the lowest thrust condition, as previously described. The red circles show the critical pressure or sonic line, where the flow locally becomes supersonic on the airfoil. This occurs in the first quadrant, with supersonic flow extending back to 0.395c. The flow becomes subsonic again as the lift becomes negative in the second quadrant. There are also patches of supersonic flow that occur on the retreating side of the blade at high lift, but there is no evidence of stall.

The upper surface blade pressures are again shown in an offset plot (Figure 2), where the offset is in the chordwise pressure transducer location, the leading edge at the top. The data here are for $C_W/\sigma = 0.089$. The red circles again show the critical pressure or sonic line, where the flow locally becomes supersonic on the airfoil. The flow is very similar to the previous case, there is supersonic flow on the airfoil surface in the first quadrant extending back to 0.395c. The shock wave passing over the pressure transducers is apparent as a very steep pressure gradient near the sonic line. Again, there are small patches of supersonic flow on the retreating side of the rotor at high airfoil angles of attack.

The upper surface blade pressures at$C_W/\sigma = 0.101$ are shown in an offset plot (Figure 3). This is the fourth highest rotor thrust case of the six limit-speed cases. Compared to the previous thrust case, the supersonic flow is slightly reduced in extent, occurring only as far back as 0.320c. There is a disturbance in the supersonic flow at high angles of attack in the fourth quadrant, and this may be incipient dynamic stall, with a possible stall vortex shed extending back as far as 0.164c. If so, the overall effect is slight and no change in pitching moment is observed in the pitching moment data (next tab).

The upper surface blade pressures at $C_W/\sigma = 0.110$ are shown in an offset plot (Figure 4). This is the limit-speed case for the third highest thrust condition. As thrust increases, the area of supersonic flow in the first quadrant is reduced, but supersonic flow is still observed as far back as 0.395c. Two pressure disturbances are seen in the fourth quadrant, and these are caused by the shedding of dynamic stall vortices near the airfoil's leading edge. The disturbances are indicated with red lines. The first disturbance extends nearly to the airfoil's trailing edge and causes a significant negative pitching moment. The second and weaker stall vortex is no longer observed past 0.530c.

The upper surface blade pressures at $C_W/\sigma = 0.120$ are shown in an offset plot (Figure 5). This is the limit speed at the second highest thrust condition. There continues to be a large area of transonic flow in the first quadrant, with supersonic flow extending back to 0.395c. Two cycles of dynamic stall are again seen in the fourth quadrant. The first dynamic stall vortex extends to the airfoil's trailing edge, causing the flow to separate, but the second stall vortex is less powerful. The rotor's power is significantly affected by the supersonic flow in the first quadrant and the extra drag from dynamic stall in the fourth quadrant.

The upper surface blade pressures at $C_W/\sigma = 0.132$ are shown in an offset plot (Figure 6). This is the limit speed case for the highest thrust condition. Although the airspeed at this condition is much reduced from the lowest thrust case ($\mu = 0.236$ versus 0.368), there is still extensive supersonic flow in the first quadrant. The two dynamic stall vortices seen in the

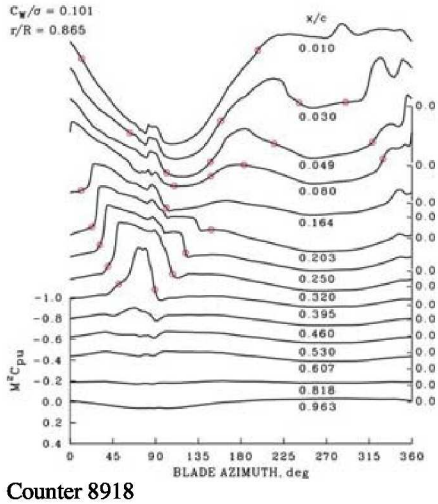

Counter 8918

previous thrust case are stronger than before, both vortices extending to the trailing edge and causing separation. The vortices now occur earlier, with the first appearing at the end of the third quadrant. The dynamic stall vortices have a significant effect on rotor power and loads.

The upper surface blade pressures at $r/R = 0.865$ are shown in an offset plot (Figure 1), where the offset is in the chordwise pressure transducer location, the leading edge at the top. The data here are for $C_W/\sigma = 0.079$, which is the lowest thrust condition, as previously described. The red circles show the critical pressure or sonic line, where the flow locally becomes supersonic on the airfoil. This occurs in the first quadrant, with supersonic flow extending back to 0.395c. The flow becomes subsonic again as the lift becomes negative in the second quadrant. There are also patches of supersonic flow that occur on the retreating side of the blade at high lift, but there is no evidence of stall.

The upper surface blade pressures are again shown in an offset plot (Figure 2), where the offset is in the chordwise pressure transducer location, the leading edge at the top. The data here are for $C_W/\sigma = 0.089$. The red circles again show the critical pressure or sonic line, where the flow locally becomes supersonic on the airfoil. The flow is very similar to the previous case, there is supersonic flow on the airfoil surface in the first quadrant extending back to 0.395c. The shock wave passing over the pressure transducers is apparent as a very steep pressure gradient near the sonic line. Again, there are small patches of supersonic flow on the retreating side of the rotor at high airfoil angles of attack.

The upper surface blade pressures at$C_W/\sigma = 0.101$ are shown in an offset plot (Figure 3). This is the fourth highest rotor thrust case of the six limit-speed cases. Compared to the previous thrust case, the supersonic flow is slightly reduced in extent, occurring only as far back as 0.320c. There is a disturbance in the supersonic flow at high angles of attack in the fourth quadrant, and this may be incipient dynamic stall, with a possible stall vortex shed extending back as far as 0.164c. If so, the overall effect is slight and no change in pitching moment is observed in the pitching moment data (next tab).

The upper surface blade pressures at $C_W/\sigma = 0.110$ are shown in an offset plot (Figure 4). This is the limit-speed case for the third highest thrust condition. As thrust increases, the area of supersonic flow in the first quadrant is reduced, but supersonic flow is still observed as far back as 0.395c. Two pressure disturbances are seen in the fourth quadrant, and these are caused by the shedding of dynamic stall vortices near the airfoil's leading edge. The disturbances are indicated with red lines. The first disturbance extends nearly to the airfoil's trailing edge and causes a significant negative pitching moment. The second and weaker stall vortex is no longer observed past 0.530c.

The upper surface blade pressures at $C_W/\sigma = 0.120$ are shown in an offset plot (Figure 5). This is the limit speed at the second highest thrust condition. There continues to be a large area of transonic flow in the first quadrant, with supersonic flow extending back to 0.395c. Two cycles of dynamic stall are again seen in the fourth quadrant. The first dynamic stall vortex extends to the airfoil's trailing edge, causing the flow to separate, but the second stall vortex is less powerful. The rotor's power is significantly affected by the supersonic flow in the first quadrant and the extra drag from dynamic stall in the fourth quadrant.

The upper surface blade pressures at $C_W/\sigma = 0.132$ are shown in an offset plot (Figure 6). This is the limit speed case for the highest thrust condition. Although the airspeed at this condition is much reduced from the lowest thrust case ($\mu = 0.236$ versus 0.368), there is still extensive supersonic flow in the first quadrant. The two dynamic stall vortices seen in the previous

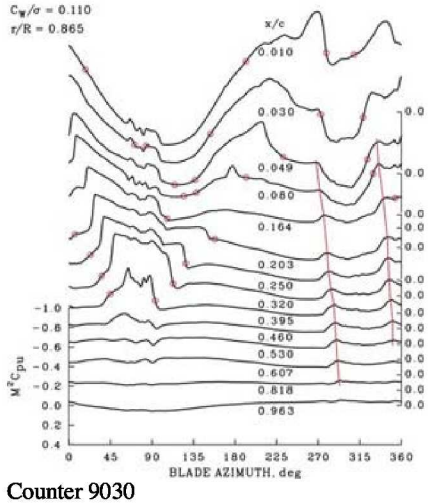

Counter 9030

thrust case are stronger than before, both vortices extending to the trailing edge and causing separation. The vortices now occur earlier, with the first appearing at the end of the third quadrant. The dynamic stall vortices have a significant effect on rotor power and loads.

The upper surface blade pressures at $r/R = 0.865$ are shown in an offset plot (Figure 1), where the offset is in the chordwise pressure transducer location, the leading edge at the top. The data here are for $C_W/\sigma = 0.079$, which is the lowest thrust condition, as previously described. The red circles show the critical pressure or sonic line, where the flow locally becomes supersonic on the airfoil. This occurs in the first quadrant, with supersonic flow extending back to 0.395c. The flow becomes subsonic again as the lift becomes negative in the second quadrant. There are also patches of supersonic flow that occur on the retreating side of the blade at high lift, but there is no evidence of stall.

The upper surface blade pressures are again shown in an offset plot (Figure 2), where the offset is in the chordwise pressure transducer location, the leading edge at the top. The data here are for $C_W/\sigma = 0.089$. The red circles again show the critical pressure or sonic line, where the flow locally becomes supersonic on the airfoil. The flow is very similar to the previous case, there is supersonic flow on the airfoil surface in the first quadrant extending back to 0.395c. The shock wave passing over the pressure transducers is apparent as a very steep pressure gradient near the sonic line. Again, there are small patches of supersonic flow on the retreating side of the rotor at high airfoil angles of attack.

The upper surface blade pressures at$C_W/\sigma = 0.101$ are shown in an offset plot (Figure 3). This is the fourth highest rotor thrust case of the six limit-speed cases. Compared to the previous thrust case, the supersonic flow is slightly reduced in extent, occurring only as far back as 0.320c. There is a disturbance in the supersonic flow at high angles of attack in the fourth quadrant, and this may be incipient dynamic stall, with a possible stall vortex shed extending back as far as 0.164c. If so, the overall effect is slight and no change in pitching moment is observed in the pitching moment data (next tab).

The upper surface blade pressures at $C_W/\sigma = 0.110$ are shown in an offset plot (Figure 4). This is the limit-speed case for the third highest thrust condition. As thrust increases, the area of supersonic flow in the first quadrant is reduced, but supersonic flow is still observed as far back as 0.395c. Two pressure disturbances are seen in the fourth quadrant, and these are caused by the shedding of dynamic stall vortices near the airfoil's leading edge. The disturbances are indicated with red lines. The first disturbance extends nearly to the airfoil's trailing edge and causes a significant negative pitching moment. The second and weaker stall vortex is no longer observed past 0.530c.

The upper surface blade pressures at $C_W/\sigma = 0.120$ are shown in an offset plot (Figure 5). This is the limit speed at the second highest thrust condition. There continues to be a large area of transonic flow in the first quadrant, with supersonic flow extending back to 0.395c. Two cycles of dynamic stall are again seen in the fourth quadrant. The first dynamic stall vortex extends to the airfoil's trailing edge, causing the flow to separate, but the second stall vortex is less powerful. The rotor's power is significantly affected by the supersonic flow in the first quadrant and the extra drag from dynamic stall in the fourth quadrant.

The upper surface blade pressures at $C_W/\sigma = 0.132$ are shown in an offset plot (Figure 6). This is the limit speed case for the highest thrust condition. Although the airspeed at this condition is much reduced from the lowest thrust case ($\mu = 0.236$ versus 0.368), there is still extensive supersonic flow in the first quadrant. The two dynamic stall vortices seen in the previous

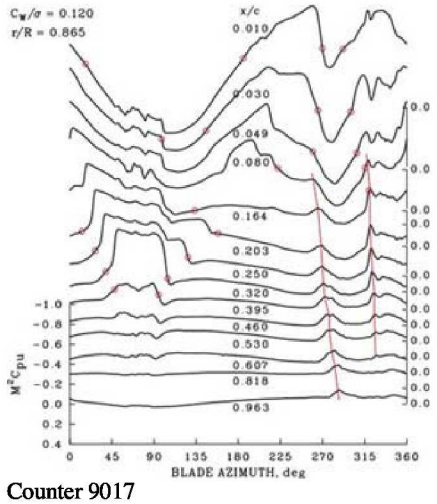

Counter 9017

thrust case are stronger than before, both vortices extending to the trailing edge and causing separation. The vortices now occur earlier, with the first appearing at the end of the third quadrant. The dynamic stall vortices have a significant effect on rotor power and loads.

The upper surface blade pressures at $r/R = 0.865$ are shown in an offset plot (Figure 1), where the offset is in the chordwise pressure transducer location, the leading edge at the top. The data here are for $C_W/\sigma = 0.079$, which is the lowest thrust condition, as previously described. The red circles show the critical pressure or sonic line, where the flow locally becomes supersonic on the airfoil. This occurs in the first quadrant, with supersonic flow extending back to 0.395c. The flow becomes subsonic again as the lift becomes negative in the second quadrant. There are also patches of supersonic flow that occur on the retreating side of the blade at high lift, but there is no evidence of stall.

The upper surface blade pressures are again shown in an offset plot (Figure 2), where the offset is in the chordwise pressure transducer location, the leading edge at the top. The data here are for $C_W/\sigma = 0.089$. The red circles again show the critical pressure or sonic line, where the flow locally becomes supersonic on the airfoil. The flow is very similar to the previous case, there is supersonic flow on the airfoil surface in the first quadrant extending back to 0.395c. The shock wave passing over the pressure transducers is apparent as a very steep pressure gradient near the sonic line. Again, there are small patches of supersonic flow on the retreating side of the rotor at high airfoil angles of attack.

The upper surface blade pressures at$C_W/\sigma = 0.101$ are shown in an offset plot (Figure 3). This is the fourth highest rotor thrust case of the six limit-speed cases. Compared to the previous thrust case, the supersonic flow is slightly reduced in extent, occurring only as far back as 0.320c. There is a disturbance in the supersonic flow at high angles of attack in the fourth quadrant, and this may be incipient dynamic stall, with a possible stall vortex shed extending back as far as 0.164c. If so, the overall effect is slight and no change in pitching moment is observed in the pitching moment data (next tab).

The upper surface blade pressures at $C_W/\sigma = 0.110$ are shown in an offset plot (Figure 4). This is the limit-speed case for the third highest thrust condition. As thrust increases, the area of supersonic flow in the first quadrant is reduced, but supersonic flow is still observed as far back as 0.395c. Two pressure disturbances are seen in the fourth quadrant, and these are caused by the shedding of dynamic stall vortices near the airfoil's leading edge. The disturbances are indicated with red lines. The first disturbance extends nearly to the airfoil's trailing edge and causes a significant negative pitching moment. The second and weaker stall vortex is no longer observed past 0.530c.

The upper surface blade pressures at $C_W/\sigma = 0.120$ are shown in an offset plot (Figure 5). This is the limit speed at the second highest thrust condition. There continues to be a large area of transonic flow in the first quadrant, with supersonic flow extending back to 0.395c. Two cycles of dynamic stall are again seen in the fourth quadrant. The first dynamic stall vortex extends to the airfoil's trailing edge, causing the flow to separate, but the second stall vortex is less powerful. The rotor's power is significantly affected by the supersonic flow in the first quadrant and the extra drag from dynamic stall in the fourth quadrant.

The upper surface blade pressures at $C_W/\sigma = 0.132$ are shown in an offset plot (Figure 6). This is the limit speed case for the highest thrust condition. Although the airspeed at this condition is much reduced from the lowest thrust case ($\mu = 0.236$ versus 0.368), there is still extensive supersonic flow in the first quadrant. The two dynamic stall vortices seen in the previous

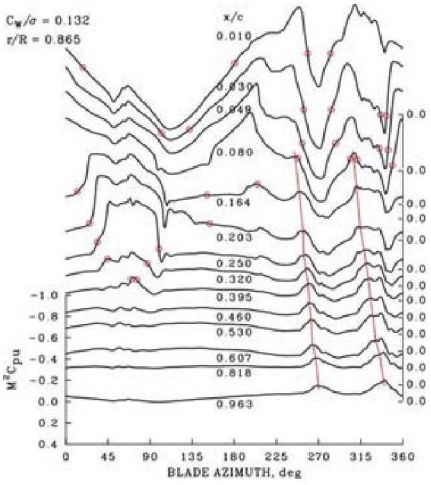

thrust case are stronger than before, both vortices extending to the trailing edge and causing separation. The vortices now occur earlier, with the first appearing at the end of the third quadrant. The dynamic stall vortices have a significant effect on rotor power and loads.

The lower surface blade pressures are shown in an offset plot (Figure 1), where the offset is in the chordwise pressure transducer location, the leading edge at the top. The data here are for $C_W/\sigma = 0.079$, which is the lowest thrust condition, previously described. The red circles show the critical pressure or sonic line, where the flow locally becomes supersonic on the airfoil. This occurs at end of the first quadrant and in the second as negative lift develops on the airfoil and the supersonic flow on the lower surface extends back to 0.250c. The flow becomes subsonic again as the lift becomes positive in the second quadrant.

The lower surface blade pressures are again shown in an offset plot (Figure 2). The data here are for $C_W/\sigma = 0.089$. The red circles show the critical pressure or sonic line, where the flow locally becomes supersonic on the airfoil. The flow is very similar to the previous case, supersonic flow develops on the lower surface at the end of the first quadrant as negative lift develops on the airfoil section. Then, as positive lift occurs in the second quadrant, the flow becomes subsonic again. Near the airfoil leading edge the supersonic flow develops without the presence of shock waves, but farther back on the airfoil shocks are apparent as they pass over the transducer locations.

The lower surface blade pressures for $C_W/\sigma = 0.101$ are shown in this offset plot (Figure 3). This is the fourth highest rotor thrust case of the six limit-speed conditions. The area of negative airfoil lift, although slightly reduced from the previous case, is still extensive. Otherwise, the development of supersonic flow on this lower surface is very similar to the previous cases.

The lower surface blade pressures at $C_W/\sigma = 0.110$ are shown in this offset plot (Figure 4). This is the limit-speed case for the third highest thrust condition. The extent of negative lift on the airfoil is reduced for this case, but the basic development of supersonic flow on the lower surface is the same as in previous cases. A dynamic stall vortex is observed at this condition on the upper surface, but the effects of this disturbance does not appear on the lower surface.

The lower surface blade pressures at $C_W/\sigma = 0.120$ are shown in this offset plot (Figure 5). This is the limit speed at the second highest thrust condition. There is no longer negative lift on the airfoil for this case, but some supersonic flow is observed on the lower surface and weak shocks occur. A weak disturbance is observed in the fourth quadrant, perhaps associated with the second of the two dynamic stall cycles on the upper surface. Also, separation at the airfoil trailing edge from the first dynamic stall cycle extends here onto the lower surface.

The lower surface blade pressures at $C_W/\sigma = 0.132$ are shown in an offset plot (Figure 6). This is the limit speed case for the highest thrust condition. Although the Mach number remains high on the lower surface for this condition, supersonic flow is now limited to only a few degrees of azimuth near 0.107c. Two disturbances in the blade pressures at the end of the third quadrant and the beginning of the fourth are related to the upper surface dynamic stall vortices. The trailing edge pressure separation observed here matches that seen on the upper surface.

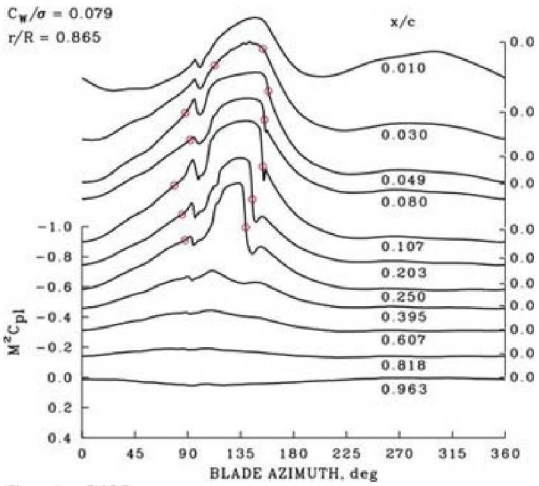

Counter 8428

The lower surface blade pressures are shown in an offset plot (Figure 1), where the offset is in the chordwise pressure transducer location, the leading edge at the top. The data here are for $C_W/\sigma = 0.079$, which is the lowest thrust condition, previously described. The red circles show the critical pressure or sonic line, where the flow locally becomes supersonic on the airfoil. This occurs at end of the first quadrant and in the second as negative lift develops on the airfoil and the supersonic flow on the lower surface extends back to 0.250c. The flow becomes subsonic again as the lift becomes positive in the second quadrant.

The lower surface blade pressures are again shown in an offset plot (Figure 2). The data here are for $C_W/\sigma = 0.089$. The red circles show the critical pressure or sonic line, where the flow locally becomes supersonic on the airfoil. The flow is very similar to the previous case, supersonic flow develops on the lower surface at the end of the first quadrant as negative lift develops on the airfoil section. Then, as positive lift occurs in the second quadrant, the flow becomes subsonic again. Near the airfoil leading edge the supersonic flow develops without the presence of shock waves, but farther back on the airfoil shocks are apparent as they pass over the transducer locations.

The lower surface blade pressures for $C_W/\sigma = 0.101$ are shown in this offset plot (Figure 3). This is the fourth highest rotor thrust case of the six limit-speed conditions. The area of negative airfoil lift, although slightly reduced from the previous case, is still extensive. Otherwise, the development of supersonic flow on this lower surface is very similar to the previous cases.

The lower surface blade pressures at $C_W/\sigma = 0.110$ are shown in this offset plot (Figure 4). This is the limit-speed case for the third highest thrust condition. The extent of negative lift on the airfoil is reduced for this case, but the basic development of supersonic flow on the lower surface is the same as in previous cases. A dynamic stall vortex is observed at this condition on the upper surface, but the effects of this disturbance does not appear on the lower surface.

The lower surface blade pressures at $C_W/\sigma = 0.120$ are shown in this offset plot (Figure 5). This is the limit speed at the second highest thrust condition. There is no longer negative lift on the airfoil for this case, but some supersonic flow is observed on the lower surface and weak shocks occur. A weak disturbance is observed in the fourth quadrant, perhaps associated with the second of the two dynamic stall cycles on the upper surface. Also, separation at the airfoil trailing edge from the first dynamic stall cycle extends here onto the lower surface.

The lower surface blade pressures at $C_W/\sigma = 0.132$ are shown in an offset plot (Figure 6). This is the limit speed case for the highest thrust condition. Although the Mach number remains high on the lower surface for this condition, supersonic flow is now limited to only a few degrees of azimuth near 0.107c. Two disturbances in the blade pressures at the end of the third quadrant and the beginning of the fourth are related to the upper surface dynamic stall vortices. The trailing edge pressure separation observed here matches that seen on the upper surface.

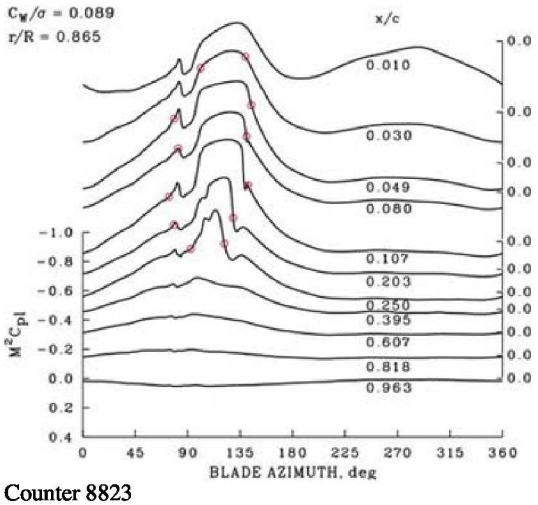

Counter 8823

The lower surface blade pressures are shown in an offset plot (Figure 1), where the offset is in the chordwise pressure transducer location, the leading edge at the top. The data here are for $C_W/\sigma = 0.079$, which is the lowest thrust condition, previously described. The red circles show the critical pressure or sonic line, where the flow locally becomes supersonic on the airfoil. This occurs at end of the first quadrant and in the second as negative lift develops on the airfoil and the supersonic flow on the lower surface extends back to 0.250c. The flow becomes subsonic again as the lift becomes positive in the second quadrant.

The lower surface blade pressures are again shown in an offset plot (Figure 2). The data here are for $C_W/\sigma = 0.089$. The red circles show the critical pressure or sonic line, where the flow locally becomes supersonic on the airfoil. The flow is very similar to the previous case, supersonic flow develops on the lower surface at the end of the first quadrant as negative lift develops on the airfoil section. Then, as positive lift occurs in the second quadrant, the flow becomes subsonic again. Near the airfoil leading edge the supersonic flow develops without the presence of shock waves, but farther back on the airfoil shocks are apparent as they pass over the transducer locations.

The lower surface blade pressures for $C_W/\sigma = 0.101$ are shown in this offset plot (Figure 3). This is the fourth highest rotor thrust case of the six limit-speed conditions. The area of negative airfoil lift, although slightly reduced from the previous case, is still extensive. Otherwise, the development of supersonic flow on this lower surface is very similar to the previous cases.

The lower surface blade pressures at $C_W/\sigma = 0.110$ are shown in this offset plot (Figure 4). This is the limit-speed case for the third highest thrust condition. The extent of negative lift on the airfoil is reduced for this case, but the basic development of supersonic flow on the lower surface is the same as in previous cases. A dynamic stall vortex is observed at this condition on the upper surface, but the effects of this disturbance does not appear on the lower surface.

The lower surface blade pressures at $C_W/\sigma = 0.120$ are shown in this offset plot (Figure 5). This is the limit speed at the second highest thrust condition. There is no longer negative lift on the airfoil for this case, but some supersonic flow is observed on the lower surface and weak shocks occur. A weak disturbance is observed in the fourth quadrant, perhaps associated with the second of the two dynamic stall cycles on the upper surface. Also, separation at the airfoil trailing edge from the first dynamic stall cycle extends here onto the lower surface.

The lower surface blade pressures at $C_W/\sigma = 0.132$ are shown in an offset plot (Figure 6). This is the limit speed case for the highest thrust condition. Although the Mach number remains high on the lower surface for this condition, supersonic flow is now limited to only a few degrees of azimuth near 0.107c. Two disturbances in the blade pressures at the end of the third quadrant and the beginning of the fourth are related to the upper surface dynamic stall vortices. The trailing edge pressure separation observed here matches that seen on the upper surface.

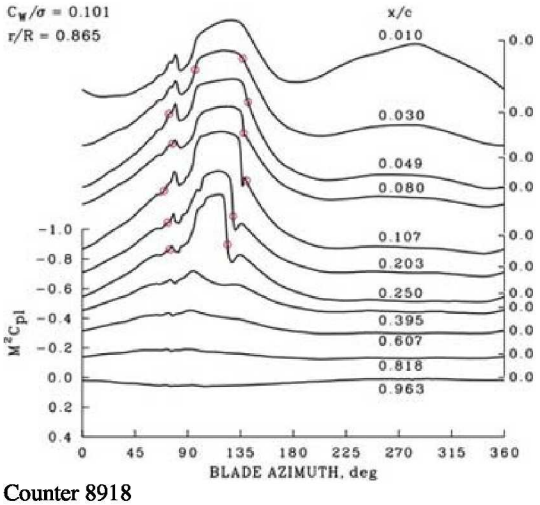

Counter 8918

The lower surface blade pressures are shown in an offset plot (Figure 1), where the offset is in the chordwise pressure transducer location, the leading edge at the top. The data here are for $C_W/\sigma = 0.079$, which is the lowest thrust condition, previously described. The red circles show the critical pressure or sonic line, where the flow locally becomes supersonic on the airfoil. This occurs at end of the first quadrant and in the second as negative lift develops on the airfoil and the supersonic flow on the lower surface extends back to 0.250c. The flow becomes subsonic again as the lift becomes positive in the second quadrant.

The lower surface blade pressures are again shown in an offset plot (Figure 2). The data here are for $C_W/\sigma = 0.089$. The red circles show the critical pressure or sonic line, where the flow locally becomes supersonic on the airfoil. The flow is very similar to the previous case, supersonic flow develops on the lower surface at the end of the first quadrant as negative lift develops on the airfoil section. Then, as positive lift occurs in the second quadrant, the flow becomes subsonic again. Near the airfoil leading edge the supersonic flow develops without the presence of shock waves, but farther back on the airfoil shocks are apparent as they pass over the transducer locations.

The lower surface blade pressures for $C_W/\sigma = 0.101$ are shown in this offset plot (Figure 3). This is the fourth highest rotor thrust case of the six limit-speed conditions. The area of negative airfoil lift, although slightly reduced from the previous case, is still extensive. Otherwise, the development of supersonic flow on this lower surface is very similar to the previous cases.

The lower surface blade pressures at $C_W/\sigma = 0.110$ are shown in this offset plot (Figure 4). This is the limit-speed case for the third highest thrust condition. The extent of negative lift on the airfoil is reduced for this case, but the basic development of supersonic flow on the lower surface is the same as in previous cases. A dynamic stall vortex is observed at this condition on the upper surface, but the effects of this disturbance does not appear on the lower surface.

The lower surface blade pressures at $C_W/\sigma = 0.120$ are shown in this offset plot (Figure 5). This is the limit speed at the second highest thrust condition. There is no longer negative lift on the airfoil for this case, but some supersonic flow is observed on the lower surface and weak shocks occur. A weak disturbance is observed in the fourth quadrant, perhaps associated with the second of the two dynamic stall cycles on the upper surface. Also, separation at the airfoil trailing edge from the first dynamic stall cycle extends here onto the lower surface.

The lower surface blade pressures at $C_W/\sigma = 0.132$ are shown in an offset plot (Figure 6). This is the limit speed case for the highest thrust condition. Although the Mach number remains high on the lower surface for this condition, supersonic flow is now limited to only a few degrees of azimuth near 0.107c. Two disturbances in the blade pressures at the end of the third quadrant and the beginning of the fourth are related to the upper surface dynamic stall vortices. The trailing edge pressure separation observed here matches that seen on the upper surface.

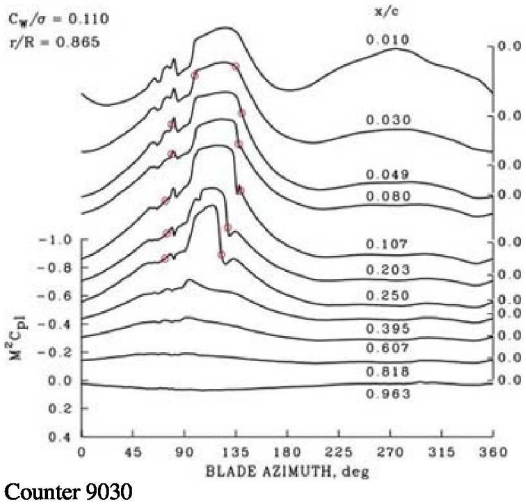

Counter 9030

The lower surface blade pressures are shown in an offset plot (Figure 1), where the offset is in the chordwise pressure transducer location, the leading edge at the top. The data here are for $C_W/\sigma = 0.079$, which is the lowest thrust condition, previously described. The red circles show the critical pressure or sonic line, where the flow locally becomes supersonic on the airfoil. This occurs at end of the first quadrant and in the second as negative lift develops on the airfoil and the supersonic flow on the lower surface extends back to 0.250c. The flow becomes subsonic again as the lift becomes positive in the second quadrant.

The lower surface blade pressures are again shown in an offset plot (Figure 2). The data here are for $C_W/\sigma = 0.089$. The red circles show the critical pressure or sonic line, where the flow locally becomes supersonic on the airfoil. The flow is very similar to the previous case, supersonic flow develops on the lower surface at the end of the first quadrant as negative lift develops on the airfoil section. Then, as positive lift occurs in the second quadrant, the flow becomes subsonic again. Near the airfoil leading edge the supersonic flow develops without the presence of shock waves, but farther back on the airfoil shocks are apparent as they pass over the transducer locations.

The lower surface blade pressures for $C_W/\sigma = 0.101$ are shown in this offset plot (Figure 3). This is the fourth highest rotor thrust case of the six limit-speed conditions. The area of negative airfoil lift, although slightly reduced from the previous case, is still extensive. Otherwise, the development of supersonic flow on this lower surface is very similar to the previous cases.

The lower surface blade pressures at $C_W/\sigma = 0.110$ are shown in this offset plot (Figure 4). This is the limit-speed case for the third highest thrust condition. The extent of negative lift on the airfoil is reduced for this case, but the basic development of supersonic flow on the lower surface is the same as in previous cases. A dynamic stall vortex is observed at this condition on the upper surface, but the effects of this disturbance does not appear on the lower surface.

The lower surface blade pressures at $C_W/\sigma = 0.120$ are shown in this offset plot (Figure 5). This is the limit speed at the second highest thrust condition. There is no longer negative lift on the airfoil for this case, but some supersonic flow is observed on the lower surface and weak shocks occur. A weak disturbance is observed in the fourth quadrant, perhaps associated with the second of the two dynamic stall cycles on the upper surface. Also, separation at the airfoil trailing edge from the first dynamic stall cycle extends here onto the lower surface.

The lower surface blade pressures at $C_W/\sigma = 0.132$ are shown in an offset plot (Figure 6). This is the limit speed case for the highest thrust condition. Although the Mach number remains high on the lower surface for this condition, supersonic flow is now limited to only a few degrees of azimuth near 0.107c. Two disturbances in the blade pressures at the end of the third quadrant and the beginning of the fourth are related to the upper surface dynamic stall vortices. The trailing edge pressure separation observed here matches that seen on the upper surface.

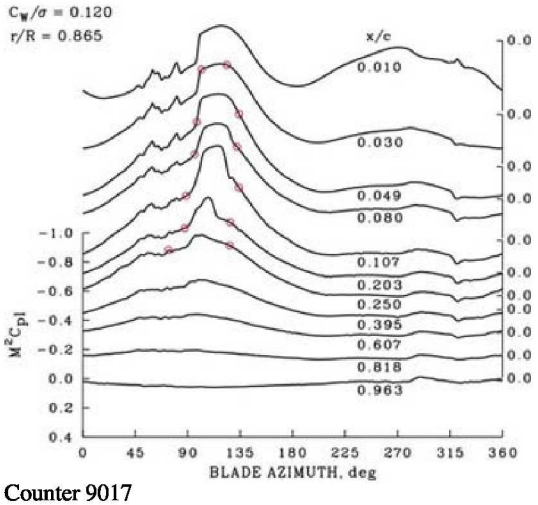

Counter 9017

The lower surface blade pressures are shown in an offset plot (Figure 1), where the offset is in the chordwise pressure transducer location, the leading edge at the top. The data here are for $C_W/\sigma = 0.079$, which is the lowest thrust condition, previously described. The red circles show the critical pressure or sonic line, where the flow locally becomes supersonic on the airfoil. This occurs at end of the first quadrant and in the second as negative lift develops on the airfoil and the supersonic flow on the lower surface extends back to 0.250c. The flow becomes subsonic again as the lift becomes positive in the second quadrant.

The lower surface blade pressures are again shown in an offset plot (Figure 2). The data here are for $C_W/\sigma = 0.089$. The red circles show the critical pressure or sonic line, where the flow locally becomes supersonic on the airfoil. The flow is very similar to the previous case, supersonic flow develops on the lower surface at the end of the first quadrant as negative lift develops on the airfoil section. Then, as positive lift occurs in the second quadrant, the flow becomes subsonic again. Near the airfoil leading edge the supersonic flow develops without the presence of shock waves, but farther back on the airfoil shocks are apparent as they pass over the transducer locations.

The lower surface blade pressures for $C_W/\sigma = 0.101$ are shown in this offset plot (Figure 3). This is the fourth highest rotor thrust case of the six limit-speed conditions. The area of negative airfoil lift, although slightly reduced from the previous case, is still extensive. Otherwise, the development of supersonic flow on this lower surface is very similar to the previous cases.

The lower surface blade pressures at $C_W/\sigma = 0.110$ are shown in this offset plot (Figure 4). This is the limit-speed case for the third highest thrust condition. The extent of negative lift on the airfoil is reduced for this case, but the basic development of supersonic flow on the lower surface is the same as in previous cases. A dynamic stall vortex is observed at this condition on the upper surface, but the effects of this disturbance does not appear on the lower surface.

The lower surface blade pressures at $C_W/\sigma = 0.120$ are shown in this offset plot (Figure 5). This is the limit speed at the second highest thrust condition. There is no longer negative lift on the airfoil for this case, but some supersonic flow is observed on the lower surface and weak shocks occur. A weak disturbance is observed in the fourth quadrant, perhaps associated with the second of the two dynamic stall cycles on the upper surface. Also, separation at the airfoil trailing edge from the first dynamic stall cycle extends here onto the lower surface.

The lower surface blade pressures at $C_W/\sigma = 0.132$ are shown in an offset plot (Figure 6). This is the limit speed case for the highest thrust condition. Although the Mach number remains high on the lower surface for this condition, supersonic flow is now limited to only a few degrees of azimuth near 0.107c. Two disturbances in the blade pressures at the end of the third quadrant and the beginning of the fourth are related to the upper surface dynamic stall vortices. The trailing edge pressure separation observed here matches that seen on the upper surface.

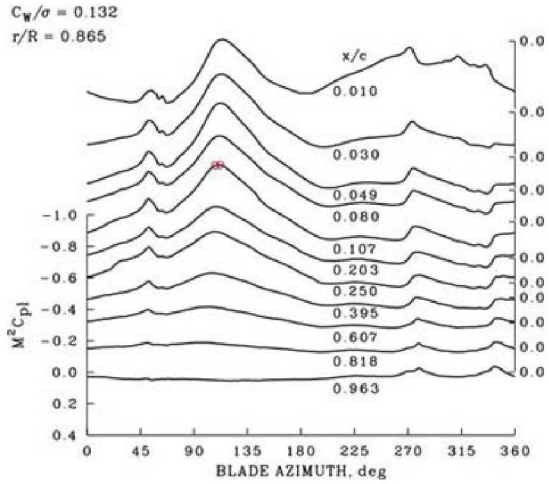

Maneuver loads are dominated by load factor and airspeed, as can be seen by clicking the arrow, primarily because of dynamic stall on the rotor. The comparison here shows the load factor developed in two pull-up maneuvers from the UH-60A Airloads Program: a 2.06g maneuver at 100 kts (Counter 8927) and a 2.12g maneuver at 139 kts (Counter 11029). For comparison, a 2.45g maneuver at 123 kts is shown from the AACT program (Washuta and Stocker, 1986). This latter maneuver was one of the most severe encountered during air-to-air combat tests of a UH-60A. In combat, the highest load factors are generally obtained at lower speeds where there is more excess power.

The alternating pitch-link loads (Figure 2) are most strongly affected by airspeed. The pitch-link loads for Counter 11029, at 139 kts and 2.12g, are significantly higher than those encountered in the AACT test at 2.45g and 123 kts. The loads for Counter 8927, at 100 kts and 2.06g, are not much higher than the maximum level flight loads, indicating that little stall occurs on the rotor for this condition.

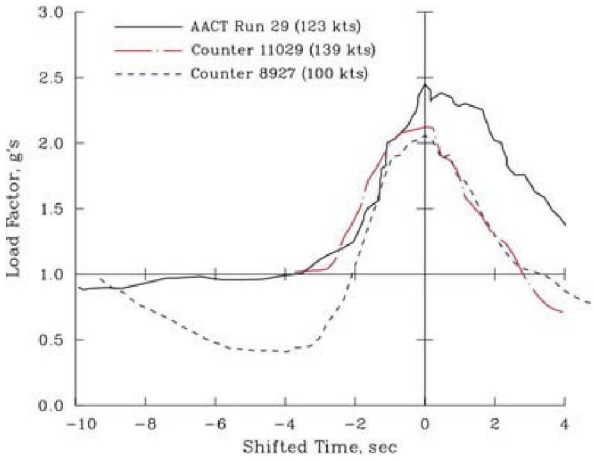

Maneuver loads are dominated by load factor and airspeed, as can be seen by clicking the arrow, primarily because of dynamic stall on the rotor. The comparison here shows the load factor developed in two pull-up maneuvers from the UH-60A Airloads Program: a 2.06g maneuver at 100 kts (Counter 8927) and a 2.12g maneuver at 139 kts (Counter 11029). For comparison, a 2.45g maneuver at 123 kts is shown from the AACT program (Washuta and Stocker, 1986). This latter maneuver was one of the most severe encountered during air-to-air combat tests of a UH-60A. In combat, the highest load factors are generally obtained at lower speeds where there is more excess power.

The alternating pitch-link loads (Figure 2) are most strongly affected by airspeed. The pitch-link loads for Counter 11029, at 139 kts and 2.12g, are significantly higher than those encountered in the AACT test at 2.45g and 123 kts. The loads for Counter 8927, at 100 kts and 2.06g, are not much higher than the maximum level flight loads, indicating that little stall occurs on the rotor for this condition.

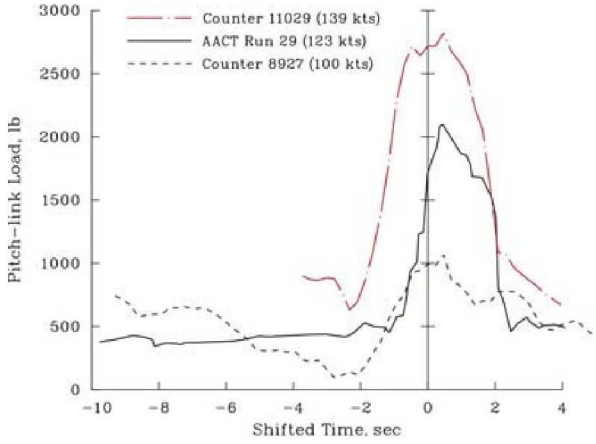

Maneuvers can be included with steady flight cases when load factor is used to multiply the weight coefficient, as shown on the ordinate of the figure. This figure shows the level flight cases from the airspeed sweeps discussed previously and two maneuver cases. Counter 9017 is a steady level flight condition with severe dynamic stall, which has already been introduced. The first maneuver is the UTTAS pull-up, which starts at the maximum level flight airspeed, the aircraft then slowing as load factor increases. The second maneuver is a diving turn in which case both high load factor and high airspeeds are obtained in a dive. These three cases are examined in detail.

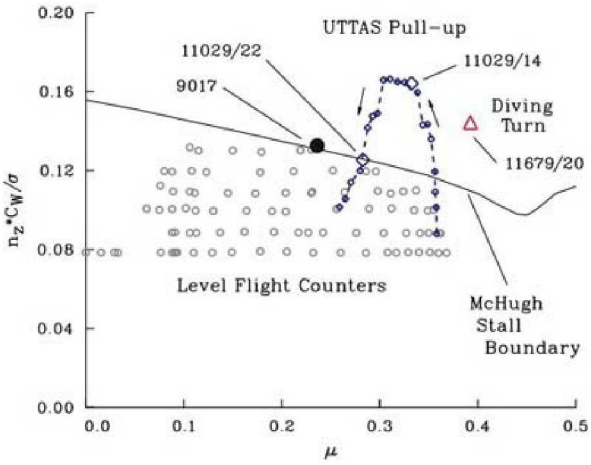

Measured aerodynamic pitching moments are shown in an offset plot for Counter 9017 where the offset is the radial station; the blade tip is at the top of the figure and the root at the bottom. The blade azimuth reference has been shifted by 135 deg., so the entire sequence of stall cycles can be more readily seen. Two dynamic stall cycles are seen at each radius from 0.775R to 0.92R, and one cycle (possibly two) is also seen at 0.965R. The first dynamic stall cycle starts inboard and is delayed to later azimuths as one moves out the blade. But the second cycle occurs simultaneously at all radii. The dynamic stall vortex sequence is dependent on both aerodynamics and structural response.

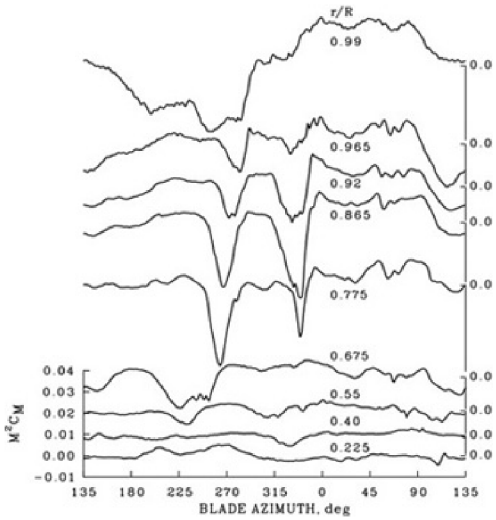

Counter 9017

Measured normal force is shown in an offset plot where the offset is in the radial station; the blade tip is at the top of the figure. The blade azimuth reference has been shifted by 135 deg., so the entire sequence of stall cycles can be seen. The stall cycles are less apparent in the normal force than in the pitching moment. But it is evident that the first stall cycle starts inboard and occurs at later azimuths as one moves towards the tip, whereas the second cycle occurs nearly simultaneously. The inception of the first dynamic stall cycle is largely caused by aerodynamics. But subsequent stall cycles also depend upon the blade and control system aeroelastic response.

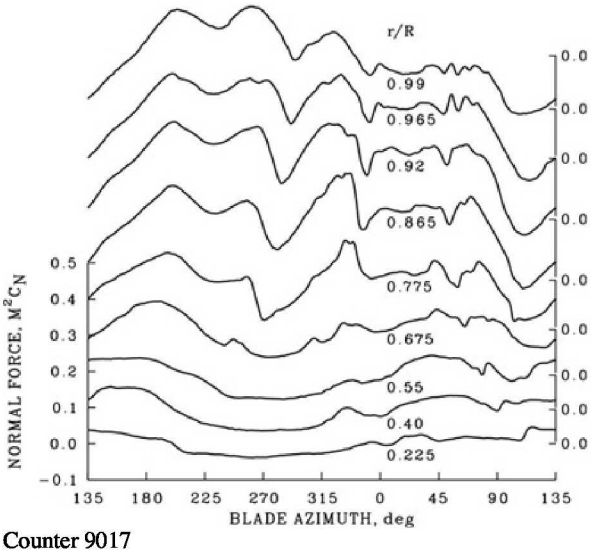

Counter 9017

Dynamic stall is characterized by the formation of a stall vortex near the airfoil leading edge, the axis of the vortex roughly parallel to the blade. During the dynamic stall process, the vortex is shed, passes along the top of the airfoil, and then leaves the blade at the airfoil's trailing edge. The stall vortex is sufficiently strong to cause suction on the airfoil's upper surface. This is evidenced in the two dynamic stall cycles here as a negative moment as the vortex passes the quarter chord (moment stall or "MS") and moment recovery once the vortex leaves the trailing edge. The normal force is roughly constant until the vortex leaves the airfoil trailing edge (lift stall or "LS"), in this case at about 265° and 345°.

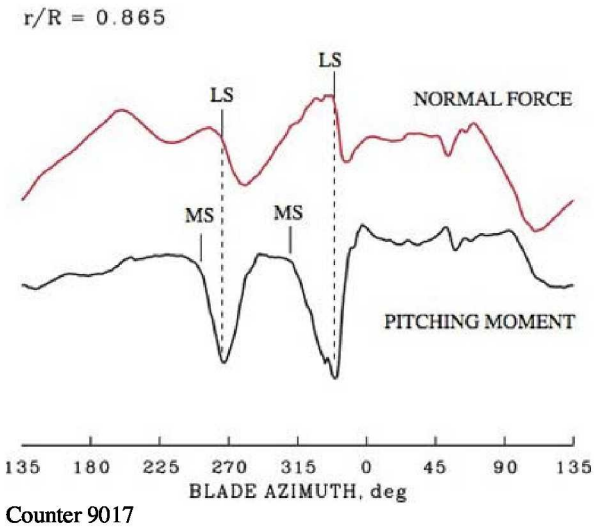

Counter 9017

Under normal flight conditions, the trailing edge pressure shows only a slight 1/rev variation around the azimuth. But, in dynamic stall, as the stall vortex approaches the airfoil's trailing edge, the boundary layer separates. This is clearly seen in the pressure transducer measurements at 0.963c, as shown here. Two dynamic stall cycles are seen from 0.775R to 0.965R. One cycle is apparent at 0.675R, but the trailing edge pressure near the blade tip is more affected by the blade's own tip vortex than by the stall vortices. Each cycle shows separation followed by reattachment. A disturbance is also observed in the first quadrant, and this may be related to an incipient stall vortex (third cycle).

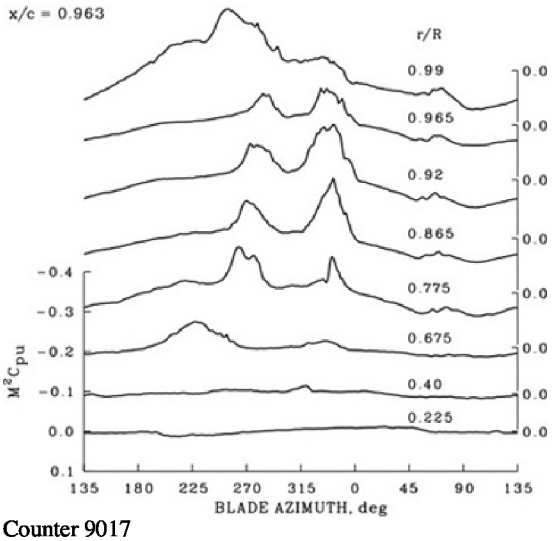

Counter 9017

The various indicators that characterize dynamic stall - that is moment stall, lift stall, and trailing edge separation - can be mapped onto the rotor disk, as shown here. The radial measurement stations are shown as dashed lines (SC1095 airfoil) and dashed-dot lines (SC1094 R8 airfoil). The stall indicators are not seen for every radial station. But as shown here, there is the expected pattern of moment stall occurring first, and then lift stall. Trailing edge separation tends to occur with moment stall or shortly thereafter, but reattachment does not take place until some time after the stall vortex leaves the trailing edge. Note that the first cycle starts inboard on the blade, whereas the second is more or less simultaneous.

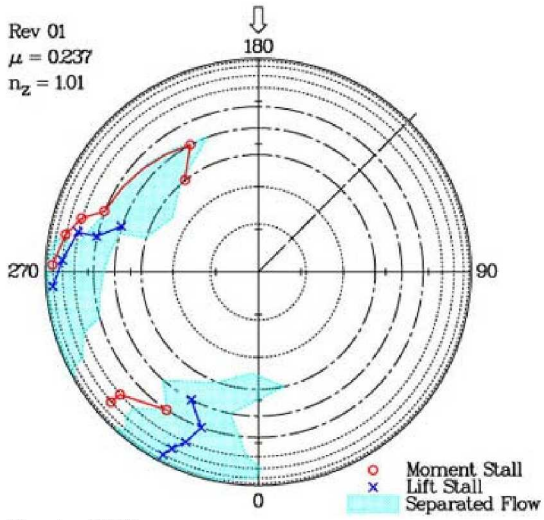

Counter 9017

The upper and lower surface pressures during dynamic stall provide detailed information concerning the formation of the dynamic stall vortices and their movement along the airfoil chord. The upper surface pressures show that there are extensive areas of supersonic (supercritical) flows on the airfoil, both on the advancing side (high Mach number) and on the retreating side (high angle of attack). The formation of the stall vortices is intimately related to these areas of supercritical flow and the stall vortex may occur in supersonic, subsonic, or mixed flows. The modeling of dynamic stall in such flows must be highly sophisticated.

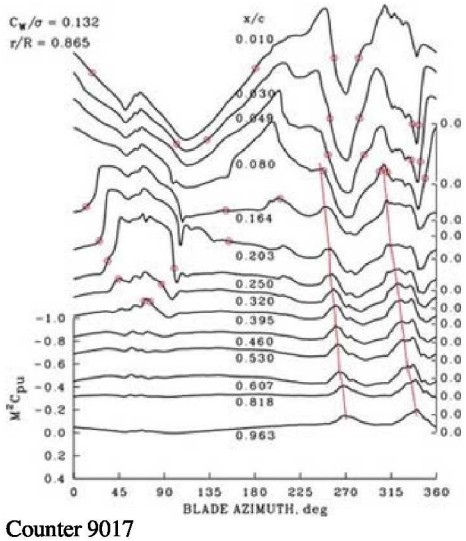

Counter 9017

The various indicators of dynamic stall can be combined on an "airfoil map" (Figure 1), that provides more detail than the rotor map shown previously. The first part of this map shows the upper and lower surfaces of the airfoil, where they are spread out, the upper surface trailing edge at the top, the leading edge in the middle, and the lower surface trailing edge at the bottom. Blade azimuth is equivalent to the passage of time and goes from left to right. Shown here, the red circles represent the sonic line (critical C_p^*) and are the same as seen on the upper surface pressure offset plot. The aqua-stippled area represents the extent of supersonic flow on the airfoil surface.

In Figure 2, the airfoil pitching moment is added at the bottom of the airfoil map. Also, lines that represent both moment stall ("MS") and lift stall ("LS") are added to the map.

The dynamic stall positions on the blade are identified by extrema in the pressure distributions, and are added to the airfoil map in Figure 3. In some cases there are multiple symbols for a transducer, reflecting ambiguity in the transducer time history. A polynomial is fitted to the extrema on the map, and this indicates the passage of the dynamic stall vortex. The Mach number when the stall vortex passes 0.5c is shown at the top of the figure, and just below are bars that indicate the expected vortex convection duration. For this counter, there are two full dynamic stall cycles, but it appears that an incipient stall cycle is also recorded in the first quadrant.

The upper surface trailing edge pressure is added at the top and this completes the airfoil map in Figure 4. A reference case trailing edge pressure is subtracted from the stall case to makes the boundary layer separation more apparent. Under attached flow conditions, then, the trailing edge pressure is approximately zero. The trailing edge pressure starts to separate as the vortex moves down the airfoil and the flow remains separated for a short while after the vortex has left the trailing edge. No separation is apparent in the first quadrant, where there is an incipient dynamic stall vortex.

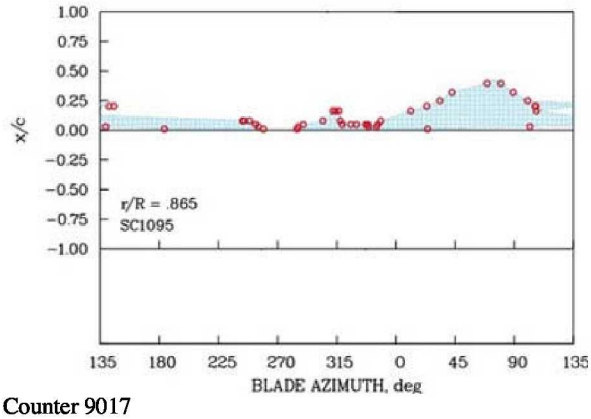

Counter 9017

The various indicators of dynamic stall can be combined on an "airfoil map" (Figure 1), that provides more detail than the rotor map shown previously. The first part of this map shows the upper and lower surfaces of the airfoil, where they are spread out, the upper surface trailing edge at the top, the leading edge in the middle, and the lower surface trailing edge at the bottom. Blade azimuth is equivalent to the passage of time and goes from left to right. Shown here, the red circles represent the sonic line (critical C_p^*) and are the same as seen on the upper surface pressure offset plot. The aqua-stippled area represents the extent of supersonic flow on the airfoil surface.

In Figure 2, the airfoil pitching moment is added at the bottom of the airfoil map. Also, lines that represent both moment stall ("MS") and lift stall ("LS") are added to the map.

The dynamic stall positions on the blade are identified by extrema in the pressure distributions, and are added to the airfoil map in Figure 3. In some cases there are multiple symbols for a transducer, reflecting ambiguity in the transducer time history. A polynomial is fitted to the extrema on the map, and this indicates the passage of the dynamic stall vortex. The Mach number when the stall vortex passes 0.5c is shown at the top of the figure, and just below are bars that indicate the expected vortex convection duration. For this counter, there are two full dynamic stall cycles, but it appears that an incipient stall cycle is also recorded in the first quadrant.

The upper surface trailing edge pressure is added at the top and this completes the airfoil map in Figure 4. A reference case trailing edge pressure is subtracted from the stall case to makes the boundary layer separation more apparent. Under attached flow conditions, then, the trailing edge pressure is approximately zero. The trailing edge pressure starts to separate as the vortex moves down the airfoil and the flow remains separated for a short while after the vortex has left the trailing edge. No separation is apparent in the first quadrant, where there is an incipient dynamic stall vortex.

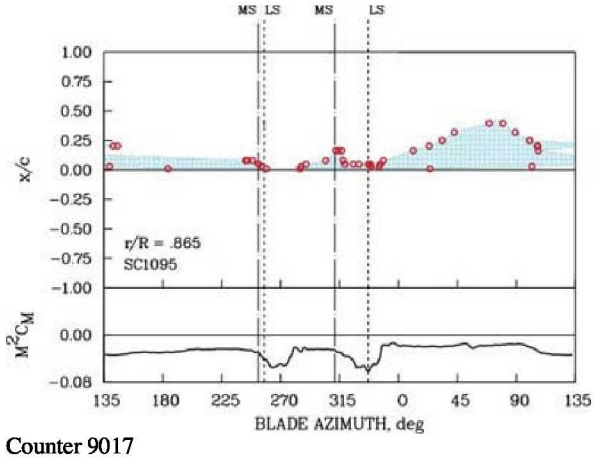

Counter 9017

The various indicators of dynamic stall can be combined on an "airfoil map" (Figure 1), that provides more detail than the rotor map shown previously. The first part of this map shows the upper and lower surfaces of the airfoil, where they are spread out, the upper surface trailing edge at the top, the leading edge in the middle, and the lower surface trailing edge at the bottom. Blade azimuth is equivalent to the passage of time and goes from left to right. Shown here, the red circles represent the sonic line (critical C_p^*) and are the same as seen on the upper surface pressure offset plot. The aqua-stippled area represents the extent of supersonic flow on the airfoil surface.

In Figure 2, the airfoil pitching moment is added at the bottom of the airfoil map. Also, lines that represent both moment stall ("MS") and lift stall ("LS") are added to the map.

The dynamic stall positions on the blade are identified by extrema in the pressure distributions, and are added to the airfoil map in Figure 3. In some cases there are multiple symbols for a transducer, reflecting ambiguity in the transducer time history. A polynomial is fitted to the extrema on the map, and this indicates the passage of the dynamic stall vortex. The Mach number when the stall vortex passes 0.5c is shown at the top of the figure, and just below are bars that indicate the expected vortex convection duration. For this counter, there are two full dynamic stall cycles, but it appears that an incipient stall cycle is also recorded in the first quadrant.

The upper surface trailing edge pressure is added at the top and this completes the airfoil map in Figure 4. A reference case trailing edge pressure is subtracted from the stall case to makes the boundary layer separation more apparent. Under attached flow conditions, then, the trailing edge pressure is approximately zero. The trailing edge pressure starts to separate as the vortex moves down the airfoil and the flow remains separated for a short while after the vortex has left the trailing edge. No separation is apparent in the first quadrant, where there is an incipient dynamic stall vortex.

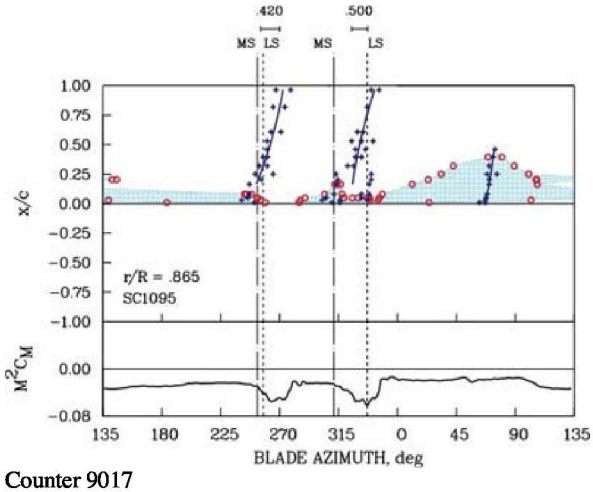

Counter 9017

The various indicators of dynamic stall can be combined on an "airfoil map" (Figure 1), that provides more detail than the rotor map shown previously. The first part of this map shows the upper and lower surfaces of the airfoil, where they are spread out, the upper surface trailing edge at the top, the leading edge in the middle, and the lower surface trailing edge at the bottom. Blade azimuth is equivalent to the passage of time and goes from left to right. Shown here, the red circles represent the sonic line (critical C_p^*) and are the same as seen on the upper surface pressure offset plot. The aqua-stippled area represents the extent of supersonic flow on the airfoil surface.

In Figure 2, the airfoil pitching moment is added at the bottom of the airfoil map. Also, lines that represent both moment stall ("MS") and lift stall ("LS") are added to the map.

The dynamic stall positions on the blade are identified by extrema in the pressure distributions, and are added to the airfoil map in Figure 3. In some cases there are multiple symbols for a transducer, reflecting ambiguity in the transducer time history. A polynomial is fitted to the extrema on the map, and this indicates the passage of the dynamic stall vortex. The Mach number when the stall vortex passes 0.5c is shown at the top of the figure, and just below are bars that indicate the expected vortex convection duration. For this counter, there are two full dynamic stall cycles, but it appears that an incipient stall cycle is also recorded in the first quadrant.

The upper surface trailing edge pressure is added at the top and this completes the airfoil map in Figure 4. A reference case trailing edge pressure is subtracted from the stall case to makes the boundary layer separation more apparent. Under attached flow conditions, then, the trailing edge pressure is approximately zero. The trailing edge pressure starts to separate as the vortex moves down the airfoil and the flow remains separated for a short while after the vortex has left the trailing edge. No separation is apparent in the first quadrant, where there is an incipient dynamic stall vortex.

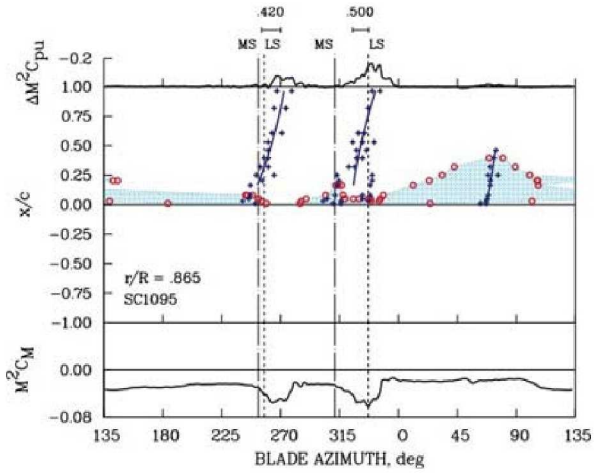

Maneuvers can cause more severe dynamic stall than occurs in level flight as discussed previously. The UTTAS pull-up is a severe maneuver that simulates obstacle avoidance in low-level flight. The maneuver is initiated near the maximum flight speed and the aircraft load factor is rapidly increased to a maximum value. The maneuver is not sustainable because of the excess drag caused by dynamic stall. The aircraft loses speed and eventually load factor and returns to a level flight regime. For the examination in the adjacent tabs, the focus is on Cycle 14 (Rev 14) of the maneuver, which is one of the most severe for dynamic stall.

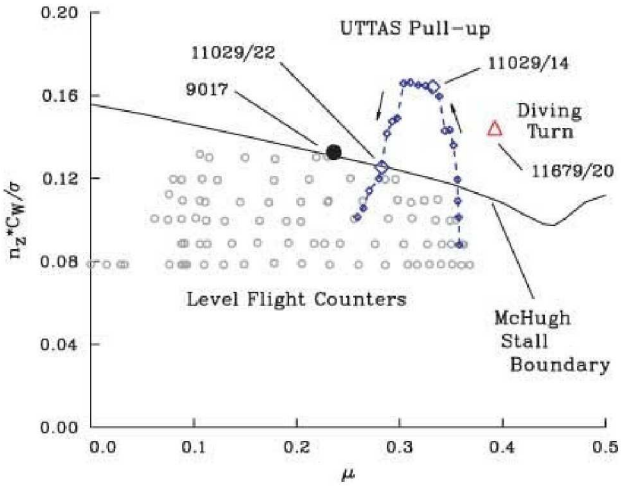

Measured pitching moments are shown in an offset plot for the UTTAS pull-up (Rev 14 of Counter 11029). The offset is the radial station; the blade tip is at the top of the figure and the root at the bottom. The blade azimuth reference has been shifted by 135°, so the entire sequence of stall cycles can be more readily seen. The rotor thrust and airspeed are greater in this maneuver and the stall is more severe than was observed in level flight (Counter 9017). Three dynamic stall cycles are seen at radial stations from 0.775R to 0.92R. Moreover, a single dynamic stall cycle is seen inboard at 0.225R and 0.40R over the nose of the aircraft, probably caused by fuselage-induced flow.

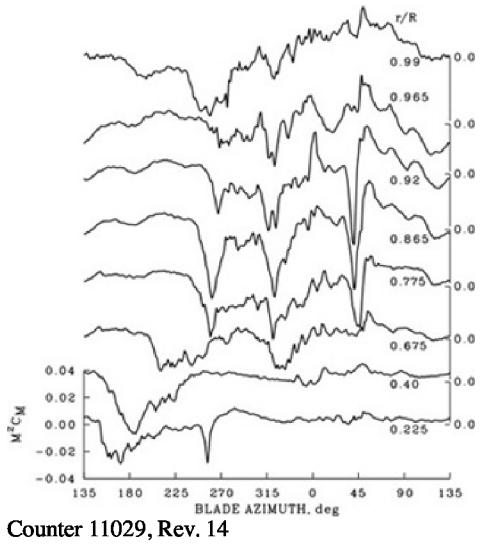

Counter 11029, Rev. 14

Measured normal force is shown in an offset plot for the UTTAS maneuver. The blade azimuth reference has been shifted by 135° so that the entire sequence of stall cycles can be seen. A third stall cycle, which did not occur in the level flight case, is seen in the first quadrant and is stronger than the other cycles because of the extensive supersonic flow on the airfoil.

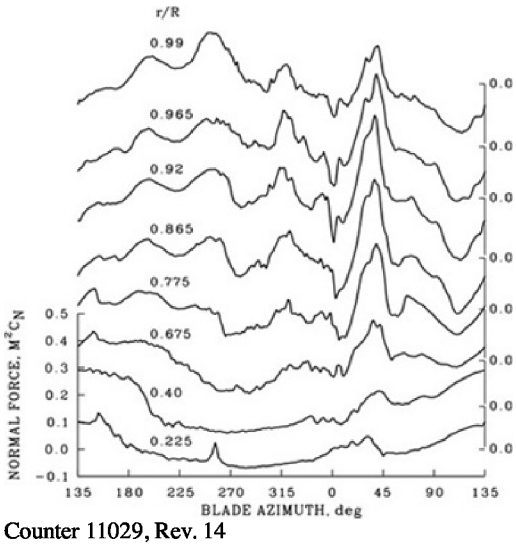

Counter 11029, Rev. 14

As in the level flight case, the boundary layer separates at the trailing edge during the stall cycles. But unlike the level flight case, where the boundary layer reattached before the second stall cycle, the flow remains separated through the first two cycles on the outer blade. Separation is observed from 0.675R to 0.965R for the three dynamic stall cycles, and the flow is also separated for the single stall cycle that occurs inboard on the blade at 0.225R and 0.40R. From the trailing edge separation, it is apparent for the first stall cycle, that the stall is initiated at about 180° inboard on the blade and occurs at about 270° near the blade tip. But for the third stall cycle separation occurs at the same azimuth.

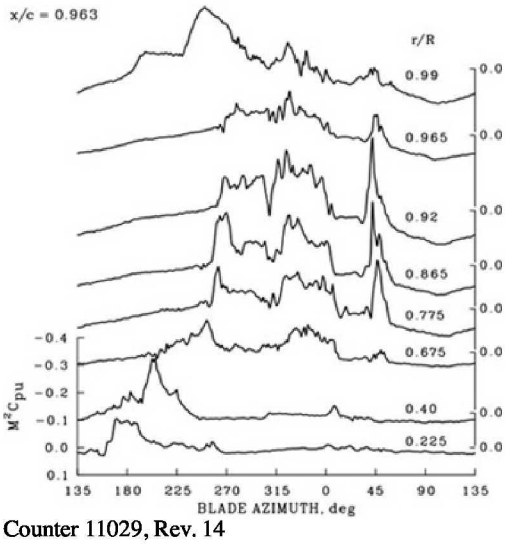

Counter 11029, Rev. 14

The various indicators that characterize dynamic stall—that is moment stall, lift stall, and trailing edge separation—are mapped onto the rotor disk for the UTTAS pull-up maneuver. The stall indicators are not seen for every radial station. But as shown here, there is the expected pattern of moment stall occurring first, and then lift stall. Trailing edge separation tends to occur with moment stall or shortly thereafter, but reattachment does not take place until some time after the stall vortex leaves the trailing edge (and in some cases not before the next cycle). Note that the first cycle occurs inboard first, whereas the second and third cycles are nearly simultaneous.

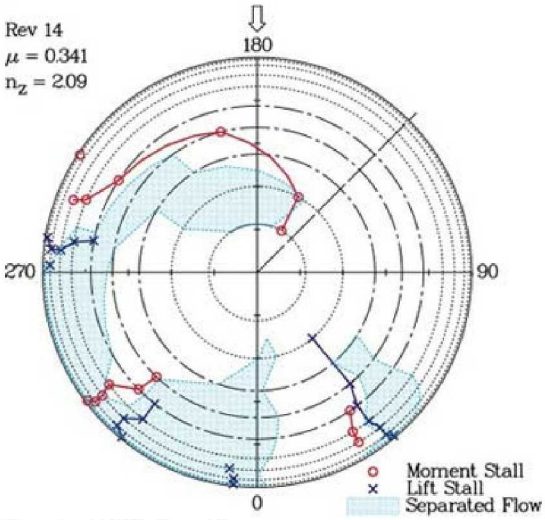

Counter 11029, Rev. 14

The offset plot of upper surface pressures at 0.865R shows the first dynamic stall vortex shed in the third quadrant. The boundary layer separates, and the flow is unsteady. A second dynamic stall vortex forms in the fourth quadrant before the boundary layer reattaches. Following the second cycle, the flow reattaches at the rear of the disk, and the flow becomes supersonic in the first quadrant. A third dynamic stall vortex is shed within the supersonic flow region, and the flow does not become subsonic until aft of 0.607c. The pressure features shown here can be transferred to the airfoil map.

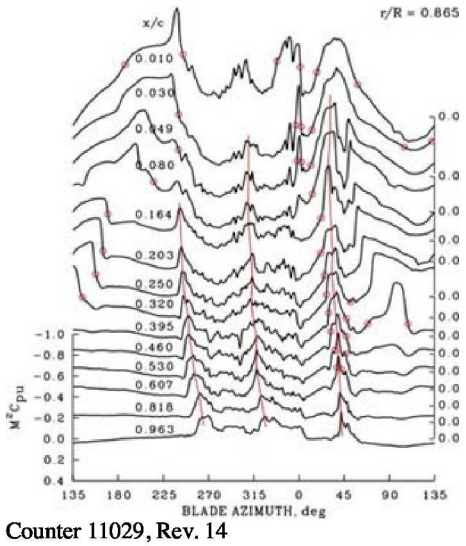

Counter 11029, Rev. 14

This airfoil map of the UTTAS pull-up shows three dynamic stall cycles at $r/R = 0.865$. The first two stall cycles occur on the retreating side of the disk, but the third occurs in the first quadrant of the advancing side. The Mach number for the advancing side dynamic stall cycle is about 0.72, and supersonic flow extends over most of the blade upper surface as the stall vortex forms and is shed. Following the third cycle, pressure extrema suggest an additional structure in the supersonic flow, but it is not identified.

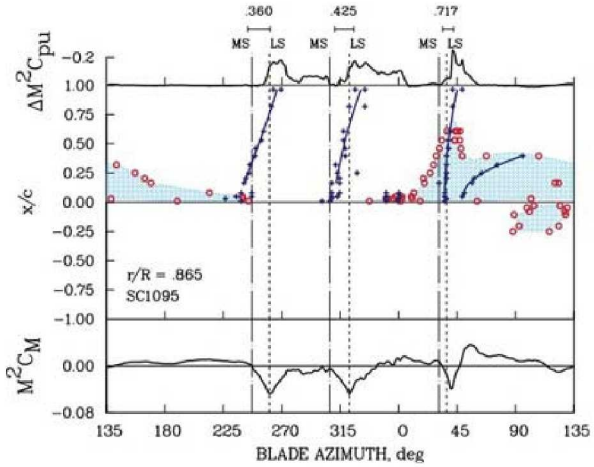

Counter 11029, Rev. 14

A summary of dynamic stall cases from Bousman (1998) is shown on a rotor map. These cases include the level flight and UTTAS pull-up cases discussed previously, plus a second revolution from the UTTAS pull-up and a diving turn condition. These cases represent a wide variety of load factors and airspeeds. Dynamic stall is initiated on the retreating side, generally inboard, and then moves out towards the blade tip. Repetitive stall events occur at intervals that are governed by the aircraft's control system stiffness. The initiation of dynamic stall is probably similar for most rotors. But subsequent cycles will depend upon each design's blade torsion and control system frequencies.

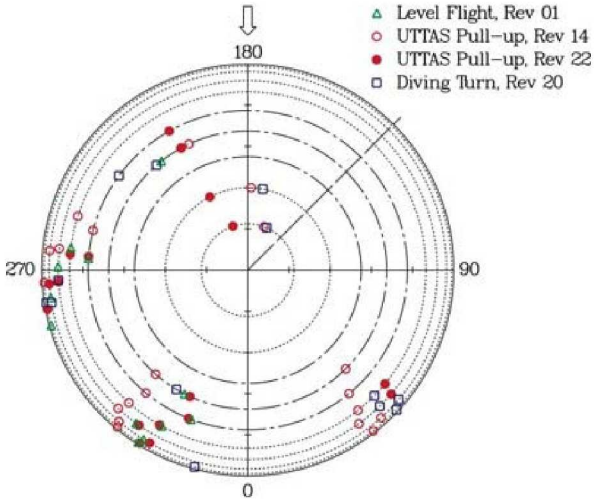

Flight conditions that exceed the dynamic stall boundary cause high loads that may be critical for design as discussed previously. But other conditions may be critical as well, such as the limit dive speed. In this case, loads are caused by supersonic flow on the airfoil rather than dynamic stall.

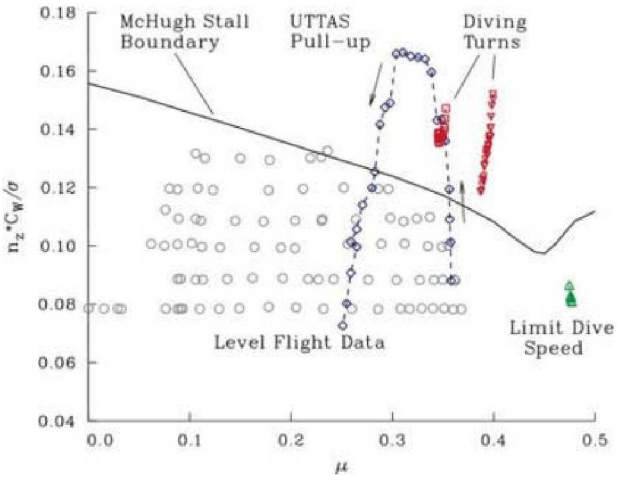

Extensive supersonic flow occurs on the airfoil at the limit dive condition, Counter 11682, as discussed before. At $r/R = 0.965$, as shown here, the lift is negative, and the shocks extend well back on both the upper and lower surfaces of the airfoil as compared to the maximum level flight airspeed case, Counter 8534. The rotor loads in this dive condition, for some components, are greater than occur in dynamic stall. This is especially true for the mid-span flap bending moments (Kufeld and Bousman 1998). Aspects of these high loads are examined in the following tabs.

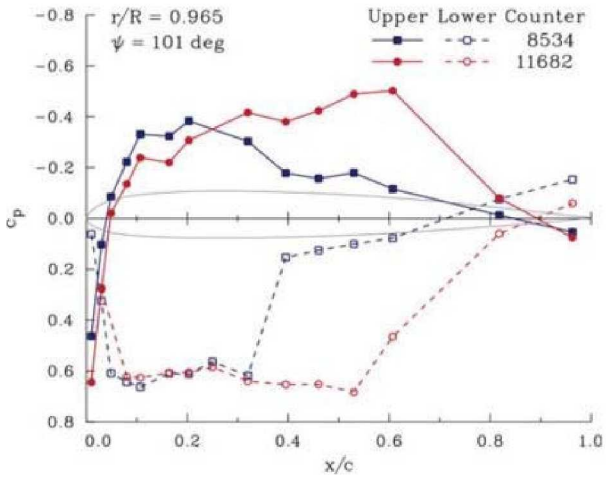

An offset plot of the radial distribution of pitching moment (1–120 harmonics) is shown, where the outboard radial measurement is at the top. The distribution of pitching moment at this dive condition ($\mu = 0.48$) is much changed from the maximum level flight case ($\mu = 0.37$). In level flight the loading outboard is largely dominated by 1/rev negative loading in the second quadrant, whereas here the loading is highly oscillatory and causes high frequency pitch-link loads. The source of these loads is the motion of the shocks on the upper and lower surfaces and is discussed further in these tabs. Inboard, high loading is also observed, caused by the lift offset in reversed flow.

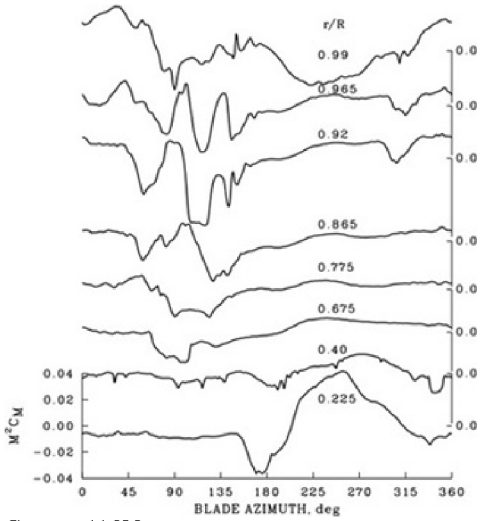

Counter 11682

An offset plot of the radial distribution of normal force (0–120 harmonics) is shown, where the outboard radial measurement is at the top. The distribution of normal force at this dive condition ($\mu = 0.48$) is somewhat changed from the maximum level flight case ($\mu = 0.37$). In both cases, there is negative loading in the second quadrant. In the dive condition, the region of negative loading extends farther inboard and over a larger range in azimuth. The loads are also more oscillatory because of shock motions. Inboard, the region of negative lift associated with reverse flow is also more extensive.

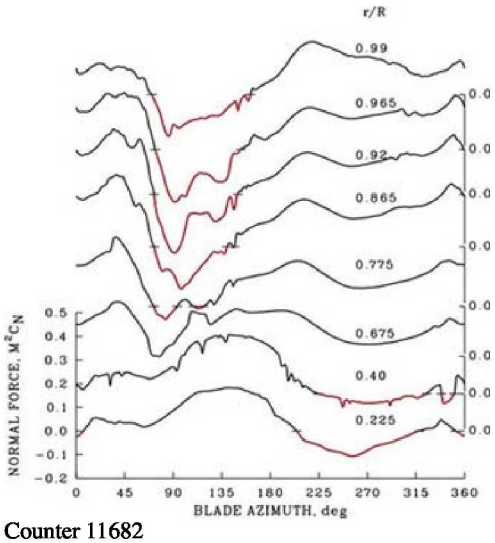

Counter 11682

An offset plot of the chordwise distribution of the upper surface pressures at $r/R = 0.92$ (0–120 harmonics) is shown in Figure 1, the leading edge measurement at the top. Red open symbols show the locations of the sonic line, which mark an extensive region of supersonic in the first two quadrants over the forward portion of the airfoil and extending as far back as 0.818c for some azimuths. A red line traces a weak dynamic stall vortex in the fourth quadrant. This stall vortex appears to be formed near the leading edge, but the trace disappears rearward of 0.607c, and no trailing edge separation is observed. This weak vortex barely affects the airfoil section's pitching moments.

An offset plot of the chordwise distribution of the lower surface pressure at 0.92R (0–120 harmonics) is shown as Figure 2, the leading edge measurement at the top. Red open symbols show the location of the sonic line. As negative lift develops at the end of the first quadrant, the flow on the lower surface becomes strongly supersonic, extending as far back as 0.607c.

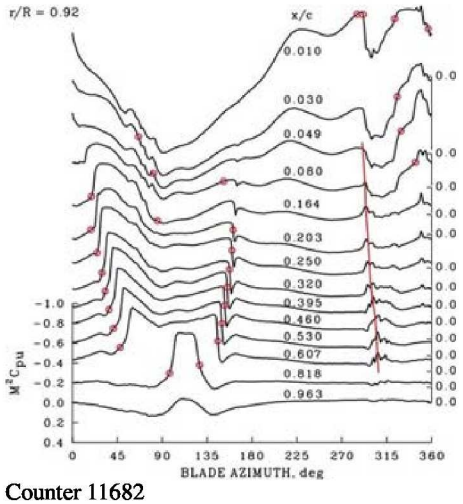

Counter 11682

An offset plot of the chordwise distribution of the upper surface pressures at $r/R = 0.92$ (0–120 harmonics) is shown in Figure 1, the leading edge measurement at the top. Red open symbols show the locations of the sonic line, which mark an extensive region of supersonic in the first two quadrants over the forward portion of the airfoil and extending as far back as 0.818c for some azimuths. A red line traces a weak dynamic stall vortex in the fourth quadrant. This stall vortex appears to be formed near the leading edge, but the trace disappears rearward of 0.607c, and no trailing edge separation is observed. This weak vortex barely affects the airfoil section's pitching moments.

An offset plot of the chordwise distribution of the lower surface pressure at 0.92R (0–120 harmonics) is shown as Figure 2, the leading edge measurement at the top. Red open symbols show the location of the sonic line. As negative lift develops at the end of the first quadrant, the flow on the lower surface becomes strongly supersonic, extending as far back as 0.607c.

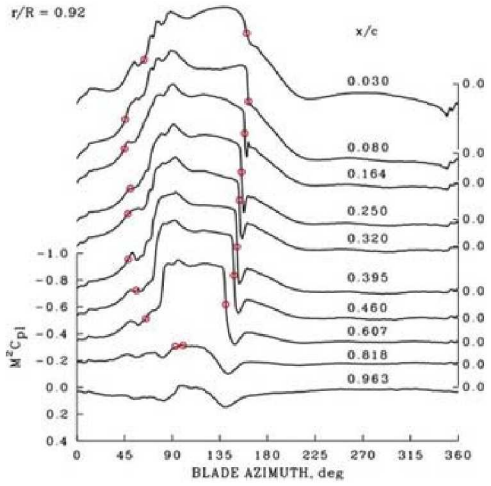

Pressure measurements on the upper and lower surfaces are compared at chordwise stations aft of the quarter chord. Overlaid on this plot (Figure 1) with a thickened dotted line is the critical pressure, or sonic line, that separates subsonic and supersonic flows on the airfoil. The general pattern here at 0.32c occurs at least to 0.607c. In the first quadrant, the flow on the upper surface is strongly supersonic, but becomes less so as the lift becomes negative at 80 or 90°. The supersonic flow on the lower surface then becomes important until the shocks move forward past these transducers at about 150°. The differences in upper and lower surface pressures strongly affect the pitching moment.

Figure 2. The pattern of upper and lower surface pressures is little changed at 0.395c from 0.320c, although the azimuthal range of supersonic flow becomes more narrow towards the rear of the airfoil. Again, the supersonic flow on the upper surface in the first quadrant contributes to a negative pitching moment, whereas the supersonic flow on the lower surface starting at 80 or 90° contributes to a positive pitching moment. Note the passage of the dynamic stall vortex in the fourth quadrant (also apparent at 0.320c).

Figure 3. The pattern of upper and lower surface pressures narrows slightly at 0.46c. As before, the supersonic flow on the upper surface in the first quadrant contributes to a negative pitching moment, whereas the supersonic flow on the lower surface starting at 80 or 90° contributes to a positive pitching moment. The passage of the dynamic stall vortex in the fourth quadrant is little changed.

Figure 4. The pattern of upper and lower surface pressures narrows at 0.607c. As before, the supersonic flow on the upper surface in the first quadrant contributes to a negative pitching moment, whereas the supersonic flow on the lower surface starting at 80 or 90° contributes to a positive pitching moment, but the difference is no longer so great. The trace of the dynamic stall vortex in the fourth quadrant is considerably reduced from that seen at 0.46c.

Figure 5. The supersonic flow on the lower surface terminates between 0.607c and 0.818c, leaving only an azimuthally narrow area of supersonic flow on the upper surface, which causes negative pitching moments. Only a hint of the dynamic stall vortex is observed, as it has moved off the airfoil or dissipated.

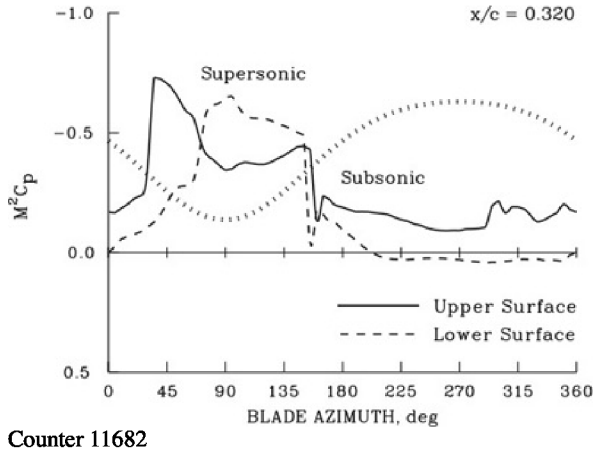

Counter 11682

Pressure measurements on the upper and lower surfaces are compared at chordwise stations aft of the quarter chord. Overlaid on this plot (Figure 1) with a thickened dotted line is the critical pressure, or sonic line, that separates subsonic and supersonic flows on the airfoil. The general pattern here at 0.32c occurs at least to 0.607c. In the first quadrant, the flow on the upper surface is strongly supersonic, but becomes less so as the lift becomes negative at 80 or 90°. The supersonic flow on the lower surface then becomes important until the shocks move forward past these transducers at about 150°. The differences in upper and lower surface pressures strongly affect the pitching moment.

Figure 2. The pattern of upper and lower surface pressures is little changed at 0.395c from 0.320c, although the azimuthal range of supersonic flow becomes more narrow towards the rear of the airfoil. Again, the supersonic flow on the upper surface in the first quadrant contributes to a negative pitching moment, whereas the supersonic flow on the lower surface starting at 80 or 90° contributes to a positive pitching moment. Note the passage of the dynamic stall vortex in the fourth quadrant (also apparent at 0.320c).

Figure 3. The pattern of upper and lower surface pressures narrows slightly at 0.46c. As before, the supersonic flow on the upper surface in the first quadrant contributes to a negative pitching moment, whereas the supersonic flow on the lower surface starting at 80 or 90° contributes to a positive pitching moment. The passage of the dynamic stall vortex in the fourth quadrant is little changed.

Figure 4. The pattern of upper and lower surface pressures narrows at 0.607c. As before, the supersonic flow on the upper surface in the first quadrant contributes to a negative pitching moment, whereas the supersonic flow on the lower surface starting at 80 or 90° contributes to a positive pitching moment, but the difference is no longer so great. The trace of the dynamic stall vortex in the fourth quadrant is considerably reduced from that seen at 0.46c.

Figure 5. The supersonic flow on the lower surface terminates between 0.607c and 0.818c, leaving only an azimuthally narrow area of supersonic flow on the upper surface, which causes negative pitching moments. Only a hint of the dynamic stall vortex is observed, as it has moved off the airfoil or dissipated.

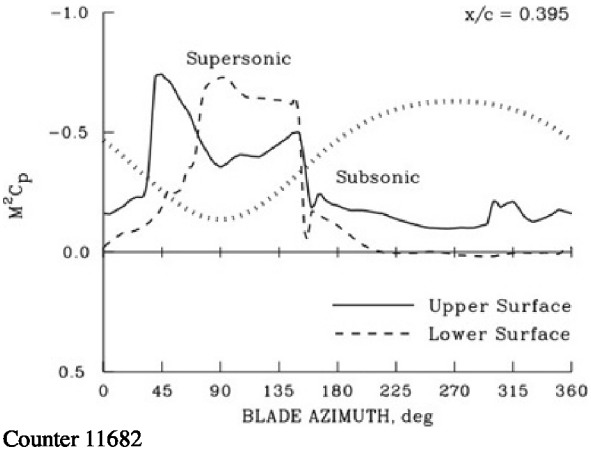

Counter 11682

Pressure measurements on the upper and lower surfaces are compared at chordwise stations aft of the quarter chord. Overlaid on this plot (Figure 1) with a thickened dotted line is the critical pressure, or sonic line, that separates subsonic and supersonic flows on the airfoil. The general pattern here at 0.32c occurs at least to 0.607c. In the first quadrant, the flow on the upper surface is strongly supersonic, but becomes less so as the lift becomes negative at 80 or 90°. The supersonic flow on the lower surface then becomes important until the shocks move forward past these transducers at about 150°. The differences in upper and lower surface pressures strongly affect the pitching moment.

Figure 2. The pattern of upper and lower surface pressures is little changed at 0.395c from 0.320c, although the azimuthal range of supersonic flow becomes more narrow towards the rear of the airfoil. Again, the supersonic flow on the upper surface in the first quadrant contributes to a negative pitching moment, whereas the supersonic flow on the lower surface starting at 80 or 90° contributes to a positive pitching moment. Note the passage of the dynamic stall vortex in the fourth quadrant (also apparent at 0.320c).

Figure 3. The pattern of upper and lower surface pressures narrows slightly at 0.46c. As before, the supersonic flow on the upper surface in the first quadrant contributes to a negative pitching moment, whereas the supersonic flow on the lower surface starting at 80 or 90° contributes to a positive pitching moment. The passage of the dynamic stall vortex in the fourth quadrant is little changed.

Figure 4. The pattern of upper and lower surface pressures narrows at 0.607c. As before, the supersonic flow on the upper surface in the first quadrant contributes to a negative pitching moment, whereas the supersonic flow on the lower surface starting at 80 or 90° contributes to a positive pitching moment, but the difference is no longer so great. The trace of the dynamic stall vortex in the fourth quadrant is considerably reduced from that seen at 0.46c.

Figure 5. The supersonic flow on the lower surface terminates between 0.607c and 0.818c, leaving only an azimuthally narrow area of supersonic flow on the upper surface, which causes negative pitching moments. Only a hint of the dynamic stall vortex is observed, as it has moved off the airfoil or dissipated.

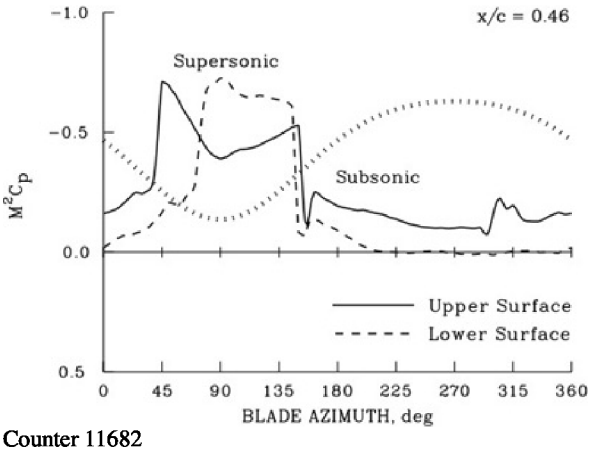

Counter 11682

Pressure measurements on the upper and lower surfaces are compared at chordwise stations aft of the quarter chord. Overlaid on this plot (Figure 1) with a thickened dotted line is the critical pressure, or sonic line, that separates subsonic and supersonic flows on the airfoil. The general pattern here at 0.32c occurs at least to 0.607c. In the first quadrant, the flow on the upper surface is strongly supersonic, but becomes less so as the lift becomes negative at 80 or 90°. The supersonic flow on the lower surface then becomes important until the shocks move forward past these transducers at about 150°. The differences in upper and lower surface pressures strongly affect the pitching moment.

Figure 2. The pattern of upper and lower surface pressures is little changed at 0.395c from 0.320c, although the azimuthal range of supersonic flow becomes more narrow towards the rear of the airfoil. Again, the supersonic flow on the upper surface in the first quadrant contributes to a negative pitching moment, whereas the supersonic flow on the lower surface starting at 80 or 90° contributes to a positive pitching moment. Note the passage of the dynamic stall vortex in the fourth quadrant (also apparent at 0.320c).

Figure 3. The pattern of upper and lower surface pressures narrows slightly at 0.46c. As before, the supersonic flow on the upper surface in the first quadrant contributes to a negative pitching moment, whereas the supersonic flow on the lower surface starting at 80 or 90° contributes to a positive pitching moment. The passage of the dynamic stall vortex in the fourth quadrant is little changed.

Figure 4. The pattern of upper and lower surface pressures narrows at 0.607c. As before, the supersonic flow on the upper surface in the first quadrant contributes to a negative pitching moment, whereas the supersonic flow on the lower surface starting at 80 or 90° contributes to a positive pitching moment, but the difference is no longer so great. The trace of the dynamic stall vortex in the fourth quadrant is considerably reduced from that seen at 0.46c.

Figure 5. The supersonic flow on the lower surface terminates between 0.607c and 0.818c, leaving only an azimuthally narrow area of supersonic flow on the upper surface, which causes negative pitching moments. Only a hint of the dynamic stall vortex is observed, as it has moved off the airfoil or dissipated.

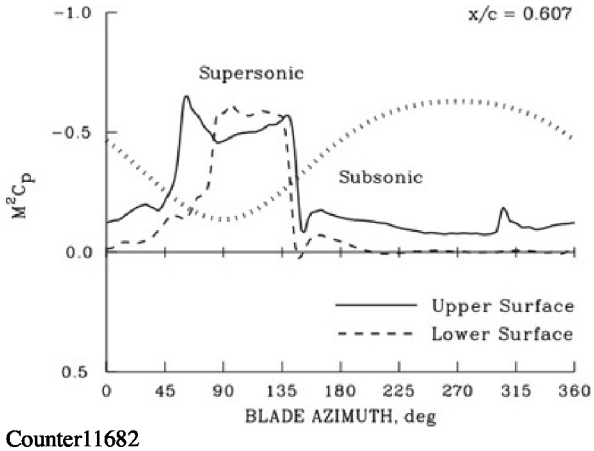

Counter11682

Pressure measurements on the upper and lower surfaces are compared at chordwise stations aft of the quarter chord. Overlaid on this plot (Figure 1) with a thickened dotted line is the critical pressure, or sonic line, that separates subsonic and supersonic flows on the airfoil. The general pattern here at 0.32c occurs at least to 0.607c. In the first quadrant, the flow on the upper surface is strongly supersonic, but becomes less so as the lift becomes negative at 80 or 90°. The supersonic flow on the lower surface then becomes important until the shocks move forward past these transducers at about 150°. The differences in upper and lower surface pressures strongly affect the pitching moment.

Figure 2. The pattern of upper and lower surface pressures is little changed at 0.395c from 0.320c, although the azimuthal range of supersonic flow becomes more narrow towards the rear of the airfoil. Again, the supersonic flow on the upper surface in the first quadrant contributes to a negative pitching moment, whereas the supersonic flow on the lower surface starting at 80 or 90° contributes to a positive pitching moment. Note the passage of the dynamic stall vortex in the fourth quadrant (also apparent at 0.320c).

Figure 3. The pattern of upper and lower surface pressures narrows slightly at 0.46c. As before, the supersonic flow on the upper surface in the first quadrant contributes to a negative pitching moment, whereas the supersonic flow on the lower surface starting at 80 or 90° contributes to a positive pitching moment. The passage of the dynamic stall vortex in the fourth quadrant is little changed.

Figure 4. The pattern of upper and lower surface pressures narrows at 0.607c. As before, the supersonic flow on the upper surface in the first quadrant contributes to a negative pitching moment, whereas the supersonic flow on the lower surface starting at 80 or 90° contributes to a positive pitching moment, but the difference is no longer so great. The trace of the dynamic stall vortex in the fourth quadrant is considerably reduced from that seen at 0.46c.

Figure 5. The supersonic flow on the lower surface terminates between 0.607c and 0.818c, leaving only an azimuthally narrow area of supersonic flow on the upper surface, which causes negative pitching moments. Only a hint of the dynamic stall vortex is observed, as it has moved off the airfoil or dissipated.

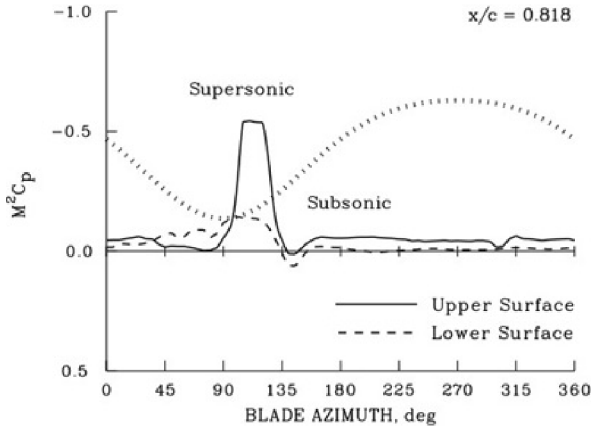

Ground-acoustic testing was performed at the Crows Landing Airfield near Patterson, California (Bousman and Kufeld 2005). A microphone array was laid out at the intersection of two runways and the UH-60A flew ascents, descents, and level flights over the array. The aircraft was continuously followed with a laser tracking system and the standard Instrumented Landing System (ILS) in the cockpit was modified to provide real-time flight guidance to the pilots. The data acquired on the aircraft are a part of the UH-60A Airloads Program database, but the acoustic data are separate. The ground-acoustic testing is described in subsequent panels.

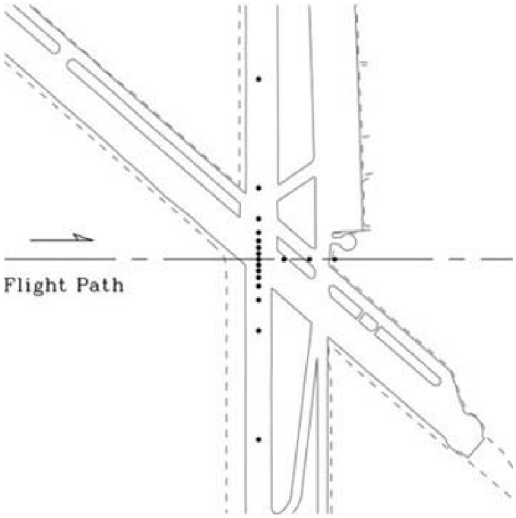

Approximately 86 climb, level flight, and descent counters (including repeat points) were obtained during ground-acoustic testing. The laser tracker was used to provide the flight path angle measurements, whereas the onboard airspeed system was used to define the advance ratio. For the most part, data were obtained from $\mu = 0.10$ to 0.25 and flight path angles from about -15° (descent) to +15° (climb). The effect of the changes in flight path angle was to change the relative positions of the blade tip vortices relative to the rotor blades. In descent, the vortex wake lined up closely to the rotor disk plane, whereas in climb, the vortex wake was well below the disk plane.

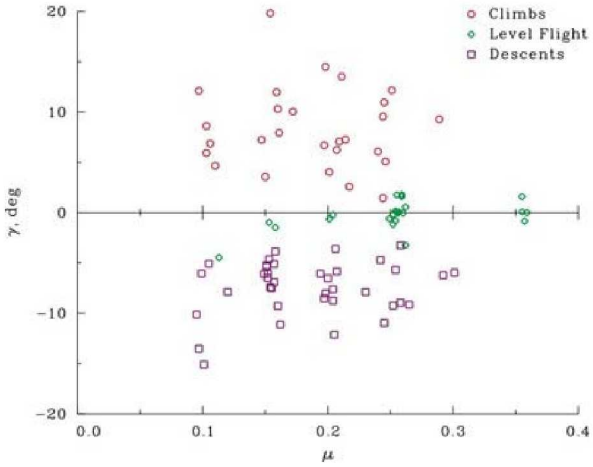

The normal force (1–120 harmonics) at eight radial stations is shown as an offset plot (Figure 1). The blade loads near the rotor tip are at the top and the loads at the blade root are at the bottom. The flight path angle, γ, is 19.8°, a climb rate that is much steeper than a typical climb out for a helicopter. The advance ratio is about 0.15, which is a typical speed for this helicopter, either for an approach to landing or while climbing out.

Figure 2. The character of the normal force is generally smooth, since the rotor wake is well below the blades at this climb rate and there is no significant interaction with the wake. See the panels in the next tab for the high-frequency content.

Figure 3. The climb angle in this case is $\gamma = 4.0°$, which is close to normal for helicopter operations. At this advance ratio ($\mu = 0.15$), there is significant blade loading from the two disk vortices. In addition, high frequency, low amplitude oscillations are seen at some of these radial stations, which are the result of close interactions of the blade with individual tip vortices from prior blades.

Figure 4. The flight path angle is -0.4°, which is essentially level flight. Loading from the disk vortices is observed outboard on the blade. In addition, loading from individual vortices is particularly noticeable at $r/R = 0.865$ on the advancing side.

Figure 5. The flight path angle is -4.8°, which is a moderate descent, close to the glide path angle used by fixed-wing aircraft in an approach to an airport. The low frequency disk vortex loading on the advancing and retreating sides is similar to the previous panels, but now high frequency loading caused by interactions with individual tip vortices is more noticeable. These interactions appear to be strongest in the first and fourth quadrants.

Figure 6. The flight path angle in this case is -6.3°, a fairly steep descent. The low frequency loading caused by the disk vortices is slightly reduced from the previous panel, but the loading from individual blade tip vortices is more apparent in the first and fourth quadrants. Moreover, this BVI loading is seen on both sides of the rotor disk nearly to the blade root.

Figure 7. The flight path angle is -11.7°, which is a steep descent. Both the disk vortex loading and the BVI loading from individual tip vortices is reduced from the prior panel. Moreover, the vortex loading is occurring closer to the rear of the disk, that is the vortices appear sooner in the first quadrant and later in the fourth quadrant.

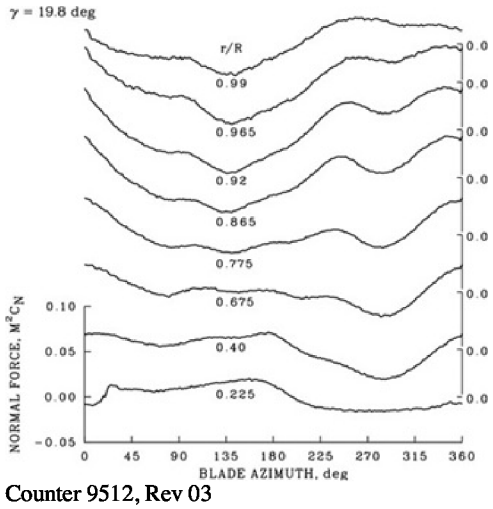

Counter 9512, Rev 03

The normal force (1–120 harmonics) at eight radial stations is shown as an offset plot (Figure 1). The blade loads near the rotor tip are at the top and the loads at the blade root are at the bottom. The flight path angle, γ, is 19.8°, a climb rate that is much steeper than a typical climb out for a helicopter. The advance ratio is about 0.15, which is a typical speed for this helicopter, either for an approach to landing or while climbing out.

Figure 2. The character of the normal force is generally smooth, since the rotor wake is well below the blades at this climb rate and there is no significant interaction with the wake. See the panels in the next tab for the high-frequency content.

Figure 3. The climb angle in this case is $\gamma = 4.0°$, which is close to normal for helicopter operations. At this advance ratio ($\mu = 0.15$), there is significant blade loading from the two disk vortices. In addition, high frequency, low amplitude oscillations are seen at some of these radial stations, which are the result of close interactions of the blade with individual tip vortices from prior blades.

Figure 4. The flight path angle is -0.4°, which is essentially level flight. Loading from the disk vortices is observed outboard on the blade. In addition, loading from individual vortices is particularly noticeable at $r/R = 0.865$ on the advancing side.

Figure 5. The flight path angle is -4.8°, which is a moderate descent, close to the glide path angle used by fixed-wing aircraft in an approach to an airport. The low frequency disk vortex loading on the advancing and retreating sides is similar to the previous panels, but now high frequency loading caused by interactions with individual tip vortices is more noticeable. These interactions appear to be strongest in the first and fourth quadrants.

Figure 6. The flight path angle in this case is -6.3°, a fairly steep descent. The low frequency loading caused by the disk vortices is slightly reduced from the previous panel, but the loading from individual blade tip vortices is more apparent in the first and fourth quadrants. Moreover, this BVI loading is seen on both sides of the rotor disk nearly to the blade root.

Figure 7. The flight path angle is -11.7°, which is a steep descent. Both the disk vortex loading and the BVI loading from individual tip vortices is reduced from the prior panel. Moreover, the vortex loading is occurring closer to the rear of the disk, that is the vortices appear sooner in the first quadrant and later in the fourth quadrant.

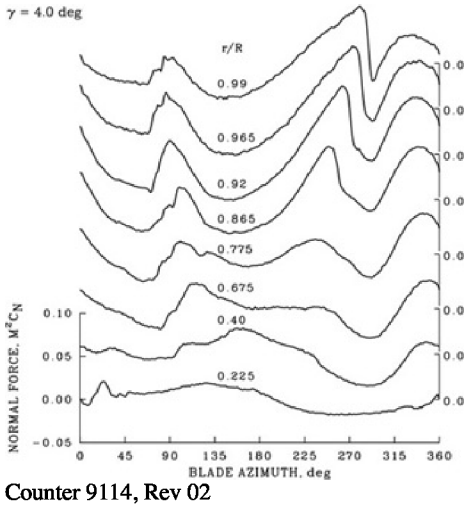

Counter 9114, Rev 02

The normal force (1–120 harmonics) at eight radial stations is shown as an offset plot (Figure 1). The blade loads near the rotor tip are at the top and the loads at the blade root are at the bottom. The flight path angle, γ, is 19.8°, a climb rate that is much steeper than a typical climb out for a helicopter. The advance ratio is about 0.15, which is a typical speed for this helicopter, either for an approach to landing or while climbing out.

Figure 2. The character of the normal force is generally smooth, since the rotor wake is well below the blades at this climb rate and there is no significant interaction with the wake. See the panels in the next tab for the high-frequency content.

Figure 3. The climb angle in this case is $\gamma = 4.0°$, which is close to normal for helicopter operations. At this advance ratio ($\mu = 0.15$), there is significant blade loading from the two disk vortices. In addition, high frequency, low amplitude oscillations are seen at some of these radial stations, which are the result of close interactions of the blade with individual tip vortices from prior blades.

Figure 4. The flight path angle is -0.4°, which is essentially level flight. Loading from the disk vortices is observed outboard on the blade. In addition, loading from individual vortices is particularly noticeable at $r/R = 0.865$ on the advancing side.

Figure 5. The flight path angle is -4.8°, which is a moderate descent, close to the glide path angle used by fixed-wing aircraft in an approach to an airport. The low frequency disk vortex loading on the advancing and retreating sides is similar to the previous panels, but now high frequency loading caused by interactions with individual tip vortices is more noticeable. These interactions appear to be strongest in the first and fourth quadrants.

Figure 6. The flight path angle in this case is -6.3°, a fairly steep descent. The low frequency loading caused by the disk vortices is slightly reduced from the previous panel, but the loading from individual blade tip vortices is more apparent in the first and fourth quadrants. Moreover, this BVI loading is seen on both sides of the rotor disk nearly to the blade root.

Figure 7. The flight path angle is -11.7°, which is a steep descent. Both the disk vortex loading and the BVI loading from individual tip vortices is reduced from the prior panel. Moreover, the vortex loading is occurring closer to the rear of the disk, that is the vortices appear sooner in the first quadrant and later in the fourth quadrant.

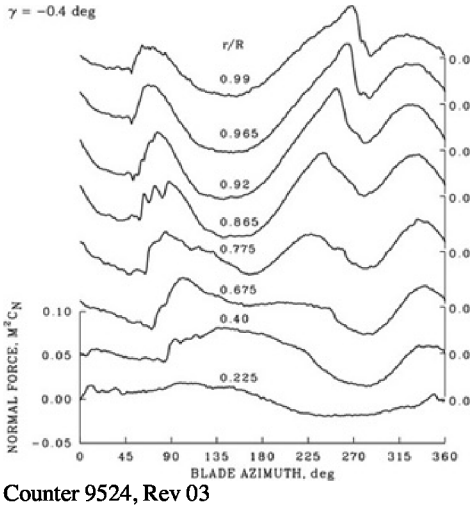

Counter 9524, Rev 03

The normal force (1–120 harmonics) at eight radial stations is shown as an offset plot (Figure 1). The blade loads near the rotor tip are at the top and the loads at the blade root are at the bottom. The flight path angle, γ, is 19.8°, a climb rate that is much steeper than a typical climb out for a helicopter. The advance ratio is about 0.15, which is a typical speed for this helicopter, either for an approach to landing or while climbing out.

Figure 2. The character of the normal force is generally smooth, since the rotor wake is well below the blades at this climb rate and there is no significant interaction with the wake. See the panels in the next tab for the high-frequency content.

Figure 3. The climb angle in this case is $\gamma = 4.0°$, which is close to normal for helicopter operations. At this advance ratio ($\mu = 0.15$), there is significant blade loading from the two disk vortices. In addition, high frequency, low amplitude oscillations are seen at some of these radial stations, which are the result of close interactions of the blade with individual tip vortices from prior blades.

Figure 4. The flight path angle is -0.4°, which is essentially level flight. Loading from the disk vortices is observed outboard on the blade. In addition, loading from individual vortices is particularly noticeable at $r/R = 0.865$ on the advancing side.

Figure 5. The flight path angle is -4.8°, which is a moderate descent, close to the glide path angle used by fixed-wing aircraft in an approach to an airport. The low frequency disk vortex loading on the advancing and retreating sides is similar to the previous panels, but now high frequency loading caused by interactions with individual tip vortices is more noticeable. These interactions appear to be strongest in the first and fourth quadrants.

Figure 6. The flight path angle in this case is -6.3°, a fairly steep descent. The low frequency loading caused by the disk vortices is slightly reduced from the previous panel, but the loading from individual blade tip vortices is more apparent in the first and fourth quadrants. Moreover, this BVI loading is seen on both sides of the rotor disk nearly to the blade root.

Figure 7. The flight path angle is -11.7°, which is a steep descent. Both the disk vortex loading and the BVI loading from individual tip vortices is reduced from the prior panel. Moreover, the vortex loading is occurring closer to the rear of the disk, that is the vortices appear sooner in the first quadrant and later in the fourth quadrant.

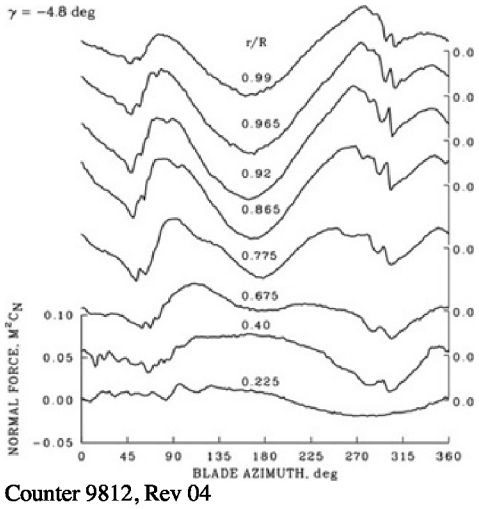

Counter 9812, Rev 04

The normal force (1–120 harmonics) at eight radial stations is shown as an offset plot (Figure 1). The blade loads near the rotor tip are at the top and the loads at the blade root are at the bottom. The flight path angle, γ, is 19.8°, a climb rate that is much steeper than a typical climb out for a helicopter. The advance ratio is about 0.15, which is a typical speed for this helicopter, either for an approach to landing or while climbing out.

Figure 2. The character of the normal force is generally smooth, since the rotor wake is well below the blades at this climb rate and there is no significant interaction with the wake. See the panels in the next tab for the high-frequency content.

Figure 3. The climb angle in this case is $\gamma = 4.0°$, which is close to normal for helicopter operations. At this advance ratio ($\mu = 0.15$), there is significant blade loading from the two disk vortices. In addition, high frequency, low amplitude oscillations are seen at some of these radial stations, which are the result of close interactions of the blade with individual tip vortices from prior blades.

Figure 4. The flight path angle is -0.4°, which is essentially level flight. Loading from the disk vortices is observed outboard on the blade. In addition, loading from individual vortices is particularly noticeable at $r/R = 0.865$ on the advancing side.

Figure 5. The flight path angle is -4.8°, which is a moderate descent, close to the glide path angle used by fixed-wing aircraft in an approach to an airport. The low frequency disk vortex loading on the advancing and retreating sides is similar to the previous panels, but now high frequency loading caused by interactions with individual tip vortices is more noticeable. These interactions appear to be strongest in the first and fourth quadrants.

Figure 6. The flight path angle in this case is -6.3°, a fairly steep descent. The low frequency loading caused by the disk vortices is slightly reduced from the previous panel, but the loading from individual blade tip vortices is more apparent in the first and fourth quadrants. Moreover, this BVI loading is seen on both sides of the rotor disk nearly to the blade root.

Figure 7. The flight path angle is -11.7°, which is a steep descent. Both the disk vortex loading and the BVI loading from individual tip vortices is reduced from the prior panel. Moreover, the vortex loading is occurring closer to the rear of the disk, that is the vortices appear sooner in the first quadrant and later in the fourth quadrant.

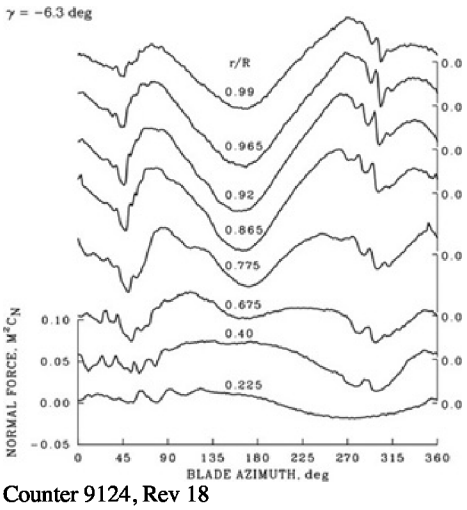

Counter 9124, Rev 18

The normal force (1–120 harmonics) at eight radial stations is shown as an offset plot (Figure 1). The blade loads near the rotor tip are at the top and the loads at the blade root are at the bottom. The flight path angle, γ, is 19.8°, a climb rate that is much steeper than a typical climb out for a helicopter. The advance ratio is about 0.15, which is a typical speed for this helicopter, either for an approach to landing or while climbing out.

Figure 2. The character of the normal force is generally smooth, since the rotor wake is well below the blades at this climb rate and there is no significant interaction with the wake. See the panels in the next tab for the high-frequency content.

Figure 3. The climb angle in this case is $\gamma = 4.0°$, which is close to normal for helicopter operations. At this advance ratio ($\mu = 0.15$), there is significant blade loading from the two disk vortices. In addition, high frequency, low amplitude oscillations are seen at some of these radial stations, which are the result of close interactions of the blade with individual tip vortices from prior blades.

Figure 4. The flight path angle is -0.4°, which is essentially level flight. Loading from the disk vortices is observed outboard on the blade. In addition, loading from individual vortices is particularly noticeable at $r/R = 0.865$ on the advancing side.

Figure 5. The flight path angle is -4.8°, which is a moderate descent, close to the glide path angle used by fixed-wing aircraft in an approach to an airport. The low frequency disk vortex loading on the advancing and retreating sides is similar to the previous panels, but now high frequency loading caused by interactions with individual tip vortices is more noticeable. These interactions appear to be strongest in the first and fourth quadrants.

Figure 6. The flight path angle in this case is -6.3°, a fairly steep descent. The low frequency loading caused by the disk vortices is slightly reduced from the previous panel, but the loading from individual blade tip vortices is more apparent in the first and fourth quadrants. Moreover, this BVI loading is seen on both sides of the rotor disk nearly to the blade root.

Figure 7. The flight path angle is -11.7°, which is a steep descent. Both the disk vortex loading and the BVI loading from individual tip vortices is reduced from the prior panel. Moreover, the vortex loading is occurring closer to the rear of the disk, that is the vortices appear sooner in the first quadrant and later in the fourth quadrant.

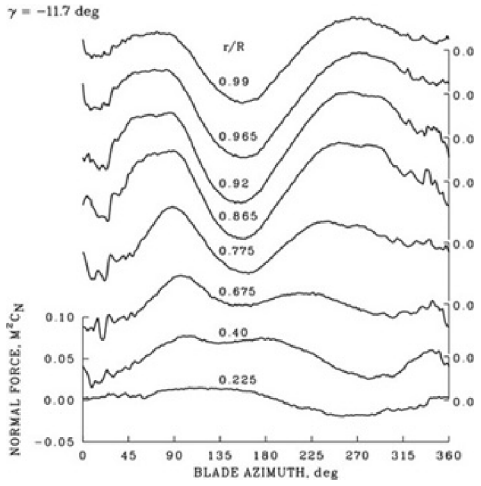

The high-frequency normal forces (17–120 harmonics) at eight radial stations are shown as an offset plot. The plotting of these higher harmonics is like a high-pass filter and allow the visualization of the higher frequencies in the blade loading that dominate the acoustic energy that is radiated by the rotor. At this flight path angle, $\gamma = 19.8°$, the rotor wake is well below the blades and there are no indications of blade vortex interactions (BVI).

The flight path angle, γ, is 4.0° in this case, which is a typical climb angle for this helicopter under normal operations. Limited BVIs are seen on the outer blade, both on the advancing and retreating sides of the rotor disk. The acoustic energy that is radiated depends upon the derivative of the time history, thus both the loading amplitude and frequency are important. The loading amplitude generally depends upon how close a previous vortex is to the blade, the miss distance.

The flight path angle is -0.4°, which is essentially level flight. BVI loading is seen in the first and fourth quadrants, largely outboard on the blade, and this loading is caused by individual tip vortices from previous blades. As noted previously, radiated acoustic energy depends upon the derivative of the loading. But the far field noise also depends on how the energy from the various BVIs add or subtract.

The flight path angle is -4.8°, which is a moderate descent, close to the glide path angle used by fixed-wing aircraft in an approach to an airport. The BVI loading occurs in the first and fourth quadrants as before, but is now stronger (increased amplitude of loading).

The flight path angle is -6.3°, a significant descent rate. At this descent angle, there are multiple interactions at many of the radial stations, indicating that the blade is passing quite close to tip vortices from prior blades. The BVI loading in the fourth quadrant is now quite severe and extends from the blade tip to the $r/R = 0.675$. For this case, the amplitudes in the first quadrant are reduced.

The flight path angle is -11.7°, which is a steep descent. The BVI loading is now reduced on both the advancing and retreating sides. Moreover, this loading is occurring closer to the trailing edge of the disk.

Acoustic energy is radiated over a range of descent angles (and also airspeeds). Picking the best airspeed and descent angle to reduce the noise footprint on the ground is a formidable problem.

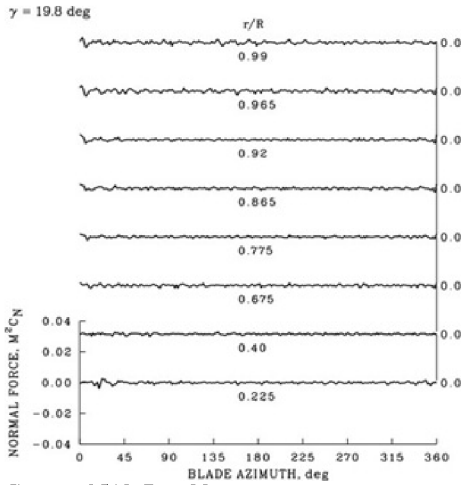

Counter 9512, Rev 03

The high-frequency normal forces (17–120 harmonics) at eight radial stations are shown as an offset plot. The plotting of these higher harmonics is like a high-pass filter and allow the visualization of the higher frequencies in the blade loading that dominate the acoustic energy that is radiated by the rotor. At this flight path angle, $\gamma = 19.8°$, the rotor wake is well below the blades and there are no indications of blade vortex interactions (BVI).

The flight path angle, γ, is 4.0° in this case, which is a typical climb angle for this helicopter under normal operations. Limited BVIs are seen on the outer blade, both on the advancing and retreating sides of the rotor disk. The acoustic energy that is radiated depends upon the derivative of the time history, thus both the loading amplitude and frequency are important. The loading amplitude generally depends upon how close a previous vortex is to the blade, the miss distance.

The flight path angle is -0.4°, which is essentially level flight. BVI loading is seen in the first and fourth quadrants, largely outboard on the blade, and this loading is caused by individual tip vortices from previous blades. As noted previously, radiated acoustic energy depends upon the derivative of the loading. But the far field noise also depends on how the energy from the various BVIs add or subtract.

The flight path angle is -4.8°, which is a moderate descent, close to the glide path angle used by fixed-wing aircraft in an approach to an airport. The BVI loading occurs in the first and fourth quadrants as before, but is now stronger (increased amplitude of loading).

The flight path angle is -6.3°, a significant descent rate. At this descent angle, there are multiple interactions at many of the radial stations, indicating that the blade is passing quite close to tip vortices from prior blades. The BVI loading in the fourth quadrant is now quite severe and extends from the blade tip to the $r/R = 0.675$. For this case, the amplitudes in the first quadrant are reduced.

The flight path angle is -11.7°, which is a steep descent. The BVI loading is now reduced on both the advancing and retreating sides. Moreover, this loading is occurring closer to the trailing edge of the disk.

Acoustic energy is radiated over a range of descent angles (and also airspeeds). Picking the best airspeed and descent angle to reduce the noise footprint on the ground is a formidable problem.

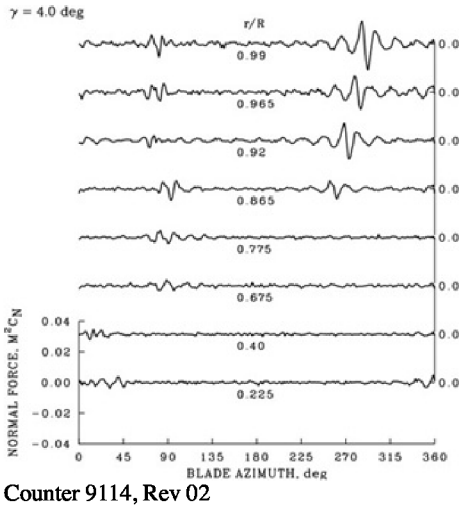

Counter 9114, Rev 02

The high-frequency normal forces (17–120 harmonics) at eight radial stations are shown as an offset plot. The plotting of these higher harmonics is like a high-pass filter and allow the visualization of the higher frequencies in the blade loading that dominate the acoustic energy that is radiated by the rotor. At this flight path angle, $\gamma = 19.8°$, the rotor wake is well below the blades and there are no indications of blade vortex interactions (BVI).

The flight path angle, γ, is 4.0° in this case, which is a typical climb angle for this helicopter under normal operations. Limited BVIs are seen on the outer blade, both on the advancing and retreating sides of the rotor disk. The acoustic energy that is radiated depends upon the derivative of the time history, thus both the loading amplitude and frequency are important. The loading amplitude generally depends upon how close a previous vortex is to the blade, the miss distance.

The flight path angle is -0.4°, which is essentially level flight. BVI loading is seen in the first and fourth quadrants, largely outboard on the blade, and this loading is caused by individual tip vortices from previous blades. As noted previously, radiated acoustic energy depends upon the derivative of the loading. But the far field noise also depends on how the energy from the various BVIs add or subtract.

The flight path angle is -4.8°, which is a moderate descent, close to the glide path angle used by fixed-wing aircraft in an approach to an airport. The BVI loading occurs in the first and fourth quadrants as before, but is now stronger (increased amplitude of loading).

The flight path angle is -6.3°, a significant descent rate. At this descent angle, there are multiple interactions at many of the radial stations, indicating that the blade is passing quite close to tip vortices from prior blades. The BVI loading in the fourth quadrant is now quite severe and extends from the blade tip to the $r/R = 0.675$. For this case, the amplitudes in the first quadrant are reduced.

The flight path angle is -11.7°, which is a steep descent. The BVI loading is now reduced on both the advancing and retreating sides. Moreover, this loading is occurring closer to the trailing edge of the disk.

Acoustic energy is radiated over a range of descent angles (and also airspeeds). Picking the best airspeed and descent angle to reduce the noise footprint on the ground is a formidable problem.

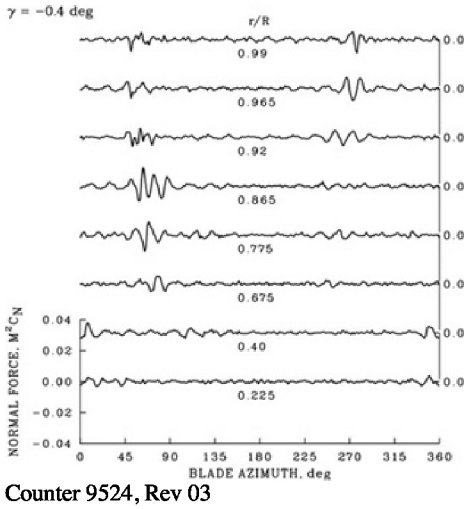

Counter 9524, Rev 03

The high-frequency normal forces (17–120 harmonics) at eight radial stations are shown as an offset plot. The plotting of these higher harmonics is like a high-pass filter and allow the visualization of the higher frequencies in the blade loading that dominate the acoustic energy that is radiated by the rotor. At this flight path angle, $\gamma = 19.8°$, the rotor wake is well below the blades and there are no indications of blade vortex interactions (BVI).

The flight path angle, γ, is 4.0° in this case, which is a typical climb angle for this helicopter under normal operations. Limited BVIs are seen on the outer blade, both on the advancing and retreating sides of the rotor disk. The acoustic energy that is radiated depends upon the derivative of the time history, thus both the loading amplitude and frequency are important. The loading amplitude generally depends upon how close a previous vortex is to the blade, the miss distance.

The flight path angle is -0.4°, which is essentially level flight. BVI loading is seen in the first and fourth quadrants, largely outboard on the blade, and this loading is caused by individual tip vortices from previous blades. As noted previously, radiated acoustic energy depends upon the derivative of the loading. But the far field noise also depends on how the energy from the various BVIs add or subtract.

The flight path angle is -4.8°, which is a moderate descent, close to the glide path angle used by fixed-wing aircraft in an approach to an airport. The BVI loading occurs in the first and fourth quadrants as before, but is now stronger (increased amplitude of loading).

The flight path angle is -6.3°, a significant descent rate. At this descent angle, there are multiple interactions at many of the radial stations, indicating that the blade is passing quite close to tip vortices from prior blades. The BVI loading in the fourth quadrant is now quite severe and extends from the blade tip to the $r/R = 0.675$. For this case, the amplitudes in the first quadrant are reduced.

The flight path angle is -11.7°, which is a steep descent. The BVI loading is now reduced on both the advancing and retreating sides. Moreover, this loading is occurring closer to the trailing edge of the disk.

Acoustic energy is radiated over a range of descent angles (and also airspeeds). Picking the best airspeed and descent angle to reduce the noise footprint on the ground is a formidable problem.

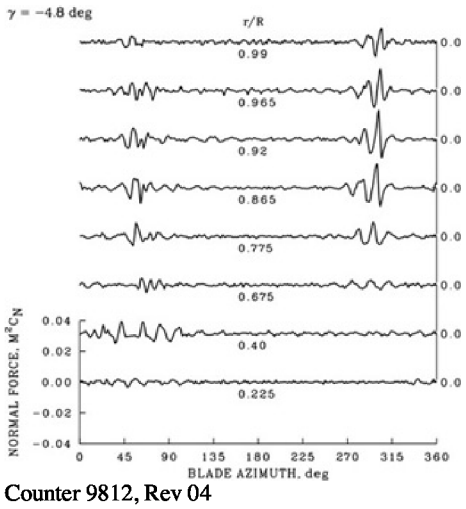

Counter 9812, Rev 04

The high-frequency normal forces (17–120 harmonics) at eight radial stations are shown as an offset plot. The plotting of these higher harmonics is like a high-pass filter and allow the visualization of the higher frequencies in the blade loading that dominate the acoustic energy that is radiated by the rotor. At this flight path angle, $\gamma = 19.8°$, the rotor wake is well below the blades and there are no indications of blade vortex interactions (BVI).

The flight path angle, γ, is 4.0° in this case, which is a typical climb angle for this helicopter under normal operations. Limited BVIs are seen on the outer blade, both on the advancing and retreating sides of the rotor disk. The acoustic energy that is radiated depends upon the derivative of the time history, thus both the loading amplitude and frequency are important. The loading amplitude generally depends upon how close a previous vortex is to the blade, the miss distance.

The flight path angle is -0.4°, which is essentially level flight. BVI loading is seen in the first and fourth quadrants, largely outboard on the blade, and this loading is caused by individual tip vortices from previous blades. As noted previously, radiated acoustic energy depends upon the derivative of the loading. But the far field noise also depends on how the energy from the various BVIs add or subtract.

The flight path angle is -4.8°, which is a moderate descent, close to the glide path angle used by fixed-wing aircraft in an approach to an airport. The BVI loading occurs in the first and fourth quadrants as before, but is now stronger (increased amplitude of loading).

The flight path angle is -6.3°, a significant descent rate. At this descent angle, there are multiple interactions at many of the radial stations, indicating that the blade is passing quite close to tip vortices from prior blades. The BVI loading in the fourth quadrant is now quite severe and extends from the blade tip to the $r/R = 0.675$. For this case, the amplitudes in the first quadrant are reduced.

The flight path angle is -11.7°, which is a steep descent. The BVI loading is now reduced on both the advancing and retreating sides. Moreover, this loading is occurring closer to the trailing edge of the disk.

Acoustic energy is radiated over a range of descent angles (and also airspeeds). Picking the best airspeed and descent angle to reduce the noise footprint on the ground is a formidable problem.

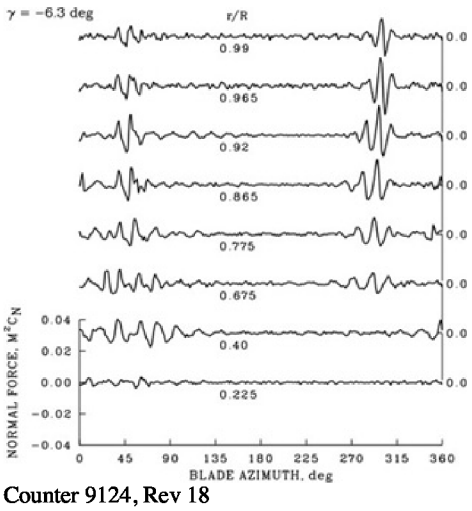

Counter 9124, Rev 18

The high-frequency normal forces (17–120 harmonics) at eight radial stations are shown as an offset plot. The plotting of these higher harmonics is like a high-pass filter and allow the visualization of the higher frequencies in the blade loading that dominate the acoustic energy that is radiated by the rotor. At this flight path angle, $\gamma = 19.8°$, the rotor wake is well below the blades and there are no indications of blade vortex interactions (BVI).

The flight path angle, γ, is 4.0° in this case, which is a typical climb angle for this helicopter under normal operations. Limited BVIs are seen on the outer blade, both on the advancing and retreating sides of the rotor disk. The acoustic energy that is radiated depends upon the derivative of the time history, thus both the loading amplitude and frequency are important. The loading amplitude generally depends upon how close a previous vortex is to the blade, the miss distance.

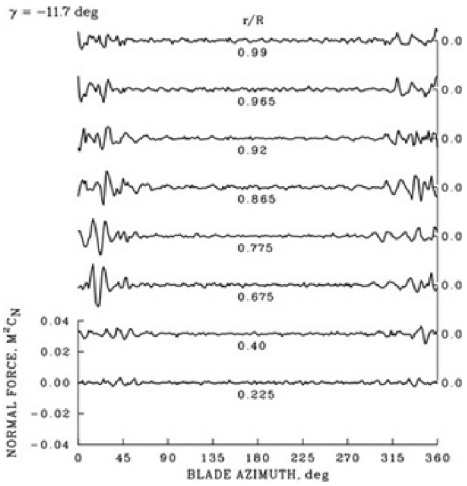

The flight path angle is -0.4°, which is essentially level flight. BVI loading is seen in the first and fourth quadrants, largely outboard on the blade, and this loading is caused by individual tip vortices from previous blades. As noted previously, radiated acoustic energy depends upon the derivative of the loading. But the far field noise also depends on how the energy from the various BVIs add or subtract.

The flight path angle is -4.8°, which is a moderate descent, close to the glide path angle used by fixed-wing aircraft in an approach to an airport. The BVI loading occurs in the first and fourth quadrants as before, but is now stronger (increased amplitude of loading).

The flight path angle is -6.3°, a significant descent rate. At this descent angle, there are multiple interactions at many of the radial stations, indicating that the blade is passing quite close to tip vortices from prior blades. The BVI loading in the fourth quadrant is now quite severe and extends from the blade tip to the $r/R = 0.675$. For this case, the amplitudes in the first quadrant are reduced.

The flight path angle is -11.7°, which is a steep descent. The BVI loading is now reduced on both the advancing and retreating sides. Moreover, this loading is occurring closer to the trailing edge of the disk.

Acoustic energy is radiated over a range of descent angles (and also airspeeds). Picking the best airspeed and descent angle to reduce the noise footprint on the ground is a formidable problem.

The high approach noise condition at γ = -6.3° in the previous tab was one of eight repeat points. The difficulty in matching such conditions is apparent in this figure which shows the computed tip-path-plane angle, averaged over each revolution, for the eight points. It is difficult to obtain a repeated condition and there is variation in the tip-path-plane angle over the test point. This results in loading changes for the duration of the test point, as illustrated in the next tab for Counter 9812. This amount of unsteadiness is typical of any helicopter in descending flight, but it makes the comparison of flight and ground-acoustic measurements more difficult.

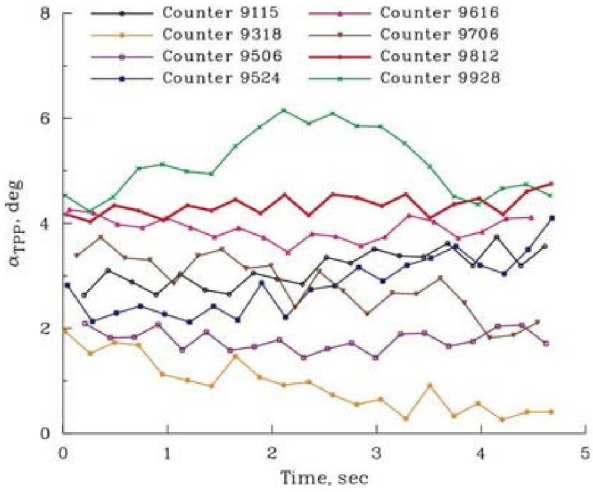

The normal force (17-120 harmonics) at eight radial stations is shown as an offset plot for a flight path angle of -6.3°. For this descent, the pilot attempted to fly a steady profile, yet there is variation in BVI amplitudes over 20 revolutions as can be seen by clicking the button. The variation in this sequence indicates small, relative shifts in the rotor blade and the rotor vortex wake (affecting miss distance). These changes will influence the noise radiated to the far field and hence the noise footprint. Although this variation creates difficulties for the analyst attempting to reproduce this flight condition, such variation on approach is a normal and expected condition.

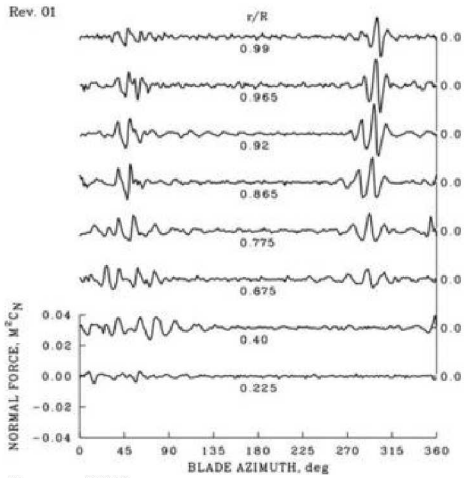

Counter 9812

The normal force (17-120 harmonics) at eight radial stations is shown as an offset plot for a flight path angle of -6.3°. For this descent, the pilot attempted to fly a steady profile, yet there is variation in BVI amplitudes over 20 revolutions as can be seen by clicking the button. The variation in this sequence indicates small, relative shifts in the rotor blade and the rotor vortex wake (affecting miss distance). These changes will influence the noise radiated to the far field and hence the noise footprint. Although this variation creates difficulties for the analyst attempting to reproduce this flight condition, such variation on approach is a normal and expected condition.

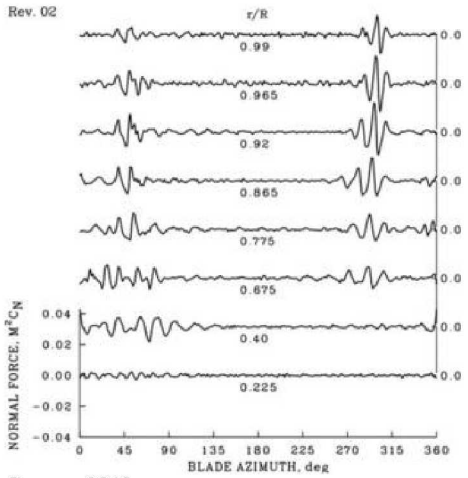

Counter 9812

The normal force (17-120 harmonics) at eight radial stations is shown as an offset plot for a flight path angle of -6.3°. For this descent, the pilot attempted to fly a steady profile, yet there is variation in BVI amplitudes over 20 revolutions as can be seen by clicking the button. The variation in this sequence indicates small, relative shifts in the rotor blade and the rotor vortex wake (affecting miss distance). These changes will influence the noise radiated to the far field and hence the noise footprint. Although this variation creates difficulties for the analyst attempting to reproduce this flight condition, such variation on approach is a normal and expected condition.

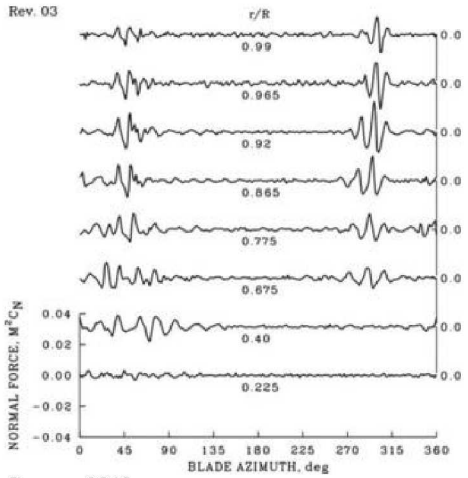

Counter 9812

The normal force (17-120 harmonics) at eight radial stations is shown as an offset plot for a flight path angle of -6.3°. For this descent, the pilot attempted to fly a steady profile, yet there is variation in BVI amplitudes over 20 revolutions as can be seen by clicking the button. The variation in this sequence indicates small, relative shifts in the rotor blade and the rotor vortex wake (affecting miss distance). These changes will influence the noise radiated to the far field and hence the noise footprint. Although this variation creates difficulties for the analyst attempting to reproduce this flight condition, such variation on approach is a normal and expected condition.

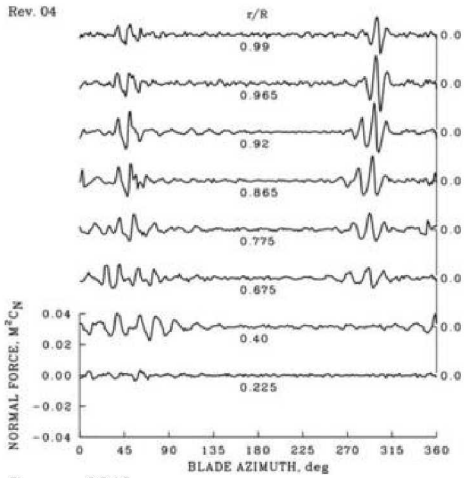

Counter 9812

The normal force (17-120 harmonics) at eight radial stations is shown as an offset plot for a flight path angle of -6.3°. For this descent, the pilot attempted to fly a steady profile, yet there is variation in BVI amplitudes over 20 revolutions as can be seen by clicking the button. The variation in this sequence indicates small, relative shifts in the rotor blade and the rotor vortex wake (affecting miss distance). These changes will influence the noise radiated to the far field and hence the noise footprint. Although this variation creates difficulties for the analyst attempting to reproduce this flight condition, such variation on approach is a normal and expected condition.

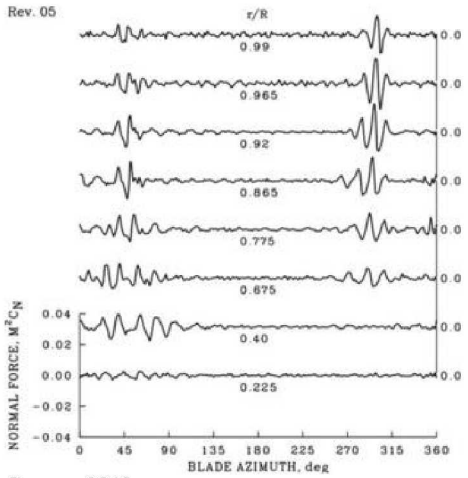

Counter 9812

The normal force (17-120 harmonics) at eight radial stations is shown as an offset plot for a flight path angle of -6.3°. For this descent, the pilot attempted to fly a steady profile, yet there is variation in BVI amplitudes over 20 revolutions as can be seen by clicking the button. The variation in this sequence indicates small, relative shifts in the rotor blade and the rotor vortex wake (affecting miss distance). These changes will influence the noise radiated to the far field and hence the noise footprint. Although this variation creates difficulties for the analyst attempting to reproduce this flight condition, such variation on approach is a normal and expected condition.

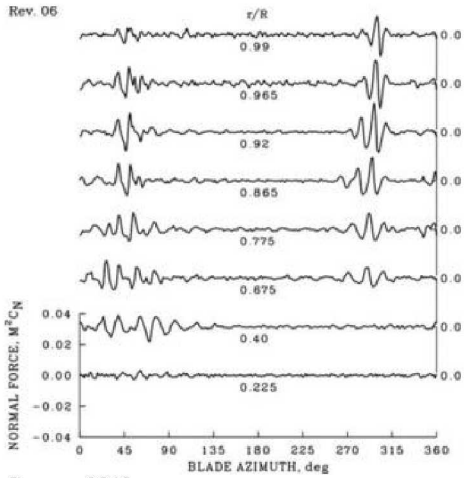

Counter 9812

The normal force (17-120 harmonics) at eight radial stations is shown as an offset plot for a flight path angle of -6.3°. For this descent, the pilot attempted to fly a steady profile, yet there is variation in BVI amplitudes over 20 revolutions as can be seen by clicking the button. The variation in this sequence indicates small, relative shifts in the rotor blade and the rotor vortex wake (affecting miss distance). These changes will influence the noise radiated to the far field and hence the noise footprint. Although this variation creates difficulties for the analyst attempting to reproduce this flight condition, such variation on approach is a normal and expected condition.

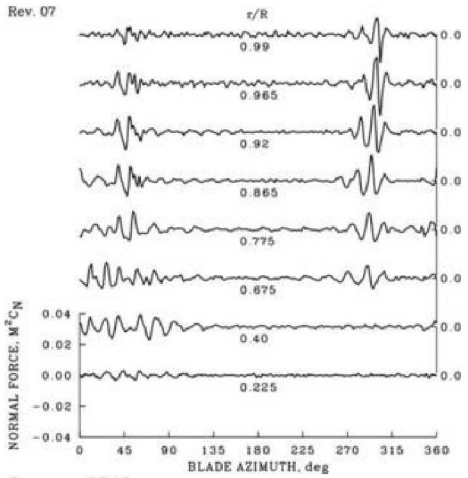

Counter 9812

The normal force (17-120 harmonics) at eight radial stations is shown as an offset plot for a flight path angle of -6.3°. For this descent, the pilot attempted to fly a steady profile, yet there is variation in BVI amplitudes over 20 revolutions as can be seen by clicking the button. The variation in this sequence indicates small, relative shifts in the rotor blade and the rotor vortex wake (affecting miss distance). These changes will influence the noise radiated to the far field and hence the noise footprint. Although this variation creates difficulties for the analyst attempting to reproduce this flight condition, such variation on approach is a normal and expected condition.

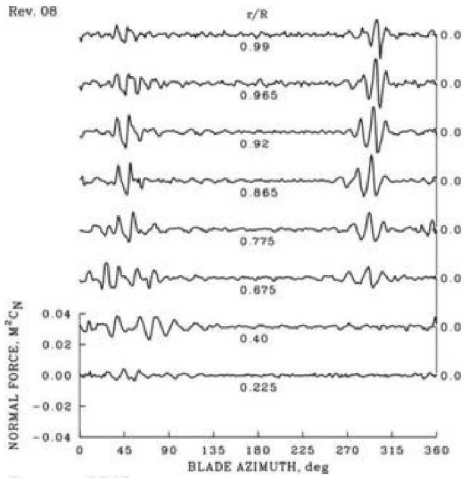

Counter 9812

The normal force (17-120 harmonics) at eight radial stations is shown as an offset plot for a flight path angle of -6.3°. For this descent, the pilot attempted to fly a steady profile, yet there is variation in BVI amplitudes over 20 revolutions as can be seen by clicking the button. The variation in this sequence indicates small, relative shifts in the rotor blade and the rotor vortex wake (affecting miss distance). These changes will influence the noise radiated to the far field and hence the noise footprint. Although this variation creates difficulties for the analyst attempting to reproduce this flight condition, such variation on approach is a normal and expected condition.

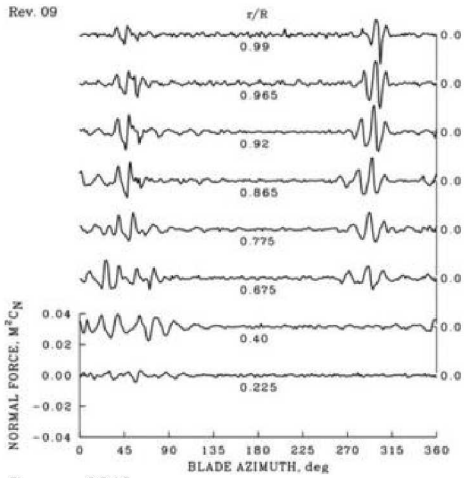

Counter 9812

The normal force (17-120 harmonics) at eight radial stations is shown as an offset plot for a flight path angle of -6.3°. For this descent, the pilot attempted to fly a steady profile, yet there is variation in BVI amplitudes over 20 revolutions as can be seen by clicking the button. The variation in this sequence indicates small, relative shifts in the rotor blade and the rotor vortex wake (affecting miss distance). These changes will influence the noise radiated to the far field and hence the noise footprint. Although this variation creates difficulties for the analyst attempting to reproduce this flight condition, such variation on approach is a normal and expected condition.

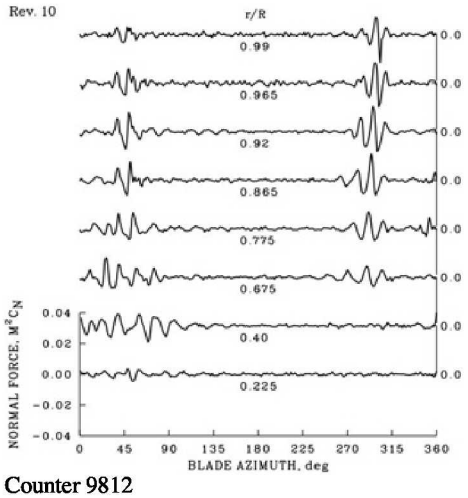

Counter 9812

The normal force (17-120 harmonics) at eight radial stations is shown as an offset plot for a flight path angle of -6.3°. For this descent, the pilot attempted to fly a steady profile, yet there is variation in BVI amplitudes over 20 revolutions as can be seen by clicking the button. The variation in this sequence indicates small, relative shifts in the rotor blade and the rotor vortex wake (affecting miss distance). These changes will influence the noise radiated to the far field and hence the noise footprint. Although this variation creates difficulties for the analyst attempting to reproduce this flight condition, such variation on approach is a normal and expected condition.

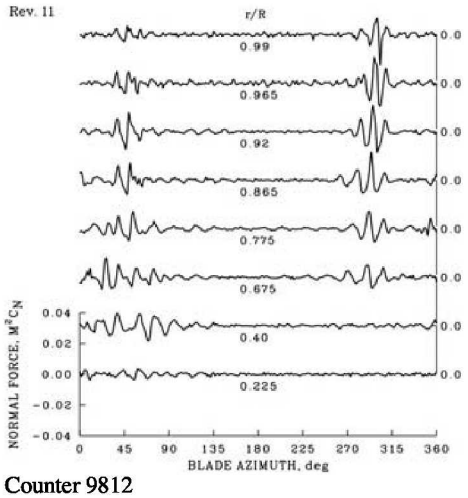

Counter 9812

The normal force (17-120 harmonics) at eight radial stations is shown as an offset plot for a flight path angle of -6.3°. For this descent, the pilot attempted to fly a steady profile, yet there is variation in BVI amplitudes over 20 revolutions as can be seen by clicking the button. The variation in this sequence indicates small, relative shifts in the rotor blade and the rotor vortex wake (affecting miss distance). These changes will influence the noise radiated to the far field and hence the noise footprint. Although this variation creates difficulties for the analyst attempting to reproduce this flight condition, such variation on approach is a normal and expected condition.

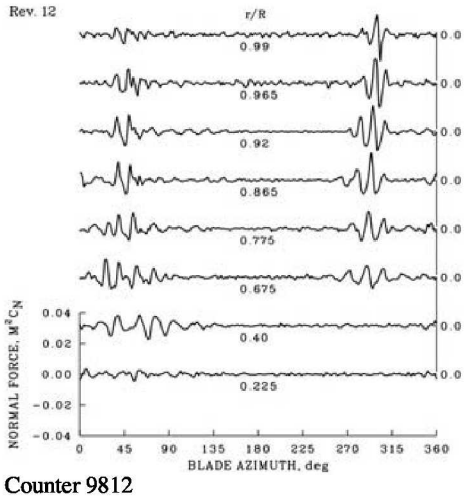

Counter 9812

The normal force (17-120 harmonics) at eight radial stations is shown as an offset plot for a flight path angle of -6.3°. For this descent, the pilot attempted to fly a steady profile, yet there is variation in BVI amplitudes over 20 revolutions as can be seen by clicking the button. The variation in this sequence indicates small, relative shifts in the rotor blade and the rotor vortex wake (affecting miss distance). These changes will influence the noise radiated to the far field and hence the noise footprint. Although this variation creates difficulties for the analyst attempting to reproduce this flight condition, such variation on approach is a normal and expected condition.

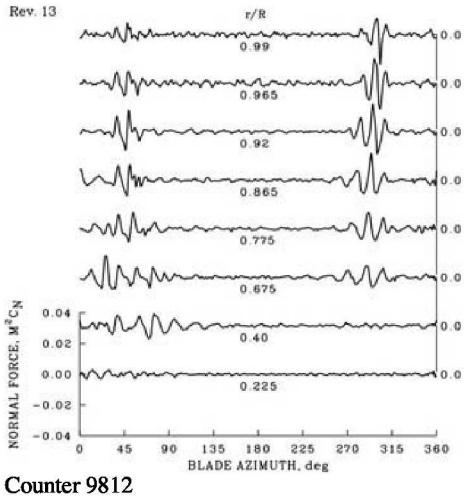

Counter 9812

The normal force (17-120 harmonics) at eight radial stations is shown as an offset plot for a flight path angle of -6.3°. For this descent, the pilot attempted to fly a steady profile, yet there is variation in BVI amplitudes over 20 revolutions as can be seen by clicking the button. The variation in this sequence indicates small, relative shifts in the rotor blade and the rotor vortex wake (affecting miss distance). These changes will influence the noise radiated to the far field and hence the noise footprint. Although this variation creates difficulties for the analyst attempting to reproduce this flight condition, such variation on approach is a normal and expected condition.

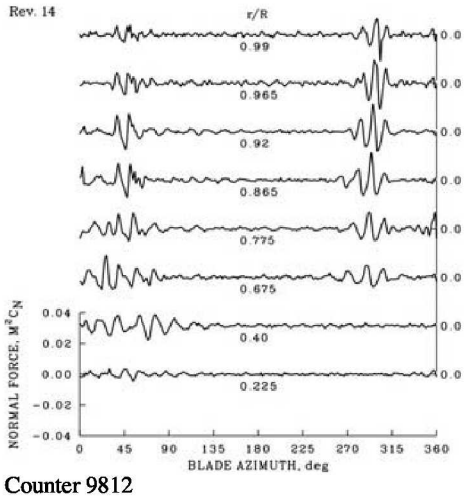

Counter 9812

The normal force (17-120 harmonics) at eight radial stations is shown as an offset plot for a flight path angle of -6.3°. For this descent, the pilot attempted to fly a steady profile, yet there is variation in BVI amplitudes over 20 revolutions as can be seen by clicking the button. The variation in this sequence indicates small, relative shifts in the rotor blade and the rotor vortex wake (affecting miss distance). These changes will influence the noise radiated to the far field and hence the noise footprint. Although this variation creates difficulties for the analyst attempting to reproduce this flight condition, such variation on approach is a normal and expected condition.

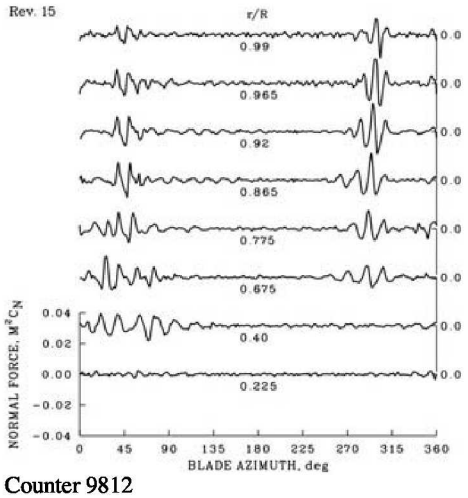

Counter 9812

The normal force (17-120 harmonics) at eight radial stations is shown as an offset plot for a flight path angle of -6.3°. For this descent, the pilot attempted to fly a steady profile, yet there is variation in BVI amplitudes over 20 revolutions as can be seen by clicking the button. The variation in this sequence indicates small, relative shifts in the rotor blade and the rotor vortex wake (affecting miss distance). These changes will influence the noise radiated to the far field and hence the noise footprint. Although this variation creates difficulties for the analyst attempting to reproduce this flight condition, such variation on approach is a normal and expected condition.

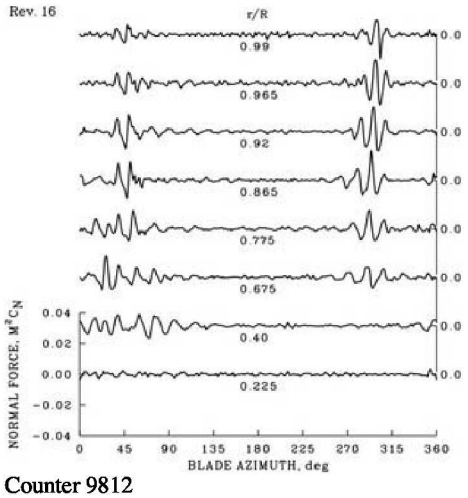

Counter 9812

The normal force (17-120 harmonics) at eight radial stations is shown as an offset plot for a flight path angle of -6.3°. For this descent, the pilot attempted to fly a steady profile, yet there is variation in BVI amplitudes over 20 revolutions as can be seen by clicking the button. The variation in this sequence indicates small, relative shifts in the rotor blade and the rotor vortex wake (affecting miss distance). These changes will influence the noise radiated to the far field and hence the noise footprint. Although this variation creates difficulties for the analyst attempting to reproduce this flight condition, such variation on approach is a normal and expected condition.

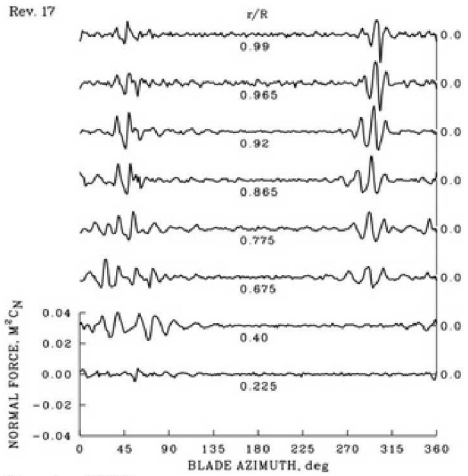

Counter 9812

The normal force (17-120 harmonics) at eight radial stations is shown as an offset plot for a flight path angle of -6.3°. For this descent, the pilot attempted to fly a steady profile, yet there is variation in BVI amplitudes over 20 revolutions as can be seen by clicking the button. The variation in this sequence indicates small, relative shifts in the rotor blade and the rotor vortex wake (affecting miss distance). These changes will influence the noise radiated to the far field and hence the noise footprint. Although this variation creates difficulties for the analyst attempting to reproduce this flight condition, such variation on approach is a normal and expected condition.

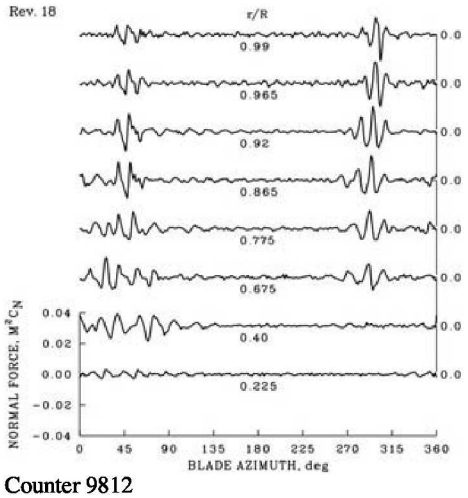

Counter 9812

The normal force (17-120 harmonics) at eight radial stations is shown as an offset plot for a flight path angle of -6.3°. For this descent, the pilot attempted to fly a steady profile, yet there is variation in BVI amplitudes over 20 revolutions as can be seen by clicking the button. The variation in this sequence indicates small, relative shifts in the rotor blade and the rotor vortex wake (affecting miss distance). These changes will influence the noise radiated to the far field and hence the noise footprint. Although this variation creates difficulties for the analyst attempting to reproduce this flight condition, such variation on approach is a normal and expected condition.

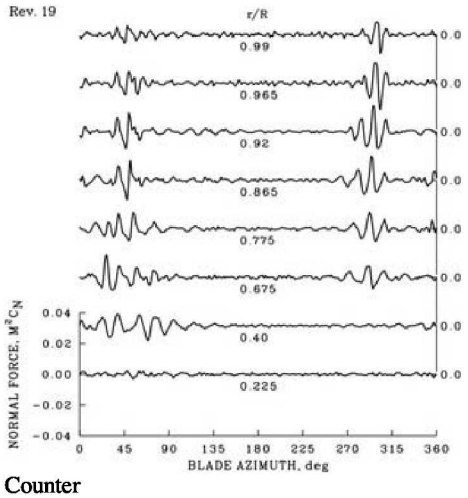

Counter

The normal force (17-120 harmonics) at eight radial stations is shown as an offset plot for a flight path angle of -6.3°. For this descent, the pilot attempted to fly a steady profile, yet there is variation in BVI amplitudes over 20 revolutions as can be seen by clicking the button. The variation in this sequence indicates small, relative shifts in the rotor blade and the rotor vortex wake (affecting miss distance). These changes will influence the noise radiated to the far field and hence the noise footprint. Although this variation creates difficulties for the analyst attempting to reproduce this flight condition, such variation on approach is a normal and expected condition.

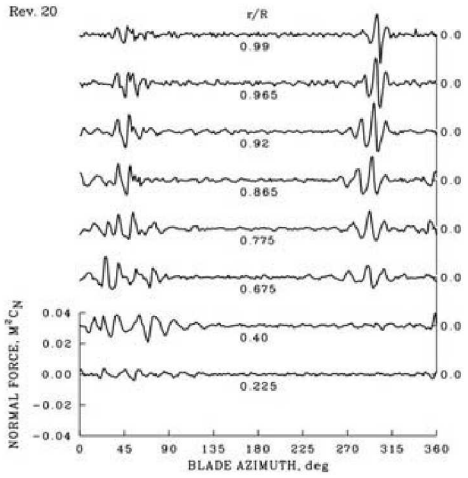

Inflight acoustic measurements were obtained by flying behind a YO-3A airplane used as an acoustic platform. The UH-60A trailed behind and to the right of the YO--3A, using lines on the latter to orient the helicopter. A hand-held laser rangefinder was used to determine distance (McCluer and Dearing 1996). Three microphones were installed on the YO-3A, one on each wing tip and one on the top of the vertical stabilizer. The YO-3A pilot then set the test condition while the UH-60A pilot maintained station. Acoustic data were recorded on the YO-3A, and these are in a database separate from the UH-60A Airloads Program database.

The UH-60A inflight-acoustic test matrix, in terms of flight path angle and advance ratio, is compared with the ground-acoustic test matrix shown previously for the Airloads Program (Figure 1 excludes most of the climb data from the ground-acoustic tests). The inflight testing focused exclusively on level and descending flight over a limited range of advance ratios. In part this was because of the flight envelope limits of the YO-3A, but also to focus on the approach condition for the UH-60A, which is centered around $\mu = 0.17$. Two weight coefficients were flown: 0.071 to match the DNW tests discussed below and 0.086 to examine the effects of rotor thrust on noise.

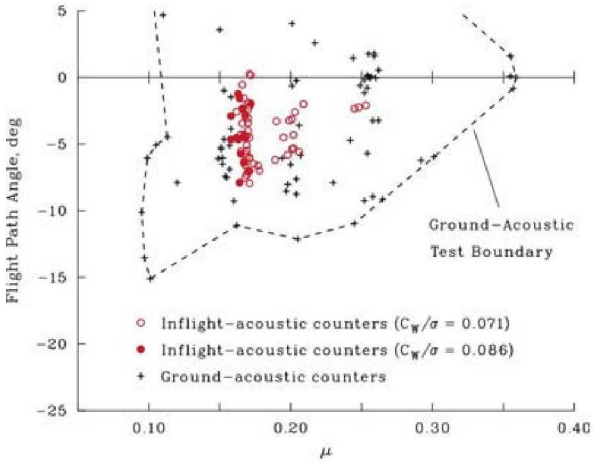

Figure 2. Click the arrow to see the UH-60A inflight-acoustic test matrix compared with test points from an 0.17-scale model test of the UH-60A rotor in the DNW in 1989. The full-scale UH-60A flight data overlap the model-scale data, and obtain high resolution in terms of flight path angle near the UH-60A's approach speed of $\mu = 0.17$.

The UH-60A inflight-acoustic test matrix, in terms of flight path angle and advance ratio, is compared with the ground-acoustic test matrix shown previously for the Airloads Program (Figure 1 excludes most of the climb data from the ground-acoustic tests). The inflight testing focused exclusively on level and descending flight over a limited range of advance ratios. In part this was because of the flight envelope limits of the YO-3A, but also to focus on the approach condition for the UH-60A, which is centered around $\mu = 0.17$. Two weight coefficients were flown: 0.071 to match the DNW tests discussed below and 0.086 to examine the effects of rotor thrust on noise.

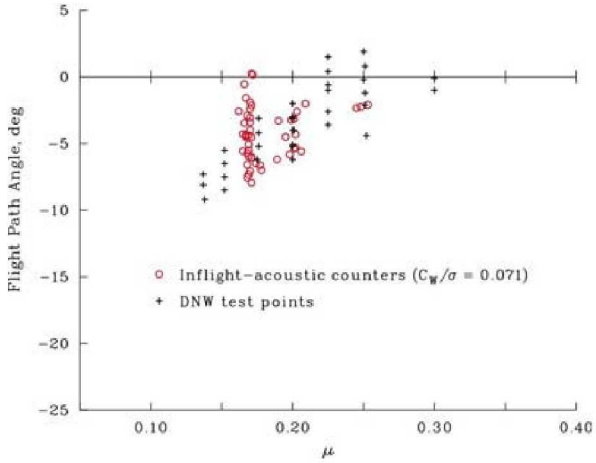

Figure 2. Click the arrow to see the UH-60A inflight-acoustic test matrix compared with test points from an 0.17-scale model test of the UH-60A rotor in the DNW in 1989. The full-scale UH-60A flight data overlap the model-scale data, and obtain high resolution in terms of flight path angle near the UH-60A's approach speed of $\mu = 0.17$.

A comparison of the radial distribution of normal force (17–120 harmonics) is shown as an offset plot for two descent cases and shows the close relationship between these two types of acoustic testing. The ground-acoustic counter ($\mu = 0.15, \gamma = -6.3°, \alpha_{TPP} = 4.2°$) and the inflight-acoustic counter ($\mu = 0.17, \gamma = -6.2°, \alpha_{TPP} = 4.2°$) are well matched except in advance ratio. There are differences in the location of the BVI interactions, perhaps caused by the advance ratio difference, and in the amplitudes of the interactions. Neither of these descent conditions are steady, as expected in the wind tunnel, but they do represent realistic approach conditions for a helicopter.

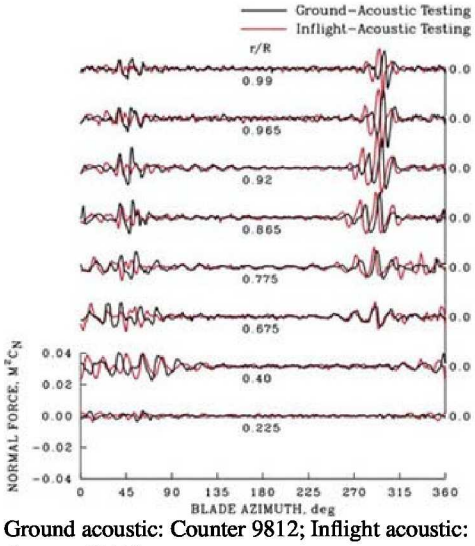

Ground acoustic: Counter 9812; Inflight acoustic: Counter 10112

Brought to you by the UH-60A Airloads Program Team!